Developing Photo-responsive Metal-Organic Frameworks towards Controlled Drug Delivery

Charity Cherie Epley

Dissertation submitted to the faculty of the Virginia Polytechnic Institute and State University in partial fulfillment of the requirements for the degree of

Doctor of Philosophy
In
Chemistry

Amanda J. Morris, Chair

Tijana Z. Grove

Alan R. Esker

David G. I. Kingston

June 14th, 2017
Blacksburg, VA

Keywords: metal-organic frameworks, nanocarriers, photodynamic therapy, theranostics, nanomedicine, drug delivery, post-synthetic modification, contrast agents

Developing Photo-responsive Metal-Organic Frameworks for Controlled Drug Delivery

Charity Cherie Epley

ABSTRACT

Metal-Organic Frameworks (MOFs) are assemblies of metal nodes bridged by multidentate organic linkers, to create hybrid networks with extremely high surface areas. These materials are a new class of highly porous solids that are being developed for a range of applications, from gas sorption to catalysis. Since the first report of exceptionally high drug loading capacities (up to 140 wt %), interest involving their applicability for biological applications has become an expanding area of exploration. In the last decade or so, researchers have developed MOF nanocarriers that are capable of encapsulating and releasing a multitude of drugs and have also created MOF nanoparticles for diagnostic imaging. Advantages of these nanocarriers over purely inorganic nanoparticles include: 1) tunability due to the incorporation of different metals and organic components, 2) their ability to decompose in biological media attributed to the hydrolytic nature of metal-linker bonds, and of course 3) the high surface areas that lead to enhanced drug uptake as mentioned. Additionally, they may be coated with stabilizing polymers that can reduce the "burst effect" that plagues organic polymers and micelles. Although MOFs show great promise in biomedicine, *controlled* drug delivery and release remains an issue under investigation.

In this regard, we have developed MOF nanocarriers (~100 nm) incorporating photo-isomerizable 4,4´-azobenzenedicarboxylate linkers that are not photo-stable and controllably degrade upon irradiation with white light. Experimental evidence suggested that the nanocarriers were selective for hydrophobic drugs and we have shown that the release of the model drug Nile

Red was enhanced upon irradiation, with release rates of 0.04 ± 0.01 %/h in the dark, and 0.36 ± 0.02 %/h when irradiated. We have also used the nanocarrier as a platform for the development of a polymer coated drug system that delivers the cancer drug 5-fluorouracil to MCF-7 human breast cancer cells. When treated with the MOF drug system in the dark, the toxicity to the cells is low; however, we observe increased cell death under irradiation, attributed to the release of 5-fluorouracil from the nanocarrier. Additionally, we have also developed a Mn^{II} based MOF that shows promise for dual mode magnetic resonance imaging (MRI) contrast and optical imaging to aid in diagnosis. Mn^{II} MRI contrast agents are attractive due to the reduced toxicity of Mn^{II} in comparison to the clinically available Gd^{III} that has been shown to cause nephrogenic systemic fibrosis. The materials developed provide a foundation and prototypes for the optimization of MOFs in biomedicine and specifically for controlled stimuli-responsive nanocarriers. Finally, the development of oxygen-independent photo-therapeutics that are capable of being effective for hypoxic tumors is the next step to the broader use of photodynamic therapy (PDT), and these efforts highlight ways to advance the goals of therapies that reduce biologically systemic off target side effects, specifically for cancer research.

Developing Photo-responsive Metal-Organic Frameworks for Controlled Drug Delivery

Charity Cherie Epley

ABSTRACT
(General Audience)

The development of therapeutic drugs or drug systems that enhance a cancer patient's quality of life during treatment is a primary goal for many researchers across a wide range of disciplines. Many investigators turn to nanoparticles (~50-200 nm in size) that tend to accumulate in tumor tissues in order to deliver active drug compounds to specific sites in the body. This targeted delivery approach would reduce the total body effects of current cancer drugs that result in unwanted (sometimes painful and even fatal) side effects. One of the main obstacles however, is ensuring that drugs incorporated into the nanoparticles are anchored such that premature drug release is prohibited. Also, while it is important to ensure strong drug-nanocarrier interactions, the nanocarrier must be able to release the drug when it has reached its biological target. We have developed a nanocarrier that provides a platform for drug systems that could achieve this drug release via the use of a light "trigger".

Metal-Organic Frameworks (MOFs) are a relatively new class of often highly porous materials that act as "sponges" for the absorption of various small molecules. MOFs are so named because they consist of metal clusters that are linked by organic compounds to form networked solids that are easily tuned based on the choice of metal and organic "linker". We have developed a MOF nanocarrier incorporating benign zirconium (IV) metal clusters bridged by an organic component that changes shape when illuminated with a light source. The resulting material is therefore not stable upon irradiation due to the organic linker shape change that disturbs the MOF structure and causes it to degrade. When loaded with drugs, this photo-

enhanced degradation results in the release of the cargo thereby, providing a handle on controlling drug release with the use of a light trigger. We have demonstrated that in the presence of the MOF nanocarrier incorporating 5-fluorouracil (a clinically available cancer drug), very low toxicity to human breast cancer cells is observed in the dark, however, cell death occurs in the presence of a light source. These reports offer a model MOF nanocarrier system that could be used to incorporate various drugs and therefore tune the system to an individual patient's needs.

Furthermore, we also developed a material that is capable of providing magnetic resonance imaging (MRI) contrast by changing the metal to manganese (II). MRI contrast agents are compounds that serve to either darken or brighten an MRI image based on the agent used and therefore they aid in clinical diagnosis by making internal abnormalities easier to spot. Currently gadolinium (III) complexes are the most widely used contrast agents; however, the toxicity of gadolinium (III) has been shown to be responsible for the development of nephrogenic systemic fibrosis in some patients. This manganese material has also shown useful for the attachment of fluorescent dyes that can aid in the benchtop optical diagnosis of biopsies. These reports provide a basis for developing ways to offer controlled drug delivery in cancer patients and to aid in cancer diagnosis using MOF materials, in an effort to reach the goals of comfortable cancer treatment.

Acknowledgements

First thanks go to my talented advisor, Dr. Amanda Morris, for her continued guidance throughout my graduate career. We have grown in this process together, as we navigated our simultaneous first years in the Chemistry Department, and there is so much gratitude I have for her direction and patience with me. I have developed a tremendous amount of respect for Dr. Morris and she has significantly helped me mature, both scientifically and professionally.

Many thanks also go to A. Morris group members, both past and present, that have helped shape the science I do and the scientist I am. Without long talks at lunch, scrutinizing questions during group meetings and, the occasional science-meets-alcohol "conferences" at various establishments around campus, I wouldn't have been able to hone my critical thinking skills to the level I am at today. Specifically, I would like to extend appreciation to Spencer R. Ahrenholtz for being there for me through this entire process. Her friendship and encouragement has served as a foundation to believe in myself and I have truly appreciated her company and advice through the years. I will always share a special kinship with all venerated A. Morris group members that have been a crucial part of my journey.

I thank my committee: Dr. Tijana Grove, Dr. Alan Esker, and Dr. David G. I. Kingston; I owe much appreciation for their contributions in various meetings that helped guide me and my work. Although at first, I was terrified at just the sight of them, I have come to respect and deeply value their vital counsel. Due to the collaborative nature of our work, Professor Grove has been specifically instrumental in helping to lead my research path and has offered me indispensible personal support.

I would like to give thanks to the entire Department of Chemistry for allowing me this opportunity to pursue my goals. Without the many departmental personnel (Joli Huynh, Mehdi

Ashraf-Khorassani, Tom Wertalik, John Burleson, Sharelle Carbaugh, Geno Iannaccone, Laurie Good, and many more), necessary day-to-day operations would not be possible. Just thinking about the wonderful supporting staff our department has, makes it no surprise how the department has received an "Exemplary Department" award for three consecutive years.

Lastly, I extend my love and appreciation to my family. Their support has been central to my lifelong academic pursuit. As a young child, my mother would escort me to the library to check out books even before I began kindergarten, and I believe those moments and memories were essential for catalyzing my passion for knowledge. My entire family has always pushed me to excel in academia and I will be forever grateful to each of you. Special thanks go to my brother and sister, John Epley and Lauren Epley Denton; my parents, Lori Franklin Steuer and Randy Epley; all my grandparents (most of who I lost over the last 10 years during my academic quest); and to an extremely special friend of mine who I consider family, Elizabeth Powell Blevins. I love and thank you all.

Table of Contents

Table of Contents

Attributions

Chapter 1 of this dissertation was adapted from a book chapter titled "Metal-Organic Frameworks in Theranostic Nanomedicine" published in the book *Metal-Organic Frameworks (MOFs): Chemistry, Technologies, and Applications* by Nova Science Publishers © 2016 to which the author, Charity C. Epley (C.C.E.) was a major contributor. Writing assistance and editing was provided by Dr. Amanda J. Morris.

Chapter 2 was written using a published manuscript. C.C.E. and Kristina L. Roth performed experiments and assisted with manuscript writing and editing. Shaoyang Lin provided TGA data. Dr. Spencer R. Ahrenholtz measured N_2 isotherms. Dr. Tijana Z. Grove provided experimental vision and assisted with writing and editing. Dr. Amanda J. Morris, principle investigator (PI), provided experimental management and assisted in writing and editing.

Chapter 3. C.C.E. performed all experiments. Madeline D. Love helped optimize the synthesis of the materials under study. Dr. Amanda J. Morris, PI, provided experimental management, helped with data interpretation, and assisted in writing and editing.

Chapter 4. C.C.E. and Kristina L. Roth synthesized the materials, performed experiments, and assisted in writing and editing. Mehdi Ashraf-Khorassani performed HPLC analysis. Margaret L. McAndrew and Josh J. Novak assisted with synthesis and experiments. Dr. Tijana Z. Grove and Dr. Amanda J. Morris were the PIs, and supervised the project, provided experimental management, and assisted in writing and editing.

Chapter 5. C.C.E synthesized and characterized the MOF and performed experiments. Kristina L. Roth performed experiments and assisted in writing and editing. Dr. Tijana Z. Grove assisted in writing and editing. Dr. Amanda J. Morris, PI, provided experimental management and assisted in writing and editing.

1. Metal-Organic Frameworks in Theranostic Nanomedicine

This chapter has been adapted from an invited book chapter written by Charity C. Epley and Amanda J. Morris titled "Metal-Organic Frameworks in Theranostic Nanomedicine." This chapter was published in the book *Metal-Organic Frameworks (MOFs): Chemistry, Technologies, and Applications* by Nova Science Publishers, New York, NY © 2016.

1.1 Abstract

Paul Ehrlich's concept of "magic bullet" therapy for marking and inducing diseased cell death is becoming more feasible with today's newest technologies.[1] Particularly, the design of a single material capable of the "triple threat": 1) *in vivo* targeting, 2) site specific drug delivery, and 3) diagnostic imaging, is at the forefront of nanomedicine. Materials demonstrating these properties are termed theranostics, that is, therapy and diagnostics provided by a solitary system. Metal-organic frameworks (MOFs), consisting of metal nodes bridged by multidentate organic linkers, are prime candidates for the development of such theranostic devices due to properties including high porosities and synthetic tunability.

Porous MOFs offer high drug loading capacities, first evidenced by Ferey et al.,[2] with an exceptional 1.4 g ibuprofen (IBU) loading per g MOF for MIL-101 (MIL = Materials of Institut Lavoisier), $Cr_3F(H_2O)_2O[(O_2C)\text{-}C_6H_4\text{-}(CO_2)]_3 \bullet 25H_2O$ with pore diameters of 29-34 Å.[3] Additionally, post-synthetic modifications (PSMs) and surface coatings of MOF nanoparticles offer an avenue to affix targeting peptides to the surface, thereby providing a platform to deliver drug cargos directly to their intended site of action. Finally, PSMs can also be used to bind fluorescent dyes for imaging purposes and the incorporation of proper metal centers into the MOF structure can offer the integrated advantage of MRI contrast.[4-6] The ability to synthetically manipulate MOFs in these ways is paramount to their realization in the expanding field of nanomedicine and patient customized treatments. This chapter will focus on the major

breakthroughs of MOFs reported to date for nanomedicine applications followed by short commentary addressing deficient areas in the field and the future direction of MOF based therapeutics.

1.2 Introduction

Beginning in the late 19th to early 20th century, scientists proposed that illnesses could be treated through biological recognition. Early research in this area involved designing drugs themselves as the primary targeting agent to diseased tissues, but around the mid-1960s, the concept of incorporating drug molecules into drug delivery systems (DDSs) was introduced to improve drug stability and solubility. DDSs are materials designed to contain, in some fashion, therapeutics that can be delivered to a target site without unnecessary systemic distribution. While many materials and types of DDSs have been proposed, the nano-therapeutic approach to DDSs began gaining popularity in the late 1980s, after years of development of macro and micro-scale systems, such as, therapeutic patches and implants.[7] While these larger drug packaging methods proved useful for certain illnesses, the discovery of nanoparticulate accumulation in tumor tissue (termed the enhanced permeation and retention, EPR, effect) made clear the need for more research at the nano-scale, specifically for cancer research. With the birth and growth of nanotechnology in recent decades, investigation of nano-materials for biological applications has skyrocketed. As such, the term nanomedicine is currently used across many disciplines to describe the medical applications of nanoparticles whose sizes may range from 50-200 nm. Most recently, nanomedicine is aimed at nano-carriers that are capable of not only delivering a drug cargo but also capable of diagnostic imaging. These DDSs are termed theranostics, that is therapy and diagnostics combined in a single system. Overall, the most ideal theranostic

nanomedicines should demonstrate three-fold functionality: 1) *in vivo* targeting, resulting in 2) site specific drug delivery, and lastly 3) medical imaging to aid in diagnosis. Also, although there are several possible routes for the introduction of nanomedicines to the human body, when discussing nanomedicines and their implementation as theranostic DDSs, dialogue generally assumes oral or, more practically, intravenous administration as is the case in this chapter.

Liposomes,[8-10] micelles,[11-12] and inorganic nanoparticles[13-15] are among the most popular nano-materials currently studied as DDSs, with a large portion of these systems being polymeric conjugates.[16-17] As mentioned, the advantage of these DDSs is their ability to deliver otherwise insoluble drugs to intended exchange sites in the body. The clinical success of Abraxane (nanoparticle albumin-bound paclitaxel) and Doxil (liposomal encapsulated doxorubicin) demonstrates the potential of nano-carrier DDSs, however, current nano-carriers generally exhibit low drug loading capacities (5-6 wt%),[18] thereby requiring larger quantities of carrier material to deliver the proper amount of drug. In addition, most of these vesicular and inorganic systems suffer from what is known as the "burst effect", that is, the initial release of large amounts of loaded drug cargos. To address these issues, researchers are investigating other types of materials that may be capable of higher drug loadings and more controllable drug release. Hybrid metal-organic framework (MOF) materials are leading many of these efforts due to advantageous properties including permanent porosity and high pore volumes.

The popularity of MOFs as DDSs has greatly expanded within the last decade. Several reviews in the literature highlight MOFs in biomedical applications,[18-25] with an emphasis on drug delivery. Due to their high porosity and surface area, MOFs offer high drug loading capabilities (140 wt % has been reported)[2] and are being studied for controlled release of various drugs. In addition, post-synthetic modifications (PSMs) involving the attachment of targeting

moieties to direct nanoparticles to an active site and/or to impart imaging capabilities offer an avenue to enhance the functionality of MOF nanomedicines. Finally, the incorporation of proper metal centers into the MOF structure can also offer the integrated advantage of diagnostic imaging, resulting in theranostic MOF DDSs that are capable of dual mode benchtop and medical imaging. Figure 1.1 provides a general example of an advanced MOF nanoparticle for theranostic nanomedicine.

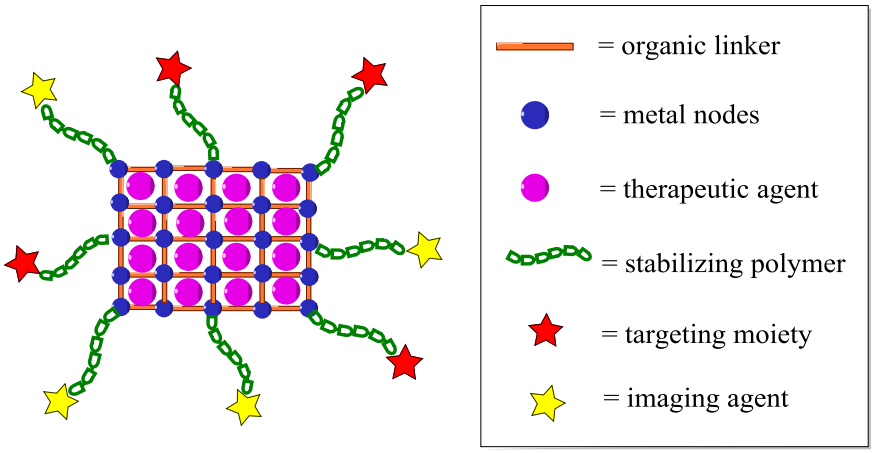

Figure 1.1 A generic schematic of a theranostic MOF material.

1.2.1 Designing MOFs for Biological Applications

The design and development of any marketable material for therapeutic applications requires a long, laborious, multi-step process intended to ensure the safety of patients. Therefore, many factors should be considered when devising a MOF DDS, and this section will highlight the aspects of MOF design that relate to the development of MOF nanomedicines. As this section attempts to outline, the eventual implementation of MOFs in nanomedicine will require the collaborative efforts of many researchers in a range of specialized fields.

Often, the expression "metal-organic framework" is used as a blanket term for hybrid metal-organic materials whose structures are comprised of extended and repeating coordination bonds (coordination polymer) and may be crystalline or amorphous. The International Union of Pure and Applied Chemistry (IUPAC) defines MOFs as 1, 2, or 3 dimensional coordination networks whose configurations possess potential voids and so, ambiguity often results.[26] In this discussion, and throughout this chapter, a distinction between purely crystalline MOFs and coordination polymers (often amorphous materials) will be made, with a focus on the crystalline systems.

1.2.2 The Starting Materials

The potential diversity of MOF materials is immense and arises from the sheer number of possible combinations devised from the choice of metal and organic linker. There are several factors to consider, however, when choosing the starting components of a MOF intended for biological applications. Most obviously is the choice of metal, as many transition metals have known harmful effects. Although some preliminary studies have employed problematic transition metals (Cr for example in the case of MIL-101 and MIL-100, MIL = Materials of Institue Lavosier)[2], the metal should be relatively biocompatible. Advantageous metals include Fe, Mg, Zr, and Ca (among others), whereas metals to avoid are known toxins, such as Cr, Pb, and Cd. Furthermore, although the metal is often benign, they may be chosen to provide some function to the final DDS. For example, the incorporation of Gd^{3+} and Mn^{2+} can offer magnetic resonance imaging (MRI) contrast capabilities, discussed further in Section 1.5. Table 1.1 lists commonly used metals in MOFs for biological applications and benefits of their incorporation.

Metal	Function
Ca^{2+}	None
Zr^{4+}	CT contrast
Zn^{2+}	None
Fe^{3+}	MRI contrast
Mn^{2+}	MRI contrast
Gd^{3+}	MRI contrast
Hf^{4+}	CT contrast
Tb^{3+}	Optical imaging*
Eu^{3+}	Optical imaging*

Table 1.1 List of commonly used metal in biological MOFs. *Metal introduced via post-synthetic doping.

A detailed study from Horcajada and co-workers[27] investigated 14 commonly used MOFs for biological applications, and found the most toxic to the cell lines chosen (human cervical cancer, HeLa and mouse macrophage, J774) were Zn-based, whereas the least toxic were Fe-based. These results were rationalized due to competition of Zn^{2+} with Fe^{2+} and Ca^{2+}, which would result in modulating metabolically important iron and calcium ion channels leading to cell damage. Another factor relevant to the metal design of MOF DDSs involves the consideration of dosage restrictions and final administration doses so that the tolerable intake of the metal is not exceeded. Although the dosing characteristics and pharmacokinetics must be investigated before successfully marketing a MOF DDS, dosing restriction is not currently a concern to researchers due to the infancy of MOF nanomedicines along with the low metal densities of highly porous MOFs used for drug delivery applications.

An appropriate linker for MOF materials should have at least two chelating moieties in order for self-assembly of the MOF structure. Commonly, carboxylates are employed as the chelating group with others being suitable as well (e.g. phosphonates). The ultimate choice of linkers for a MOF depends on their intended role. Most often in MOF DDSs, the organic

component serves only as the structural backbone of the material. However, there are reports of linkers chosen for other purposes, including linkers that serve as an avenue to attach (via PSM) additional functionality[28-29] and structural linkers that function as the actual therapeutic component.[30-33] For example, a report from Reiter et al. demonstrated the release of a prodrug, *c*,*c*,*t*-(diamminedichlorodisuccinato)Pt(IV) (DSCP) that also provided the backbone for a Tb^{3+} based coordination polymer.[30] Additionally, materials may be made of more than one linker referred to as co-linkers. As an example, "bio-MOF-1", reported by Rosi and co-workers, consists of adeninate and biphenyldicarboxylate co-ligands forming a highly crystalline MOF with a surface area of ~1700 m^2/g.[34]

Furthermore, linkers can be chosen based on the desired pore space/volume of the final product. As a general rule, MOFs made from longer and larger struts can typically crystallize with higher pore volumes and larger accessible pore diameters. If the target drug for encapsulation is known, drug size and pore dimensions become important factors to consider in selection of the organic component. While larger pores are advantageous to loading drug cargos, an upper limit to these dimensions must exist, as larger pores could result in unwanted rapid and premature diffusion of loosely encapsulated drug molecules. Additionally, longer struts tend to result in materials with decreased structural stability which is also an aspect of concern. Finally, some linker-metal combinations have been shown to undergo a "breathing" effect (changes in pore dimensions) when placed in different solvents, which could offer the added benefit of better securing drug cargos and helping to control drug delivery.[35-36]

The toxicity of the organic component should be considered. Not only should developmental efforts be concerned with the linker toxicity itself, they should be aware of possible *in vivo* degradation products resulting from metabolism of the material. The commonly

employed aromatic carboxylates, specifically benzene dicarboxylate (BDC aka terephthalic acid) and its functionalized derivatives, are the most extensively utilized linkers in MOF DDSs. These linkers are assumed to degrade into benzoic acid, which is metabolized by butyrate-CoA ligase and glycine N-acyltransferase to hippuric acid that is excreted in urine.[37] Additonally, benzoic acid occurs naturally in many plant species and its salts have been used as food preservatives with a tolerable intake of 5 mg/kg/day for humans. For these reasons, the BDC based linkers are considered relatively non-toxic when at reasonable dosing limits of the final DDS as previously mentioned. While a comprehensive list of all linkers used is not practical here, Table 1.2 provides a list of commonly employed linkers in biologically relevant MOFs, mostly represented by the MIL (Materials of Institut Lavoisier) family of MOFs.

Linker	MOF common names	Linker function
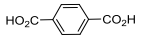	MIL-101 MIL-53 MIL-88B	Backbone Flexible backbone
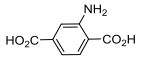	MIL-101_NH_2 MIL-53_NH_2 MIL-88B_NH_2	PSM Flexible backbone
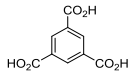	MIL-100	Backbone
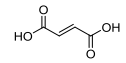	MIL-88A	Flexible backbone
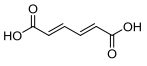	MIL-89	Flexible backbone
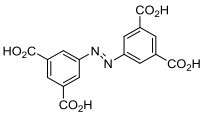	MIL-127	Backbone
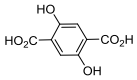	CPO-27	Backbone
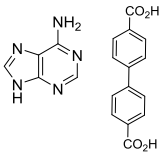	bio-MOF-1	Backbone

Table 1.2 List of commonly employed linkers in biologically relevant MOFs.

Finally, like conventional drug development, all reagents used in the synthesis of biologically applicable MOF materials must be accounted for. For example, toxic solvents often used to synthesize MOF materials (e.g. DMF) can be avoided or completely removed upon solvent exchange and evacuation. Additionally, harsh chemicals that may be introduced via PSM or coating techniques must be eliminated from the final MOF product. Overall, when taking all afore mentioned synthetic parameters into consideration, the design and development of MOF DDSs may seem like an intimidating task. However, with collaborative research efforts, MOF materials as DDSs have shown tremendous potential and continue to progress in the field of nanomedicine.

1.2.3 Synthesis of nano-MOFs

In order to be applicable in nanomedicine, MOFs must be engineered on the nano-scale. The acceptable range for particle sizes is generally 50-200 nm (final product formulation). The lower limit of this range, particularly for cancer research, ensures particles that are capable of "passive targeting", that is, accumulating in tumor tissues via the EPR effect (See Section 1.4.2). While the discovery of the EPR effect has offered researchers a lower limit to consider, DDSs should not surpass 200 nm if they are to travel through the blood stream, in order to avoid the possibility of obstructing circulation.[18]

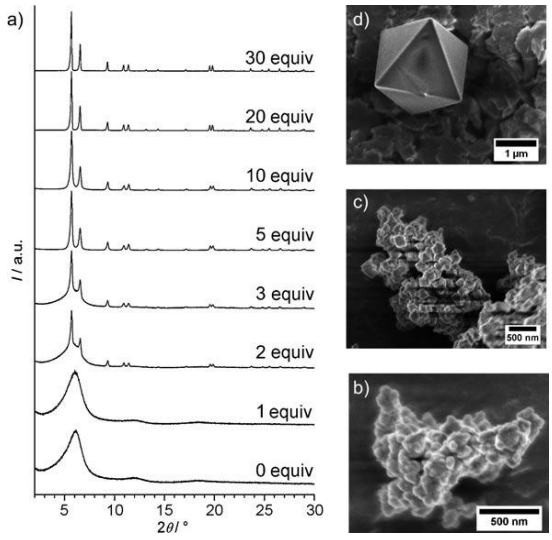

Figure 1.2 Demonstration of the modular approach to solvothermal NMOF formation using a UiO-67 example. a) PXRD patterns of UiO-67 at varying concentrations of modulator (equiv = mol modulator : mol Zr^{4+}). SEM images of material formed from b) 0, c) 3, and d) 30 equivalents of benzoic acid. This image was reprinted with permission from reference 48. Copyright © 2011 Wiley-VCH Verlag 6644 GmbH&Co. KGaA, Weinheim.

The ability to synthetically control particle sizes and shapes is paramount in the design of MOF DDSs. A wide range of different morphologies of nano-scale MOFs (NMOFs) have been accomplished via solvothermal,[38-41] microwave,[42-45] and micro-emulsion[5, 46-47] techniques. The most common is the solvothermal method, in which the metal and the linker are combined in a sealed vessel and heated in a solvent at elevated temperatures for a given period of time. While this technique provides simplicity, it can be synthetically challenging to fashion NMOFs in this way. One method to combat this is via the use of "modulators". Modulators, or "crystallization promoters", are typically monocarboxylates, such as benzoic acid, acetic acid, and formic acid that serve to bind competitively with the linker to metal nodes. This competitive binding results in crystalline MOFs; where often, if no modulator were present, only amorphous material would result. The example presented in Figure 1.2 demonstrates the modular approach for the synthesis of a Zr^{4+} based MOF incorporating biphenyl-4,4'-dicarboxylic acid (bpdc) as the linker, UiO-67

(UiO = University of Oslo). By varying the concentration of the modulator, particle sizes can also be controlled,[48-49] where an increase in modulator concentration typically results in larger particles. A reason for this relationship is at lower concentrations of modulator, MOF nucleation is favored, resulting in more nucleation sites. A consequence of increasing the number of nucleation sites is a reduction in crystal growth, thus more particles are produced which are smaller at lower concentrations of modulator (Figure 1.2).[48] The synthetic temperature also plays a significant role in solvothermal preparations. As expected, increasing the temperature usually results in faster crystallization kinetics which can result in smaller particles. A report from Ragon et al. studied the effect of temperature on the crystallization kinetics of Zr-based UiO-type materials and found that increasing the temperature does indeed increase the rate at which these MOFs crystallize, however, this was not the case for shorter linkers.[50] One rationalization for this is that the solubility of the linker increases at higher temperatures for the longer linkers but is not a limitation for shorter ones.

Microwave and micro-emulsion methods for the formulation of NMOFs are not as common. Microwaves have been widely used in chemical synthesis to reduce synthetic times and improve overall yields. While conventional heating relies on convection to radiate heat, microwaves interact with individual solvent molecules leading to localized "hotspots" throughout the synthetic medium.[42] Depending on the nucleation and crystal growth kinetics of the system, these "hotspots" can act to promote MOF nucleation, thus hindering crystal growth and resulting in NMOFS.

Micro-emulsions, commonly used to synthesize polymers, are becoming increasingly popular for MOF synthesis, and are essentially micellular mother solutions composed of solvent and a surfactant in a defined molar ratio (known as the W value, or water to surfactant ratio).

Emulsions comprise micelles in colloidal suspension that encapsulate starting materials. In a typical reverse phase (water in oil) micro-emulsion synthesis, Figure 1.3, two separate emulsions are made, one containing the linker, the other the metal salt. The two emulsions are then combined and allowed to react in either an open or closed system at varying temperatures for a given amount of time. Qian et al. have shown that different morphologies and particle sizes can be achieved by varying the W value.[47] Lin and co-workers have also shown the same control by altering the reaction temperature.[51] While the particle shapes (long nanorods) in some of these syntheses may not be ideal, the ability to control particle sizes and shapes via the use of micro-emulsions offers additional techniques for the formation NMOFs.

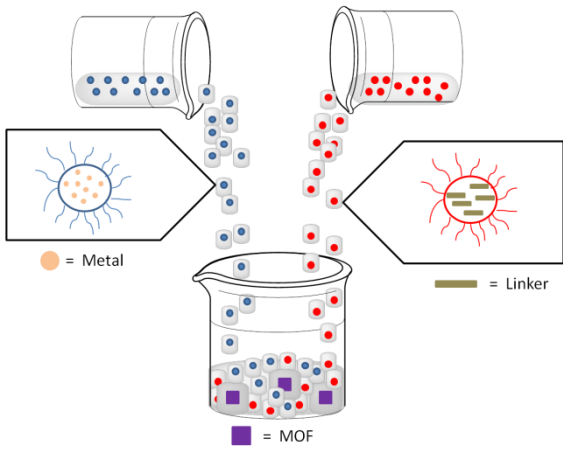

Figure 1.3 Diagram of a typical micro-emulsion synthesis.

1.2.4 Stability and Biodistribution

To realistically deliver drug cargos via MOF nanomedicines, premature drug release must be avoided. This brings into question the issue of material stability in biologically relevant solvents. Most MOF materials incorporating carboxylate chelating functionalities are not stable in aqueous media due to the hydrolysis of metal-carboxylate bonds. In addition, the presence of

buffers used to mimic the conditions in blood results in faster material degradation and thus, premature drug release. A report from Serre and co-workers[52] suggests that a majority of the MOFs currently studied as drug delivery agents do indeed degrade rapidly in biological media as evidenced by powder X-ray diffraction (PXRD).[52] There are techniques to avoid this intrinsic instability; for example, the utilization of surface coatings can offer stabilization, addressed further in Section 1.4.1. Although not currently explored, the stability issue may also be addressed by changing the chelating component of the linker to moieties that bind stronger to metal nodes. This can be rationalized and supported by the hard-soft acid-base (HSAB) theory. For example, Zr^{4+} is a hard acid and although the carboxylate anion is a hard base, there may be other bases that are harder (e.g. phosphonates) and would bind stronger to the $Zr_6O_4(OH)_4$ nodes found in UiO-type MOFs. Stronger binding interactions would result in materials that are not as susceptible to degradation especially in phosphate buffered biological media.

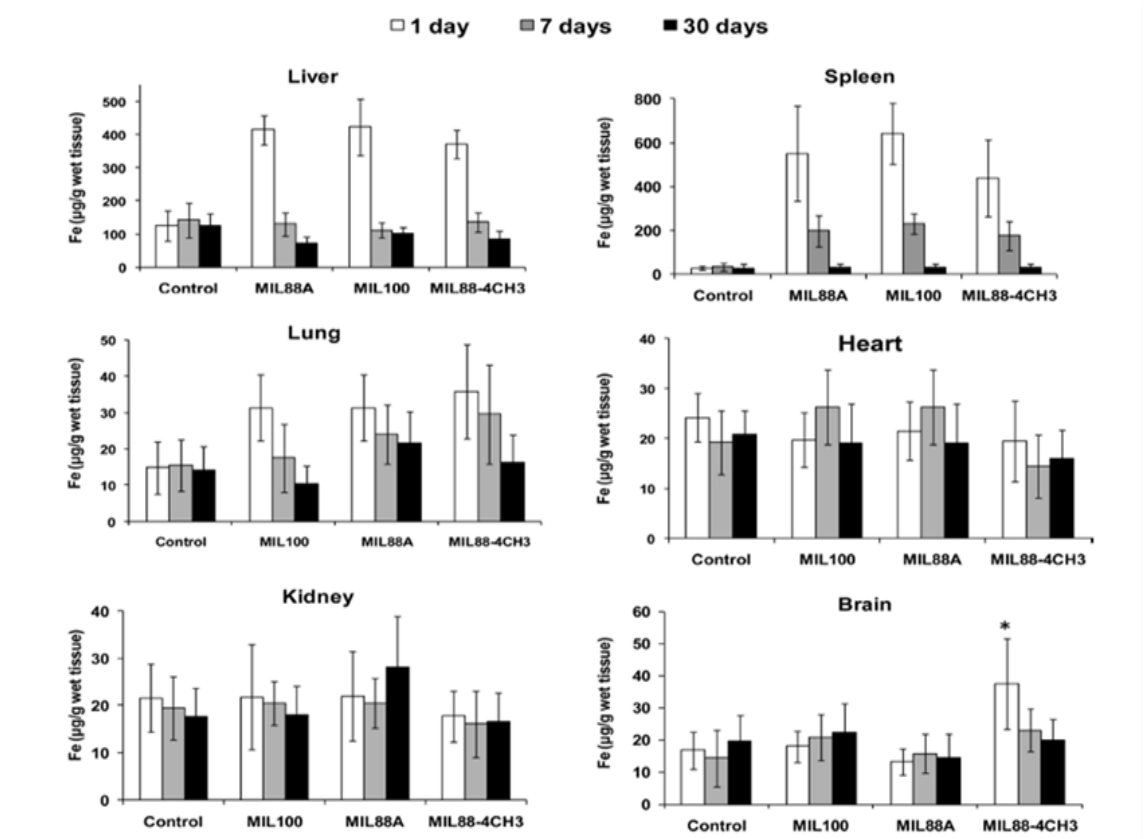

Figure 1.4 Iron levels in different tissues after 1, 7, and 30 days of i.v. administration of nanoparticles of MIL-88A, MIL-100, MIL-88B_CH_3. Reprinted with permission from reference 18. Copyright © 2012 American Chemical Society.

While extremely rapid degradation is not advantageous, the material should exhibit some level of instability in order to be metabolized and expelled from the human system. Material metabolism and excretion is essential to avoid material accumulation in biological tissues. To address this issue, the Serre group has monitored the fumaric acid (linker component of MIL-88A) concentration in several Wistar rat organ tissues.[53] By evaluating urine, liver, and spleen tissues over a period of 24 hours, they observed accumulation in the liver and spleen, suggesting that MOFs are not immediately metabolized. In another study, the same group demonstrated that a series of iron-carboxylate MOFs are expelled from these organs (liver and spleen) after 24

hours and long-term accumulation (30 days) of iron occurs mostly in lung, heart, and kidney tissues, Figure 1.4.[18]

1.3 Drug Loading and Release

The purpose of using MOF materials for DDSs lies in their incredibly high surface areas, varying pore sizes, and synthetic tunability. These porous properties have afforded drug encapsulation and release that exceeds their inorganic and polymeric counterparts (5-6 wt% vs. 140 wt% for MOF materials). Synthetic manipulation of these materials can also aid in the uptake of hydrophilic, amphiphilic, and hydrophobic drug classes. In addition, organic moieties in MOF structures facilitate an affinity for drug molecules, which are by far, largely organic compounds.[19]

1.3.1 Drug Loading

Due to strict control and cost of potent and patented drugs, researchers often turn to common and inexpensive substances that exhibit biological activity to explore drug loading capacities, such as ibuprofen and caffeine.[2, 18, 54-57] Ibuprofen (IBU), in particular, is a cost effective and readily accessible model drug. It has been used for drug encapsulation/release studies in several types of materials.[58-60] A most impressive encapsulation of 1.4 g IBU/g MIL-101 was demonstrated by the Ferey group.[2] This MOF demonstrated significantly higher IBU loading than MIL-100 (0.35g IBU/g MIL-100), which was attributed to the differences in pore diameters, with the larger diameters (25-29 Å and 25-34 Å for MIL-100 and MIL-101 respectively) capable of higher loading.[18]

Drug	BioMIL-1	bio-MOF-1	MIL-53	MIL-88A	MIL-89	MIL-100	MIL-101	MIL-101_NH_2	MOF-1	UiO (amino-TPDC)	UiO-66	UiO-66_NH_2	ZIF-8
acetominophen	–	–	19.7	–	–	–	19.7	–	–	–	–	–	–
azidothimidine	–	–	–	–	–	6.1	–	–	–	–	–	–	–
azidothimidine triphosphate	–	–	0.24	0.60	–	21.2	–	42.0	–	–	–	–	–
benzophenone 3	–	–	–	–	–	15	–	–	–	–	–	–	–
benzophenone 4	–	–	5	–	–	15.2	–	–	–	–	–	–	–
busulfan	–	–	14.3	8.0	9.8	25.5	–	–	–	–	–	–	–
caffeine	–	–	23.1	–	–	24.2	–	–	–	–	2.2[β]	1.2	28
calcein	–	–	–	–	–	–	–	–	–	–	4.9	–	–
cidofovir	–	–	–	2.6	14	16.1	–	41.9	–	–	–	–	–
cisplatin (or prodrug)	–	–	–	–	–	–	–	12.8	–	12.3	–	30.7	–
doxorubicin	–	–	–	–	–	9.1	–	–	–	–	–	–	4.9
5-flurouracil	–	–	–	–	–	–	–	–	36.9	–	–	–	66
ibuprofen	–	–	–	–	–	35	140	–	–	–	2.1[β]	3.1	–
nicotinic acid	71.5[α]	–	–	–	–	–	–	–	–	–	–	–	–
procainamide	–	22	–	–	–	–	–	–	–	–	–	–	–
progesterone	–	–	19.6	–	–	–	20.2	–	–	–	–	–	–
stavudine	–	–	20.0	–	–	–	20.2	–	–	–	–	–	–
topotecan	–	–	–	–	–	33	–	–	–	–	–	–	–
urea	–	–	63.5	–	–	69.2	–	–	–	–	–	–	–
Ref	**33**	**34**	**19, 36**	**19**	**19**	**18, 19, 2, 63**	**2, 36**	**19**	**98**	**58**	**56, 62**	**56, 57**	**52, 58, 75**

Table 1.3 Maximum loading (wt %) for drugs encapsulated in MOFs. α) incorporated as the structural component of the MOF. β) loading reported for the mono-brominated derivative.

Other drugs encapsulated into MOF materials include challenging species that exhibit poor biodistribution due to solubility and stability limitations in biological media; for example, azidothimidine triphosphate (AZT-Tp), cidofovir (CDV), busulfan, and doxorubicin.[19, 61-63] By incorporation of these agents into DDSs, these limitations can be overcome. Yet another noteworthy drug of interest for encapsulation into MOF DDSs is cisplatin.[18, 30, 64] Cisplatin is a powerful anti-cancer agent that has excellent solubility and biodistribution; however, it is also highly toxic to healthy cells. By incorporating cisplatin into DDSs that can offer homing capabilities, the drug may be delivered only to nefarious tissues, thereby negating the undesirable side effects that result from systemic distribution. Table 1.3 provides a comprehensive list of the

drugs loaded into MOF materials to date and the maximum reported loading (wt %) for each drug-MOF combination.

Encapsulation studies usually begin by suspending the dehydrated material into a solution containing the drug of interest, also referred to as the impregnation method. The solution is then allowed to stir in a volatile solvent (for eventual evacuation) for a given time period. The solid material is recovered, washed and dried, and loading is confirmed using thermogravimetric analysis (TGA), powder X-ray diffraction (PXRD), and UV-Vis absorption spectroscopy techniques.[2, 19] Other, less common, methods by which drugs are incorporated are via direct integration of drug moieties as the structural component[30, 33] of the MOF and by introducing the drug of choice into the synthetic broth.[55, 65]

The affinity of drug molecules to the pore spaces of MOF materials is not completely understood but is assumed to be dependent upon pore size, volume, and shape, in addition to drug-MOF host interactions. Energy calculations of IBU conformations inside two porous MOFs (MIL-101 and UMCM-1, UMCM = University of Michigan crystalline material) suggest the lowest energy conformation orients the carboxylic acid group of IBU toward the metal site.[66] These calculations were consistent with experimental PXRD and NMR results, suggesting the metal sites in these porous MOFs play a role in small molecule adsorption.[67-68] Although metal sites must surely play an important role in drug adsorption in some MOFs, the nature of the linker also significantly affects drug affinity as well. In a recent study of caffeine uptake in MIL-88(Fe), it was shown that linker functionalization had a significant effect on the loading capacity of the MOF, Figure 1.5.[69] MOFs with more hydrophilic alcohol and amine groups demonstrated better caffeine uptake, suggesting that hydrogen bonding is a contributing factor. While these

studies elucidate some factors affecting drug affinity in MOF materials, the individual dynamics of each drug-MOF combination will be different.

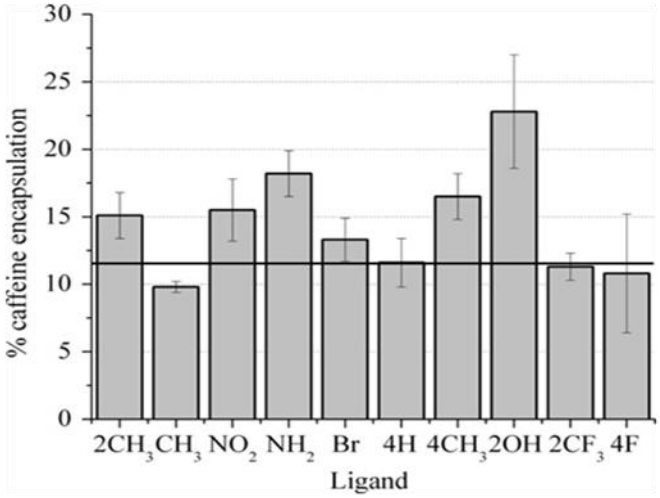

Figure 1.5 Caffeine encapsulation (wt%) via the impregnation method of MIL-88(Fe) materials with various functional groups on the backbone linker. The black line represents the encapsulation of unfunctionalized MIL-88(Fe) particles. Reprinted with permission from reference 69. Copyright © 2011 Elsevier Inc.

1.3.2 Drug Release

Once maximum uptake is observed (no additional loading occurs with extended loading time) the loaded MOF material is suspended in simulated body fluid (SBF) or phosphate buffered saline (PBS) and release is observed using PXRD, HPLC, and UV-Vis spectroscopy techniques.[2, 18, 35] The release of drugs from most MOF materials seems to occur via drug diffusion or a material degradation mechanism, or perhaps, as a result of both processes. In the case of drugs anchored into the pore spaces via non-covalent interactions, the mechanism of drug delivery is most likely dominated by MOF degradation. As a demonstration of this, Serre and co-workers measured the release of caffeine from a series of popular MOFs in deionized water and phosphate buffered saline (PBS), Figure 1.6.[52] They observed enhanced release in the PBS

media and PXRD confirmed more rapid degradation under those conditions as opposed to the deionized water. Often in the MOF literature, a "burst" effect is evident by the abrupt release of large amounts of drug cargo that usually slows after the first hour. Despite the observed burst effect, the initial reports of drug release from MOF materials have laid the foundation in the field, but more studies are needed to address the key issue of stability. Extreme stability of nano-carriers is undesirable however, as the biological system must have a method to eliminate or metabolize the nano-carriers once the drug cargo is fully depleted.

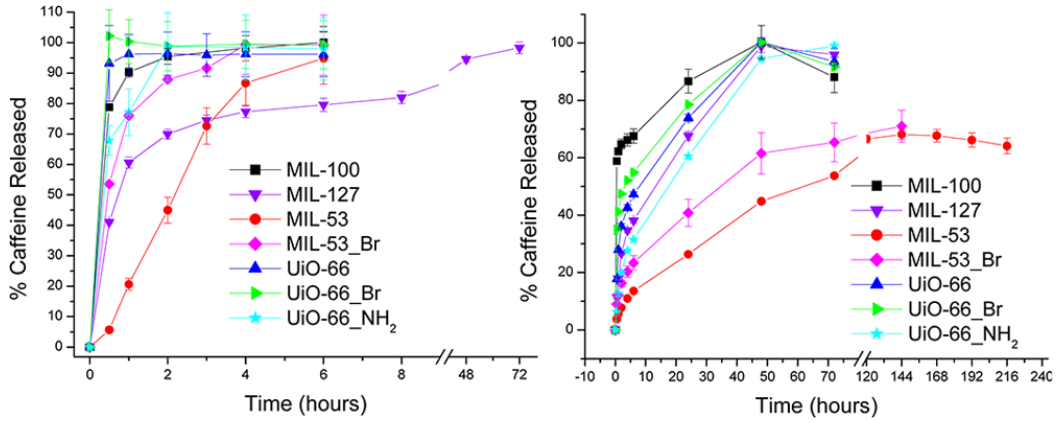

Figure 1.6 Caffeine release from MOF materials in PBS (left) and deionized water (right) at 37 °C. The x-scale should be noted and release occurs much faster in PBS due to the instability of the MOF materials in this media. This image was copied with permission from reference 52. Copyright © 2013 American Chemical Society.

Instability of MOF materials in aqueous environments results in drug release mechanisms that cannot be controlled. While some reports claim controllable release from MOF materials, there are only a few reports of drug delivery from MOF materials that is managed via an external stimulus. The first was from Rosi et al.[34] who demonstrated procainamide release from a Zn-adeninate MOF, bio-MOF-1. The release of procainamide was stimulated by sodium cation exchange with the procainamide electrostatically bound to the anionic MOF, and complete

release was achieved after 72 h. In other reports from Tan and co-workers,[70-72] the UiO-66-NH_2 and UMCM-1-NH_2 MOFs were post-synthetically functionalized with pyridinium stalks capped with carboxylatopillar[5]ene (cyclic macromolecules comprised of benzene derivatives linked in the para position) moieties. Upon pH activation, heating, or competitive binding (with Zn^{2+}, Ca^{2+}, and methylviologen salts), the model drug rhodamine 6G (Rh-6G) or 5-fluorouracil encapsulated within the MOF was released due to disruption of the pillarene capping units. While these reports, and others,[65, 71, 73-75] were the first to demonstrate "stimuli-responsive" release from MOF materials, most rely on ionic exchange in solution for drug release to occur. Therefore, upon placement in blood serum, the drug release from these materials would take place immediately and mechanisms by which these systems offer controlled release would be irrelevant. Table 1.4 provides a list of the release parameters and times of some benchmark MOFs.

MOF	Drug	Release Conditions			Ref
		Max release time	Temp. (°C)	Solvent	
BioMIL-1	nicotinic acid	1 h	37	PBS	**32**
bio-MOF-1	procainamide	5 d	25	PBS	**34**
MIL-53	ibuprofen	21 d	37	SBF	**35**
	acetominophen	6 d	37	PBS	**36**
	progesterone	5 d	37	PBS + 0.5%SDS	**36**
	stavudine	5 d	37	PBS	**36**
MIL-100	ibuprofen	3 d	37	SBF	**2**
	cidofovir	5 d	37	PBS	**19**
	AZT-Tp	5 d	37	PBS	**19**
	doxorubicin	12 d	37	PBS	**19**
	topotecan	5-7 h	37	PBS	**63**
MIL-101	ibuprofen	6 d	37	SBF	**2**
	acetominophen	6 d	37	PBS	**36**
	progesterone	5 d	37	PBS + 0.5%SDS	**36**
	stavudine	5 d	37	PBS	**36**
UiO-66	caffeine	4 d	25, 40	water	**74**
	procainamide	4 d	25, 40	water	**74**
	calcein	2 d	37	PBS	**62**
ZIF-8	caffeine	3 d	25	water	**62**
	doxorubicin	30 d	25	PBS	**61**
	5-flurouracil	12 h	37	PBS + acetate	**75**

Table 1.4 Release conditions of various benchmark MOFs.

1.4 Post-synthetic modifications

Post-synthetic modifications (PSMs), are chemical transformations performed on MOFs that serve to impart additional functionality to the final MOF system. These modifications can range from covalent attachments of active moieties or coatings designed to envelop the MOF material. Although there are many reports of PSMs to MOF materials, only a small fraction address NMOFs for DDS applications. As PSMs relate to DDSs, they include surface coatings and the attachment of targeting moieties. For more comprehensive reviews of PSM techniques, the reader is directed to the literature.[76-77]

1.4.1 Surface Coatings

In order to ensure stability in blood plasma, DDSs are often functionalized with stabilizers to avoid rejection and elimination by blood proteins. Surface coatings can also prevent NMOF aggregation and increase their ability to be suspended in aqueous formulations. Additionally, polymeric coatings may serve to slow drug release and eliminate "burst effect" phenomena observed for some NMOFS. Biodegradable polymers are typically used and while many polymers have been used to coat different types of nanoparticles, there are three main approaches when modifying the surfaces of NMOFs for DDSs. These approaches are coating with polyethylene glycol (PEG), polyvinylpyrrolidone (PVP), or silica shells, and in some cases, a combination of these may be employed. Coating with PEG is commonly referred to as "PEGylation". This method works by functionalizing the surface of the NMOF with a PEG shell by simply allowing the particles to stir in a solution of PEG.[78-80] Most often, a nanoparticle suspension is formed by sonicating in a solution in which PEG is soluble. A suspension is necessary in order to ensure that individual particles are coated and not agglomerates. PEG is then added to the solution and allowed to self assemble around the nanoparticles. PVP coatings are achieved in a similar manner.[81]

Silica shells can be easily grown on the surface of NMOFs whose surfaces are usually first coated with PVP or PEG.[30, 80, 82] Because the formation of the silica shell involves suspending the materials in ethanol in the presence of tetraethoxysilane (TEOS) and ammonia, the polymer is necessary to facilitate this process and to prevent aggregation.[83] Should the naked NMOFs suspend easily and evenly in ethanolic solutions, and be stable to the silica growth reaction conditions, the polymer may not be necessary.[83] The thickness of the silica shell can

also be controlled by varying the reaction time, as elegantly demonstrated by Lin and co-workers[81] where they varied the thickness of a silica shell on $Ln(BDC)_{1.5}(H_2O)_2$ (where Ln = Eu^{3+}, Gd^{3+}, or Tb^{3+}) nanoparticles from 2-3 nm to 8-9 nm by increasing the reaction time from 3 h to 7 h, respectively, Figure 1.7.

Less common functionalizing species include isopropylacrylamide-methacrylate copolymers[84] and 1,2-dioleoyl-sn-glycero-3-phosphate (DOPA),[85] among others. These coated nanoparticles may then be further functionalized with cell targeting proteins that enhance endocytosis or with imaging agents as highlighted in subsequent sections. Regardless of the stabilizer choice, the particle size must remain under consideration when developing marketable DDSs. Developmental efforts should consider all particle layers such that the final system does not exceed the desired 200 nm.

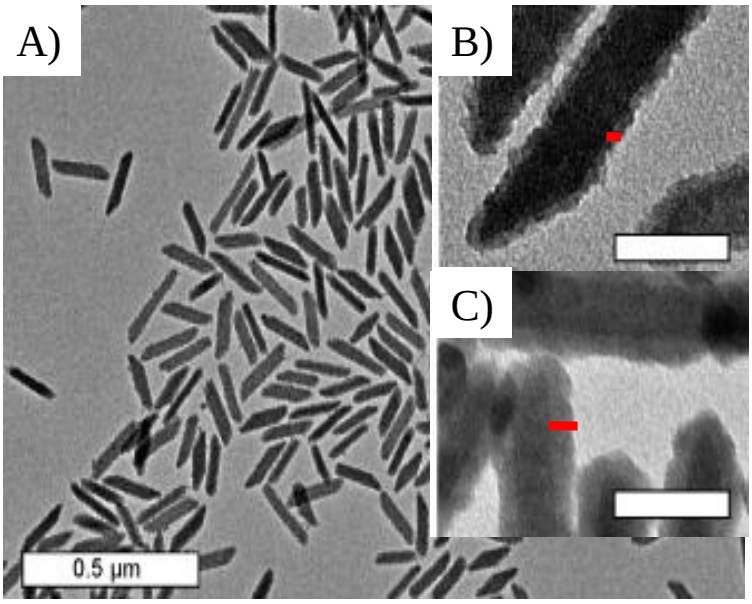

Figure 1.7 TEM images of $Ln(BDC)_{1.5}(H_2O)_2$ nanoparticles coated with A) and B) 2-3 nm silica coatings and with a C) 8-9 nm coating. The red bars are provided for clarity. Scale bars are 50 nm unless otherwise indicated. This image was adapted with permission from reference 81. Copyright © 2007 American Chemical Society.

1.4.2 Targeting

In order to achieve a *theranostic* MOF DDS, the material must be capable of *in vivo* targeting of an active site. There are two main approaches to imparting targeting functionality to these materials: passive and active targeting. Passive targeting is accomplished by fashioning nano-materials that accumulate at tumor sites via the EPR effect. The EPR effect was so named for the observation by Hiroshi Maeda that tumor vasculature is different than that of healthy tissue, and so, circulation through tumors results in the permeation and retention of nano-sized particulates (larger than ~50 nm).[86,87,88] In the late 1980s, Maeda was working with a copolymer conjugated anticancer protein, styrene maleic acid neocarzinostatin (SMANCS), when he found that the larger SMANCS exhibited higher accumulation and retention in the tumor he was studying than the neocarzinostatin (NCS) itself.[88] This led him to the realization that the larger copolymer conjugated system was more effective for selectively delivering the drug to the tumor site, due to the retention of macromolecules in tumor tissue by "leaky" tumor vasculature.[86] Most MOF DDSs in the literature utilize this form of targeting, mainly for synthetic simplicity.

Active targeting involves the attachment of proteins, or species designed to actively seek out diseased cells via biological recognition. While there are only a handful of active targeting agents that have been reported in the area of MOF nanomedicines,[5, 28, 80] by far the most common is the cyclic peptide cRGDfK which is known to bind to the $\alpha_v\beta_3$ integrin.[89] This integrin is overexpressed in angiogenic tumors and the result of cRGDfK binding inhibits the tumor from forming new blood vessels and thus, slows tumor growth.[28] Additionally, targeting the $\alpha_v\beta_3$ integrin allows a DDS to reach angiogenic tumors and release drug cargos in those areas, further retarding tumor growth and ultimately leading to cell death. Anisamide (AA) functionalized materials can also be used to target various cancer cells by binding to overexpressed sigma receptors. The attachment of anisamide (AA) to a polyethylene glycol (PEG) and silica (SiO_2)

coated Zr nano-MOF with an incorporated phosphorescent ruthenium linker has been shown to significantly enhance endocytosis in H460 human lung cancer cells, Figure 1.8.[80]

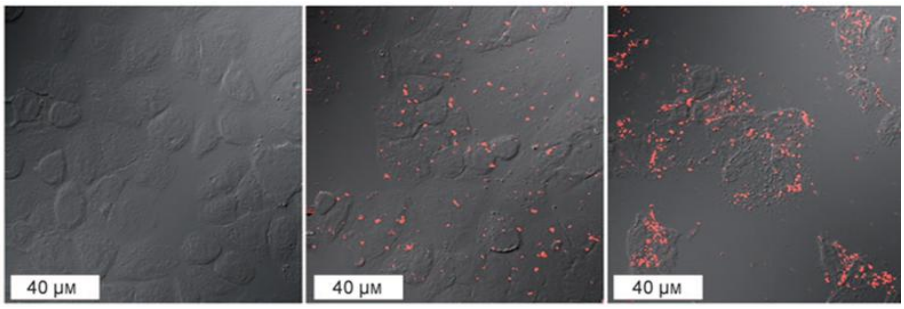

Figure 1.8 Confocal microscopy images of H460 cells incubated with no nanoparticles (left), with PEG coated nanoparticles without AA targeting (middle), and with nanoparticles containing AA targeting functionality (right). This image was taken with permission from reference 80. Copyright © 2011 Wiley-VCH Verlag GmbH & Co. KGaA, Weinheim.

1.5 Medical Imaging

There are many types of medical imaging techniques utilized as both *in vivo* and *in vitro* diagnostic tools. Advantages to *in vivo* imaging include real-time observation of therapeutic efficiency and the ability to monitor biodistribution of therapeutic agents. *In vitro* imaging on the other hand, allows a quick and easy tool to evaluate the practicality of a therapeutic agent before its *in vivo* introduction, and aids in overall understanding of medical illnesses from a research perspective. As these imaging modalities relate to current MOF DDSs, the most commonly explored are magnetic resonance imaging (MRI) for *in vivo* studies, and optical imaging for *in vitro* studies.

1.5.1 NMOFs as Contrast Agents for MRI and CT

Magnetic Resonance Imaging (MRI) is one of the most widely utilized medical imaging techniques due to its non-invasive nature and the facilitation of *in vivo* imaging without the need for radioactive modality.[90] In general, MRI is based on traditional nuclear magnetic resonance (NMR) where a subject is enclosed by an external magnetic field resulting in the alignment of active nuclei (mostly protons, H^1 in MRI) either parallel or anti-parallel to the external field. Application of electromagnetic radiation (whose frequency corresponds to the nuclei of interest) results in nuclear spin flips of the anti-parallel nuclei such that all nuclei become parallel to the external field. Once the electromagnetic radiation is removed, the flipped nuclei relax to their original alignment in the external field. This relaxation releases quantifiable energy and allows for the measurement of nuclear relaxation times (T_n), Figure 1.9.

Due to the high density of MRI active H^1 nuclei in the biological system, contrast agents are employed to enrich MRI images. Various types and/or hybrid systems have been proposed as MRI contrast agents including chelation complexes,[91-93] metal nanoparticles[94-96], polymers[97-100], and coordination polymers.[4, 51, 101] Several reviews in the literature discuss current state of the art MOF MRI contrast agents.[6, 23, 102] The effectiveness of a material for MRI contrast is measured by probing the increase or decrease of the proton relaxation times of water molecules that surround the nanoparticle. Generally, contrast agents are categorized into "positive" and "negative" enhancement agents. Positive agents are those that serve to increase the brightness of images, typically by shortening the proton *longitudinal* relaxation time (T_1). Alternatively, negative enhancement agents are those that serve to darken images by shortening the *transverse* (T_2) relaxation time; however, darkened images provided by negative contrast agents can be clinically confused with bleeding and calcification, and so, positive contrast agents are preferred.[103] These nuclear spin-decay times can be measured using appropriate NMR

instrumentation, and the inverse of the relaxation times, when plotted as a function of contrast agent concentration, gives the "relaxivity" (r_n) of a material, typically reported in units of $mM^{-1}s^{-1}$, Figure 1.9. It is this property of relaxivity that is used in the field to compare contrast agents and their capacity to function as competitive contrast agents.

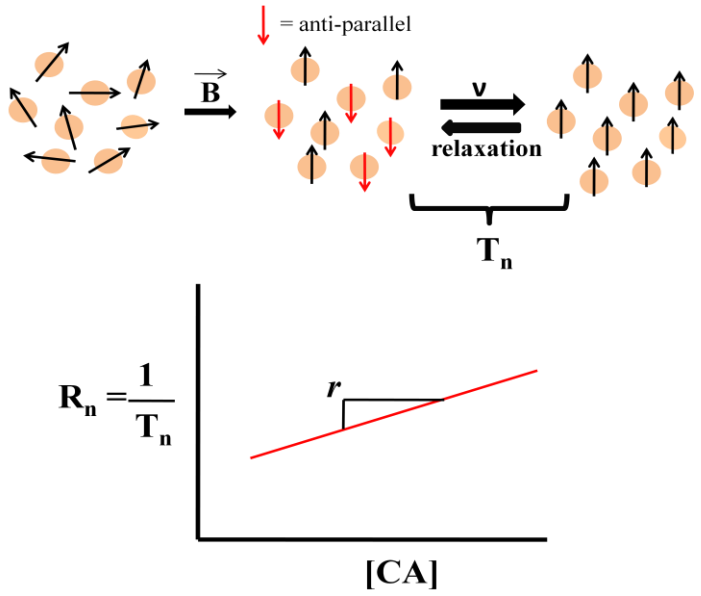

Figure 1.9 Top: Overall diagram of the theory behind MRI. Bottom: Mathematical demonstration of relaxivity, a property used to compare contrast agents.

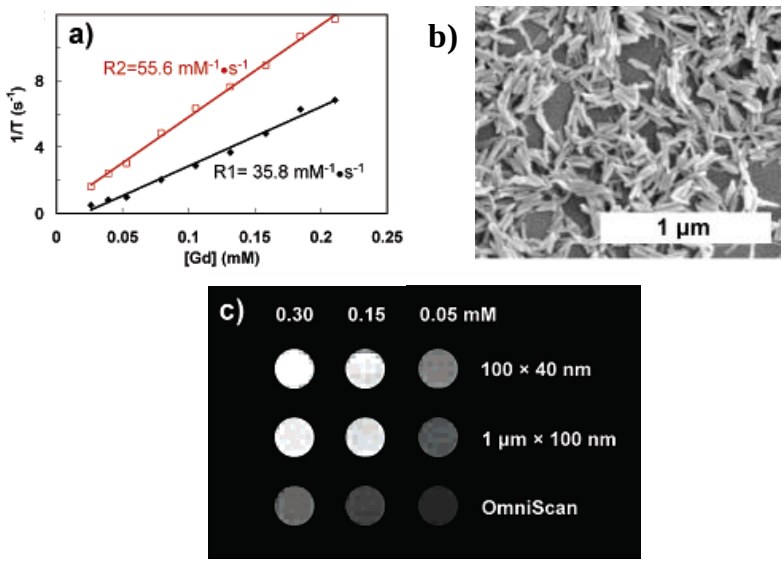

Figure 1.10 a) Relaxivity of Gd-BDC nanorods whose SEM images are shown in b). c) MRI contrast enhancement of Gd-BDC nanorods, demonstrated by brighter images with increasing concentrations of nanorods (top) as opposed to the contrast offered by equimolar concentrations of OmniScan (bottom). This image was adapted with permission from reference 6. Copyright © 2006 American Chemical Society.

Typical relaxivity ratios (r_2/r_1) values of marketed Gd^{3+} T_1-weighted contrast agents are below 2 and provide the target value when designing theranostic devices for MRI contrast. Lin and co-workers were the first to show MRI contrast ability of MOFs with a series of Gd-based (designated here as Gd-BDC and Gd-BTC) materials of differing sizes and shapes, incorporating benzene dicarboxylate (BDC) and benzene tricarboxylate (BTC) linkers.[6] The Gd-BDC nanorods (100 nm x 40 nm) exhibited a relaxivity ratio of 1.55, which is on par with the target value and, in fact, they demonstrated improved contrast compared to the clinically employed agent OmniScan, Figure 1.10. Gd-BTC nanoplates exhibited a higher ratio of 2.26. Their results also showed that the Gd-BDC nanorods could serve as both T_1 and T_2-weighted contrast agents, depending on the pulse sequence employed. The same group has also explored analogous Mn-based (designated here as Mn-BDC and Mn-BTC) MOFs,[5] whose relaxivity ratios were on the order of 14.5 and 30.7 for Mn-BDC nanorods and Mn-BTC nanoparticles, respectively. The Mn-

BTC nanoparticles were coated with a silica shell and functionalized with a cyclic arginine-glycine-aspartate (RGD) peptide labeled with a rhodamine B fluorophore. Despite objectionable relaxivity ratios, *in vitro* MRI images of HT-29 cells incubated with the coated Mn-BTC, showed slight positive contrast. These studies have laid the foundation for researchers to investigate MOFs as promising MRI contrast agents towards theranostic MOF nanomedicines.

X-ray computed tomography (CT) is another non-invasive medical imaging technique used for diagnosis and treatment. CT uses high energy X-rays that penetrate biological tissues and can afford 3-D images of hard and soft tissues. Depending on the atoms present, X-rays are absorbed by the subject and the difference between incident X-rays and those collected after tissue penetration can be measured and used to create an image.[104] Elements of higher atomic number (Z) are better at absorbing X-rays and so, contrast agents are employed in CT to provide soft tissue resolution in much the same way as MRI contrast agents. Traditionally, iodinated complexes or species are used, which has inspired the use of iodinated NMOFs for CT contrast. In a report from deKraft et al., I_4-BDC ligands were used to formulate Cu^{2+} and Zn^{2+}-based coordination polymers (CPs).[105] These materials exhibited up to 63 wt % iodine and the increased iodine density is advantageous for using CPs as opposed to molecular iodinated compounds. In other reports, high Z metals have been incorporated to offer CT contrast. For example, Zr and Hf based UiO-type MOFs were shown to brighten images at low concentrations (0.05 M) as well as the commercially used iodixanol, Figure 1.11.[78]

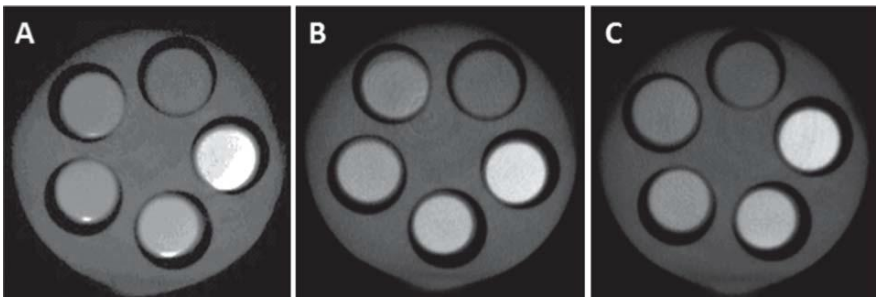

Figure 1.11 CT phantom images of (A) Hf-UiO, (B) Zr-UiO, and (C) iodixanol dispersed in water. From the top, counterclockwise, the slots have [Hf/Zr/I] = 0, 0.05, 0.10, 0.15, and 0.2 M. This image was copied from reference 78. Copyright © 2012 The Royal Society of Chemistry.

1.5.2 NMOFs for Optical Imaging

Optical imaging, including fluorescent and phosphorescent probes, is a powerful tool for bench-top research and diagnosis. The attachment of optical probes provides a quick method of visually observing endocytosis and cytotoxicity of NMOFs via microscopy. Many types of optical probes are used, including boron-dipyrromethene (bodipy),[28] rhodamine dyes,[5] and ruthenium complexes.[80] Often these probes serve as an indicator that attached targeting moieties are enhancing cell uptake. For example, Figure 1.8, in Section 1.3.2 visually demonstrates the targeting ability of anisamide to H460 human lung cancer cells via the encorporation of a phosphorescent [Ru 5,5'-$(CO_2)_2$-bpy$(bpy)_2$] (bpy is 2,2'-bipyridine) component encorporated into the MOF backbone.[80] Additionally, probes can be used to image the biodistribution of nanoparticles. For example, Kimizuka and coworkers demonstrated accumulation of Gd^{3+}-based nanoparticles doped with a perylene-5 dye in the liver tissues of mice injected with the nanoparticles, Figure 1.12.[106] In addition to attaching optical dyes to the surface of MOFs, lanthanide ions (Tb^{3+} and Eu^{3+}) can also be doped into the materials post-synthetically via

encapsulation.[6, 46, 81, 107] These ions provide luminescent properties to the MOF material in much the same way as organic dyes.

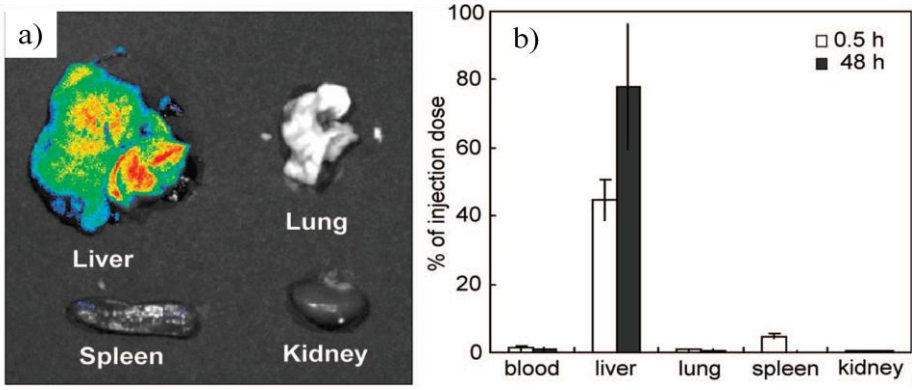

Figure 1.12 a) Fluorescent images of tissue samples (liver, spleen, kidney and lung) isolated from mice injected with Gd^{3+}-based nanoparticles doped with perylene-5 dye. b) ICP-MS analysis of gadolinium confirming NP accumulation in the liver from the mice, after 0.5 and 48 h of injection. This image was adapted with permission from reference 106. Copyright © 2009 American Chemical Society.

1.6 MOFs in Photodynamic Therapy

It should be noted that recently, MOFs have been proposed as nanoparticulate PDT agents. Traditional photodynamic therapy (PDT) involves the use of a photosensitizer that upon excitation with light forms an excited state, which reacts with surrounding constituents to produce reactive oxygen species including singlet state oxygen. Singlet-state oxygen reacts with cellular components in a number of ways, typically by inhibiting metabolic pathways, to result in cell death.[108] Advantages of PDT to other types of cancer therapies include lower mortality rates (because of the aggressive chemotherapy approaches that often overwhelm patients' immune systems), improved quality of life while undergoing therapy, and tumor elimination without invasive surgery.[108] Nanoparticles in particular are ideal candidates for PDT due to their ability to accumulate in tumor tissues via the enhanced permeation and retention (EPR) effect. As such, the

use of nanoparticles can eliminate the need for systemic distribution that results in increased photosensitivity to patients and damage to healthy tissues. Additionally, the use of nanoparticles enhances PDT efficiency by localizing multiple photosensitizers into a concentrated area resulting in a denser photosensitizer environment within tumor tissues. Due to the harmful nature of ultraviolet radiation (UV), and the wavelength associated with oxygen triplet to singlet excitation (1274 nm), the typical range of light desired to generate excited state oxygen is 800-1300 nm.

Nano-particulate MOFs for PDT have only recently been proposed by two reports from Wenbin Lin et al. The first material reported was a porphyrin-based MOF incorporating 5,15-di(p-benzoato)porphyrin (H_2DBP) and Hf metal centers to form a structure modeling the UiO-series of MOFs, UiO-DBP. While the administration of this nano-MOF resulted in rapid uptake by human head and neck cancer cells (SQ20B) and clearly demonstrated significant tumor reduction in tumor bearing mice subjects, the photophysical properties of the material were not ideal, with the most red-shifted absorbance found at 634 nm. The non-ideality of the photophysical properties lead to another report from this group where they employed an analogous chlorin-based MOF incorporating 5,15-di(p-methylbenzoato)chlorin (Me_2DBC), UiO-DBC.[31] The shift from a porphyrin linker to a chlorin resulted in a 13 nm increase in the lowest energy Q band and an extinction coefficient that was 11 times higher than the UiO-DBP, resulting in more optimal photophysical properties. The UiO-DBC nano-MOF also demonstrated cellular uptake and tumor reduction, further demonstrating the application of MOFs for photo-therapy.

1.7 Future Directions

In summary, there are multiple components that involve the development of theranostic DDSs. Ultimately; all of these components must be combined in order for MOFs to be competitive materials in nanomedicine. Due to the novelty of NMOFs for biological applications, research is currently aimed at exploring each component and how it can contribute to an overall successful theranostic MOF system. With time and more collaborative development however, MOFs for nanomedicine applications have tremendous potential. Although MOF DDSs that combine cooperative functionalities, (e.g. drug delivery, targeting and imaging capabilities) have been reported, the main issue of stability remains. Overall, in order for MOF DDSs to compete with marketed materials, they must demonstrate stability in biological conditions. Thus, the current challenges in the design of MOF theranostic medicines are aimed at, not only improving current technologies, but also discovering new materials to aid in the realization of MOFs in theranostic nanomedicine.

1.8 References

1. Strebhardt, K.; Ullrich, A., Paul Ehrlich's Magic Bullet Concept: 100 Years of Progress. *Nature Reviews Cancer* **2008,** *8* (6), 473-480.

2. Horcajada, P.; Serre, C.; Vallet-Regí, M.; Sebban, M.; Taulelle, F.; Férey, G., Metal–Organic Frameworks as Efficient Materials for Drug Delivery. *Angewandte Chemie International Edition* **2006,** *45* (36), 5974-5978.

3. Férey, G.; Mellot-Draznieks, C.; Serre, C.; Millange, F.; Dutour, J.; Surblé, S.; Margiolaki, I., A Chromium Terephthalate-Based Solid with Unusually Large Pore Volumes and Surface Area. *Science* **2005,** *309* (5743), 2040-2042.

4. Della Rocca, J.; Lin, W., Nanoscale Metal–Organic Frameworks: Magnetic Resonance Imaging Contrast Agents and Beyond. *European Journal of Inorganic Chemistry* **2010,** *2010* (24), 3725-3734.

5. Taylor, K. M. L.; Rieter, W. J.; Lin, W., Manganese-Based Nanoscale Metal−Organic Frameworks for Magnetic Resonance Imaging. *Journal of the American Chemical Society* **2008,** *130* (44), 14358-14359.

6. Rieter, W. J.; Taylor, K. M. L.; An, H.; Lin, W.; Lin, W., Nanoscale Metal−Organic Frameworks as Potential Multimodal Contrast Enhancing Agents. *Journal of the American Chemical Society* **2006,** *128* (28), 9024-9025.

7. Hoffman, A. S., The Origins and Evolution of "Controlled" Drug Delivery Systems. *Journal of Controlled Release* **2008,** *132* (3), 153-163.

8. Gabizon, A. A., Stealth Liposomes and Tumor Targeting: One Step Further in the Quest for the Magic Bullet. *Clinical Cancer Research* **2001,** *7* (2), 223-225.

9. Gregoriadis, G., Engineering Liposomes for Drug Delivery: Progress and Problems. *Trends in Biotechnology* **1995,** *13* (12), 527-537.

10. Mufamadi, M. S.; Pillay, V.; Choonara, Y. E.; Du Toit, L. C.; Modi, G.; Naidoo, D.; Ndesendo, V. M. K., A Review on Composite Liposomal Technologies for Specialized Drug Delivery. *Journal of Drug Delivery* **2011,** *2011*.

11. Kataoka, K.; Harada, A.; Nagasaki, Y., Block Copolymer Micelles for Drug Delivery: Design, Characterization and Biological Significance. *Advanced Drug Delivery Reviews* **2001,** *47* (1), 113-131.

12. Lasic, D. D., Mixed Micelles in Drug Delivery. *Nature* **1992,** *355* (6357), 279-280.

13. Kulak, A.; Hall, S. R.; Mann, S., Single-Step Fabrication of Drug-Encapsulated Inorganic Microspheres with Complex Form by Sonication-Induced Nanoparticle Assembly. *Chemical Communications* **2004,** (5), 576-577.

14. Liong, M.; Lu, J.; Kovochich, M.; Xia, T.; Ruehm, S. G.; Nel, A. E.; Tamanoi, F.; Zink, J. I., Multifunctional Inorganic Nanoparticles for Imaging, Targeting, and Drug Delivery. *ACS Nano* **2008,** *2* (5), 889-896.

15. Xu, Z. P.; Zeng, Q. H.; Lu, G. Q.; Yu, A. B., Inorganic Nanoparticles as Carriers for Efficient Cellular Delivery. *Chemical Engineering Science* **2006,** *61* (3), 1027-1040.

16. Duncan, R., The Dawning Era of Polymer Therapeutics. *Nature Reviews Drug Discovery* **2003,** *2* (5), 347.

17. Duncan, R.; Kopeček, J., Soluble Synthetic Polymers as Potential Drug Carriers Polymers in Medicine. Springer Berlin / Heidelberg: 1984; Vol. 57, pp 51-101.

18. Horcajada, P.; Gref, R.; Baati, T.; Allan, P. K.; Maurin, G.; Couvreur, P.; Férey, G.; Morris, R. E.; Serre, C., Metal–Organic Frameworks in Biomedicine. *Chemical Reviews* **2012,** *112* (2), 1232-1268.

19. Horcajada, P.; Chalati, T.; Serre, C.; Gillet, B.; Sebrie, C.; Baati, T.; Eubank, J. F.; Heurtaux, D.; Clayette, P.; Kreuz, C.; Chang, J.-S.; Hwang, Y. K.; Marsaud, V.; Bories, P.-N.; Cynober, L.; Gil, S.; Férey, G.; Couvreur, P.; Gref, R., Porous Metal–Organic-Framework Nanoscale Carriers as a Potential Platform for Drug Delivery and Imaging. *Nature Materials* **2010,** *9* (2), 172-178.

20. Huxford, R. C.; Della Rocca, J.; Lin, W., Metal–Organic Frameworks as Potential Drug Carriers. *Current Opinion in Chemical Biology* **2010,** *14* (2), 262-268.

21. McKinlay, A. C.; Morris, R. E.; Horcajada, P.; Férey, G.; Gref, R.; Couvreur, P.; Serre, C., Biomofs: Metal–Organic Frameworks for Biological and Medical Applications. *Angewandte Chemie International Edition* **2010,** *49* (36), 6260-6266.

22. Vallet-Regí, M.; Balas, F.; Arcos, D., Mesoporous Materials for Drug Delivery. *Angewandte Chemie International Edition* **2007,** *46* (40), 7548-7558.

23. Della Rocca, J.; Liu, D.; Lin, W., Nanoscale Metal–Organic Frameworks for Biomedical Imaging and Drug Delivery. *Accounts of Chemical Research* **2011,** *44* (10), 957-968.

24. He, C.; Liu, D.; Lin, W., Nanomedicine Applications of Hybrid Nanomaterials Built from Metal–Ligand Coordination Bonds: Nanoscale Metal–Organic Frameworks and Nanoscale Coordination Polymers. *Chemical Reviews* **2015,** *115* (19), 11079-11108.

25. Giménez-Marqués, M.; Hidalgo, T.; Serre, C.; Horcajada, P., Nanostructured Metal–Organic Frameworks and Their Bio-Related Applications. *Coordination Chemistry Reviews* **2016,** *307, Part 2*, 342-360.

26. Batten, S. R.; Champness, N. R.; Xiao-Ming, C.; Garcia-Martinez, J.; Kitagawa, S.; Öhrström, L.; O'Keeffe, M.; Myunghyun Paik, S.; Reedijk, J., Terminology of Metal--Organic Frameworks and Coordination Polymers (Iupac Recommendations 2013). *Pure & Applied Chemistry* **2013,** *85* (8), 1715-1724.

27. Tamames-Tabar, C.; Cunha, D.; Imbuluzqueta, E.; Ragon, F.; Serre, C.; Blanco-Prieto, M. J.; Horcajada, P., Cytotoxicity of Nanoscaled Metal-Organic Frameworks. *Journal of Materials Chemistry B* **2014,** *2* (3), 262-271.

28. Taylor-Pashow, K. M. L.; Rocca, J. D.; Xie, Z.; Tran, S.; Lin, W., Postsynthetic Modifications of Iron-Carboxylate Nanoscale Metal−Organic Frameworks for Imaging

and Drug Delivery. *Journal of the American Chemical Society* **2009,** *131* (40), 14261-14263.

29. He, C.; Lu, K.; Lin, W., Nanoscale Metal–Organic Frameworks for Real-Time Intracellular Ph Sensing in Live Cells. *Journal of the American Chemical Society* **2014,** *136* (35), 12253-12256.

30. Rieter, W. J.; Pott, K. M.; Taylor, K. M. L.; Lin, W., Nanoscale Coordination Polymers for Platinum-Based Anticancer Drug Delivery. *Journal of the American Chemical Society* **2008,** *130* (35), 11584-11585.

31. Lu, K.; He, C.; Lin, W., A Chlorin-Based Nanoscale Metal–Organic Framework for Photodynamic Therapy of Colon Cancers. *Journal of the American Chemical Society* **2015,** *137* (24), 7600-7603.

32. Miller, S. R.; Heurtaux, D.; Baati, T.; Horcajada, P.; Greneche, J.-M.; Serre, C., Biodegradable Therapeutic Mofs for the Delivery of Bioactive Molecules. *Chemical Communications* **2010,** *46* (25), 4526-4528.

33. An, J.; Geib, S. J.; Rosi, N. L., Cation-Triggered Drug Release from a Porous Zinc−Adeninate Metal−Organic Framework. *Journal of the American Chemical Society* **2009,** *131* (24), 8376-8377.

34. Horcajada, P.; Serre, C.; Maurin, G.; Ramsahye, N. A.; Balas, F.; Vallet-Regí, M.; Sebban, M.; Taulelle, F.; Férey, G., Flexible Porous Metal-Organic Frameworks for a Controlled Drug Delivery. *Journal of the American Chemical Society* **2008,** *130* (21), 6774-6780.

35. Gordon, J.; Kazemian, H.; Rohani, S., Mil-53(Fe), Mil-101, and Sba-15 Porous Materials: Potential Platforms for Drug Delivery. *Materials Science and Engineering: C* **2015,** *47*, 172-179.

36. Final Report on the Safety Assessment of Benzyl Alcohol, Benzoic Acid, and Sodium Benzoate. *International Journal of Toxicology* **2001,** *20* (3 suppl), 23-50.

37. He, J.; Yu, J.; Zhang, Y.; Pan, Q.; Xu, R., Synthesis, Structure, and Luminescent Property of a Heterometallic Metal−Organic Framework Constructed from Rod-Shaped Secondary Building Blocks. *Inorganic Chemistry* **2005,** *44* (25), 9279-9282.

38. McDonald, T. M.; Lee, W. R.; Mason, J. A.; Wiers, B. M.; Hong, C. S.; Long, J. R., Capture of Carbon Dioxide from Air and Flue Gas in the Alkylamine-Appended Metal–Organic Framework Mmen-Mg2(Dobpdc). *Journal of the American Chemical Society* **2012,** *134* (16), 7056-7065.

39. Senkovska, I.; Kaskel, S., Solvent-Induced Pore-Size Adjustment in the Metal-Organic Framework [Mg3(Ndc)3(Dmf)4] (Ndc = Naphthalenedicarboxylate). *European Journal of Inorganic Chemistry* **2006,** *2006* (22), 4564-4569.

40. Zhang, D.-J.; Song, T.-Y.; Shi, J.; Ma, K.-R.; Wang, Y.; Wang, L.; Zhang, P.; Fan, Y.; Xu, J.-N., Solvothermal Synthesis a Novel Hemidirected 2-D (3,3)-Net Metal-Organic Framework [Pb(Hidc)]N Based on the Linkages of Left- and Right-Hand Helical Chains. *Inorganic Chemistry Communications* **2008,** *11* (2), 192-195.

41. Klinowski, J.; Almeida Paz, F. A.; Silva, P.; Rocha, J., Microwave-Assisted Synthesis of Metal-Organic Frameworks. *Dalton Transactions* **2011,** *40* (2), 321-330.

42. Lu, C.-M.; Liu, J.; Xiao, K.; Harris, A. T., Microwave Enhanced Synthesis of Mof-5 and Its Co2 Capture Ability at Moderate Temperatures across Multiple Capture and Release Cycles. *Chemical Engineering Journal* **2010,** *156* (2), 465-470.

43. Seo, Y.-K.; Hundal, G.; Jang, I. T.; Hwang, Y. K.; Jun, C.-H.; Chang, J.-S., Microwave Synthesis of Hybrid Inorganic–Organic Materials Including Porous Cu3(Btc)2 from

Cu(Ii)-Trimesate Mixture. *Microporous and Mesoporous Materials* **2009,** *119* (1–3), 331-337.

44. Xiang, Z.; Cao, D.; Shao, X.; Wang, W.; Zhang, J.; Wu, W., Facile Preparation of High-Capacity Hydrogen Storage Metal-Organic Frameworks: A Combination of Microwave-Assisted Solvothermal Synthesis and Supercritical Activation. *Chemical Engineering Science* **2010,** *65* (10), 3140-3146.
45. Taylor, K. M. L.; Jin, A.; Lin, W., Surfactant-Assisted Synthesis of Nanoscale Gadolinium Metal–Organic Frameworks for Potential Multimodal Imaging. *Angewandte Chemie International Edition* **2008,** *47* (40), 7722-7725.
46. Xu, H.; Rao, X.; Gao, J.; Yu, J.; Wang, Z.; Dou, Z.; Cui, Y.; Yang, Y.; Chen, B.; Qian, G., A Luminescent Nanoscale Metal-Organic Framework with Controllable Morphologies for Spore Detection. *Chemical Communications* **2012**.
47. Schaate, A.; Roy, P.; Godt, A.; Lippke, J.; Waltz, F.; Wiebcke, M.; Behrens, P., Modulated Synthesis of Zr-Based Metal–Organic Frameworks: From Nano to Single Crystals. *Chemistry – A European Journal* **2011,** *17* (24), 6643-6651.
48. Tsuruoka, T.; Furukawa, S.; Takashima, Y.; Yoshida, K.; Isoda, S.; Kitagawa, S., Nanoporous Nanorods Fabricated by Coordination Modulation and Oriented Attachment Growth. *Angewandte Chemie International Edition* **2009,** *48* (26), 4739-4743.
49. Ragon, F.; Chevreau, H.; Devic, T.; Serre, C.; Horcajada, P., Impact of the Nature of the Organic Spacer on the Crystallization Kinetics of Uio-66(Zr)-Type Mofs. *Chemistry – A European Journal* **2015,** *21* (19), 7135-7143.
50. Della Rocca, J.; Liu, D.; Lin, W., Nanoscale Metal–Organic Frameworks for Biomedical Imaging and Drug Delivery. *Accounts of Chemical Research* **2011,** *44* (10), 957-968.

51. Cunha, D.; Ben Yahia, M.; Hall, S.; Miller, S. R.; Chevreau, H.; Elkaïm, E.; Maurin, G.; Horcajada, P.; Serre, C., Rationale of Drug Encapsulation and Release from Biocompatible Porous Metal–Organic Frameworks. *Chemistry of Materials* **2013,** *25* (14), 2767-2776.

52. Baati, T.; Horcajada, P.; Gref, R.; Couvreur, P.; Serre, C., Quantification of Fumaric Acid in Liver, Spleen and Urine by High-Performance Liquid Chromatography Coupled to Photodiode-Array Detection. *Journal of Pharmaceutical and Biomedical Analysis* **2011,** *56* (4), 758-762.

53. Devautour-Vinot, S.; Martineau, C.; Diaby, S.; Ben-Yahia, M.; Miller, S.; Serre, C.; Horcajada, P.; Cunha, D.; Taulelle, F.; Maurin, G., Caffeine Confinement into a Series of Functionalized Porous Zirconium Mofs: A Joint Experimental/Modeling Exploration. *The Journal of Physical Chemistry C* **2013,** *117* (22), 11694-11704.

54. Liédana, N.; Galve, A.; Rubio, C.; Téllez, C.; Coronas, J., Caf@Zif-8: One-Step Encapsulation of Caffeine in Mof. *ACS Applied Materials & Interfaces* **2012,** *4* (9), 5016-5021.

55. Devautour-Vinot, S.; Diaby, S.; da Cunha, D.; Serre, C.; Horcajada, P.; Maurin, G., Ligand Dynamics of Drug-Loaded Microporous Zirconium Terephthalates-Based Metal–Organic Frameworks: Impact of the Nature and Concentration of the Guest. *The Journal of Physical Chemistry C* **2014,** *118* (4), 1983-1989.

56. Mocniak, K. A.; Kubajewska, I.; Spillane, D. E. M.; Williams, G. R.; Morris, R. E., Incorporation of Cisplatin into the Metal-Organic Frameworks UiO66-NH2 and UiO66 - Encapsulation Vs. Conjugation. *RSC Advances* **2015,** *5* (102), 83648-83656.

57. Kapoor, S.; Hegde, R.; Bhattacharyya, A. J., Influence of Surface Chemistry of Mesoporous Alumina with Wide Pore Distribution on Controlled Drug Release. *Journal of Controlled Release* **2009,** *140* (1), 34-39.

58. Shen, S.-C.; Ng, W. K.; Chia, L.; Hu, J.; Tan, R. B. H., Physical State and Dissolution of Ibuprofen Formulated by Co-Spray Drying with Mesoporous Silica: Effect of Pore and Particle Size. *International Journal of Pharmaceutics* **2011,** *410* (1–2), 188-195.

59. Zhang, Y.; Chen, J.; Zhang, G.; Lu, J.; Yan, H.; Liu, K., Sustained Release of Ibuprofen from Polymeric Micelles with a High Loading Capacity of Ibuprofen in Media Simulating Gastrointestinal Tract Fluids. *Reactive and Functional Polymers* **2012,** *72* (6), 359-364.

60. Vasconcelos, I. B.; Silva, T. G. d.; Militao, G. C. G.; Soares, T. A.; Rodrigues, N. M.; Rodrigues, M. O.; Costa, N. B. d.; Freire, R. O.; Junior, S. A., Cytotoxicity and Slow Release of the Anti-Cancer Drug Doxorubicin from Zif-8. *RSC Advances* **2012,** *2* (25), 9437-9442.

61. Orellana-Tavra, C.; Baxter, E. F.; Tian, T.; Bennett, T. D.; Slater, N. K. H.; Cheetham, A. K.; Fairen-Jimenez, D., Amorphous Metal-Organic Frameworks for Drug Delivery. *Chemical Communications* **2015,** *51* (73), 13878-13881.

62. di Nunzio, M. R.; Agostoni, V.; Cohen, B.; Gref, R.; Douhal, A., A "Ship in a Bottle" Strategy to Load a Hydrophilic Anticancer Drug in Porous Metal Organic Framework Nanoparticles: Efficient Encapsulation, Matrix Stabilization, and Photodelivery. *Journal of Medicinal Chemistry* **2014,** *57* (2), 411-420.

63. He, C.; Lu, K.; Liu, D.; Lin, W., Nanoscale Metal–Organic Frameworks for the Co-Delivery of Cisplatin and Pooled Sirnas to Enhance Therapeutic Efficacy in Drug-Resistant

Ovarian Cancer Cells. *Journal of the American Chemical Society* **2014,** *136* (14), 5181-5184.

64. Zheng, H.; Zhang, Y.; Liu, L.; Wan, W.; Guo, P.; Nyström, A. M.; Zou, X., One-Pot Synthesis of Metal–Organic Frameworks with Encapsulated Target Molecules and Their Applications for Controlled Drug Delivery. *Journal of the American Chemical Society* **2016,** *138* (3), 962-968.
65. Babarao, R.; Jiang, J., Unraveling the Energetics and Dynamics of Ibuprofen in Mesoporous Metal−Organic Frameworks. *The Journal of Physical Chemistry C* **2009,** *113* (42), 18287-18291.
66. Hamon, L.; Heymans, N.; Llewellyn, P. L.; Guillerm, V.; Ghoufi, A.; Vaesen, S.; Maurin, G.; Serre, C.; De Weireld, G.; Pirngruber, G. D., Separation of Co2-Ch4 Mixtures in the Mesoporous Mil-100(Cr) Mof: Experimental and Modelling Approaches. *Dalton Transactions* **2012,** *41* (14), 4052-4059.
67. Lan, Y.-Q.; Jiang, H.-L.; Li, S.-L.; Xu, Q., Mesoporous Metal-Organic Frameworks with Size-Tunable Cages: Selective Co2 Uptake, Encapsulation of Ln3+ Cations for Luminescence, and Column-Chromatographic Dye Separation. *Advanced Materials* **2011,** *23* (43), 5015-5020.
68. Gaudin, C.; Cunha, D.; Ivanoff, E.; Horcajada, P.; Chevé, G.; Yasri, A.; Loget, O.; Serre, C.; Maurin, G., A Quantitative Structure Activity Relationship Approach to Probe the Influence of the Functionalization on the Drug Encapsulation of Porous Metal-Organic Frameworks. *Microporous and Mesoporous Materials* **2012,** *157* (0), 124-130.

69. Tan, L.-L.; Li, H.; Qiu, Y.-C.; Chen, D.-X.; Wang, X.; Pan, R.-Y.; Wang, Y.; Zhang, S. X.-A.; Wang, B.; Yang, Y.-W., Stimuli-Responsive Metal-Organic Frameworks Gated by Pillar[5]Arene Supramolecular Switches. *Chemical Science* **2015,** *6* (3), 1640-1644.

70. Tan, L.-L.; Li, H.; Zhou, Y.; Zhang, Y.; Feng, X.; Wang, B.; Yang, Y.-W., Zn2+-Triggered Drug Release from Biocompatible Zirconium Mofs Equipped with Supramolecular Gates. *Small* **2015,** *11* (31), 3807-3813.

71. Tan, L.-L.; Song, N.; Zhang, S. X.-A.; Li, H.; Wang, B.; Yang, Y.-W., Ca2+, Ph and Thermo Triple-Responsive Mechanized Zr-Based Mofs for on-Command Drug Release in Bone Diseases. *Journal of Materials Chemistry B* **2016,** *4* (1), 135-140.

72. Hu, Q.; Yu, J.; Liu, M.; Liu, A.; Dou, Z.; Yang, Y., A Low Cytotoxic Cationic Metal–Organic Framework Carrier for Controllable Drug Release. *Journal of Medicinal Chemistry* **2014,** *57* (13), 5679-5685.

73. Nagata, S.; Kokado, K.; Sada, K., Metal-Organic Framework Tethering Pnipam for on-Off Controlled Release in Solution. *Chemical Communications* **2015,** *51* (41), 8614-8617.

74. Sun, C.-Y.; Qin, C.; Wang, X.-L.; Yang, G.-S.; Shao, K.-Z.; Lan, Y.-Q.; Su, Z.-M.; Huang, P.; Wang, C.-G.; Wang, E.-B., Zeolitic Imidazolate Framework-8 as Efficient Ph-Sensitive Drug Delivery Vehicle. *Dalton Transactions* **2012,** *41* (23), 6906-6909.

75. Tanabe, K. K.; Cohen, S. M., Postsynthetic Modification of Metal-Organic Frameworks-a Progress Report. *Chemical Society Reviews* **2011,** *40* (2), 498-519.

76. Song, Y.-F.; Cronin, L., Postsynthetic Covalent Modification of Metal–Organic Framework (Mof) Materials. *Angewandte Chemie International Edition* **2008,** *47* (25), 4635-4637.

77. deKrafft, K. E.; Boyle, W. S.; Burk, L. M.; Zhou, O. Z.; Lin, W., Zr- and Hf-Based Nanoscale Metal-Organic Frameworks as Contrast Agents for Computed Tomography. *Journal of Materials Chemistry* **2012,** *22* (35), 18139-18144.

78. Gref, R.; Minamitake, Y.; Peracchia, M. T.; Trubetskoy, V.; Torchilin, V.; Langer, R., Biodegradable Long-Circulating Polymeric Nanospheres. *Science* **1994,** *263* (5153), 1600-1603.

79. Liu, D.; Huxford, R. C.; Lin, W., Phosphorescent Nanoscale Coordination Polymers as Contrast Agents for Optical Imaging. *Angewandte Chemie International Edition* **2011,** *50* (16), 3696-3700.

80. Rieter, W. J.; Taylor, K. M. L.; Lin, W., Surface Modification and Functionalization of Nanoscale Metal-Organic Frameworks for Controlled Release and Luminescence Sensing. *Journal of the American Chemical Society* **2007,** *129* (32), 9852-9853.

81. Rieter, W. J.; Kim, J. S.; Taylor, K. M. L.; An, H.; Lin, W.; Tarrant, T.; Lin, W., Hybrid Silica Nanoparticles for Multimodal Imaging. *Angewandte Chemie International Edition* **2007,** *46* (20), 3680-3682.

82. Graf, C.; Vossen, D. L. J.; Imhof, A.; van Blaaderen, A., A General Method to Coat Colloidal Particles with Silica. *Langmuir* **2003,** *19* (17), 6693-6700.

83. Rowe, M. D.; Thamm, D. H.; Kraft, S. L.; Boyes, S. G., Polymer-Modified Gadolinium Metal-Organic Framework Nanoparticles Used as Multifunctional Nanomedicines for the Targeted Imaging and Treatment of Cancer. *Biomacromolecules* **2009,** *10* (4), 983-993.

84. Wang, S.; Morris, W.; Liu, Y.; McGuirk, C. M.; Zhou, Y.; Hupp, J. T.; Farha, O. K.; Mirkin, C. A., Surface-Specific Functionalization of Nanoscale Metal–Organic Frameworks. *Angewandte Chemie International Edition* **2015,** *54* (49), 14738-14742.

85. Maeda, H., The Enhanced Permeability and Retention (Epr) Effect in Tumor Vasculature: The Key Role of Tumor-Selective Macromolecular Drug Targeting. *Advances in Enzyme Regulation* **2001,** *41* (1), 189-207.

86. Fang, J.; Nakamura, H.; Maeda, H., The Epr Effect: Unique Features of Tumor Blood Vessels for Drug Delivery, Factors Involved, and Limitations and Augmentation of the Effect. *Advanced Drug Delivery Reviews* **2011,** *63* (3), 136-151.

87. Maeda, H.; Wu, J.; Sawa, T.; Matsumura, Y.; Hori, K., Tumor Vascular Permeability and the Epr Effect in Macromolecular Therapeutics: A Review. *Journal of Controlled Release* **2000,** *65* (1–2), 271-284.

88. Lee, J. W.; Juliano, R. L., A5β1 Integrin Protects Intestinal Epithelial Cells from Apoptosis through a Phosphatidylinositol 3-Kinase and Protein Kinase B–Dependent Pathway. *Molecular Biology of the Cell* **2000,** *11* (6), 1973-1987.

89. Val M. Runge; Ai, T. D., Hao; Xuemei Hu, The Developmental History of the Gadolinium Chelates as Intravenous Contrast Media for Magnetic Resonance. *Investigative Radiology* **2011,** *46* (12), 807-816.

90. Bryson, J. M.; Reineke, J. W.; Reineke, T. M., Macromolecular Imaging Agents Containing Lanthanides: Can Conceptual Promise Lead to Clinical Potential? *Macromolecules* **2012,** *45* (22), 8939-8952.

91. Hermann, P.; Kotek, J.; Kubicek, V.; Lukes, I., Gadolinium(Iii) Complexes as Mri Contrast Agents: Ligand Design and Properties of the Complexes. *Dalton Transactions* **2008,** (23), 3027-3047.

92. Port, M.; Idee, J.-M.; Medina, C.; Robic, C.; Sabatou, M.; Corot, C., Efficiency, Thermodynamic and Kinetic Stability of Marketed Gadolinium Chelates and Their Possible Clinical Consequences: A Critical Review. *BioMetals* **2008,** *21* (4), 469-490.

93. Hu, F.; Zhao, Y. S., Inorganic Nanoparticle-Based T1 and T1/T2 Magnetic Resonance Contrast Probes. *Nanoscale* **2012,** *4* (20), 6235-6243.

94. Kinsella, J. M.; Ananda, S.; Andrew, J. S.; Grondek, J. F.; Chien, M.-P.; Scadeng, M.; Gianneschi, N. C.; Ruoslahti, E.; Sailor, M. J., Enhanced Magnetic Resonance Contrast of Fe3o4 Nanoparticles Trapped in a Porous Silicon Nanoparticle Host. *Advanced Materials* **2011,** *23* (36), H248-H253.

95. Na, H. B.; Song, I. C.; Hyeon, T., Inorganic Nanoparticles for Mri Contrast Agents. *Advanced Materials* **2009,** *21* (21), 2133-2148.

96. Adkins, C. T.; Dobish, J. N.; Brown, C. S.; Mayrsohn, B.; Hamilton, S. K.; Udoji, F.; Radford, K.; Yankeelov, T. E.; Gore, J. C.; Harth, E., High Relaxivity Mri Imaging Reagents from Bimodal Star Polymers. *Polymer Chemistry* **2012,** *3* (2), 390-398.

97. Boase, N. R. B.; Blakey, I.; Thurecht, K. J., Molecular Imaging with Polymers. *Polymer Chemistry* **2012,** *3* (6), 1384-1389.

98. Li, Y.; Beija, M.; Laurent, S.; Elst, L. v.; Muller, R. N.; Duong, H. T. T.; Lowe, A. B.; Davis, T. P.; Boyer, C., Macromolecular Ligands for Gadolinium Mri Contrast Agents. *Macromolecules* **2012,** *45* (10), 4196-4204.

99. Wang, K.; Peng, H.; Thurecht, K. J.; Puttick, S.; Whittaker, A. K., Ph-Responsive Star Polymer Nanoparticles: Potential 19f Mri Contrast Agents for Tumour-Selective Imaging. *Polymer Chemistry* **2013,** *4* (16), 4480-4489.

100. Rowe, M. D.; Chang, C.-C.; Thamm, D. H.; Kraft, S. L.; Harmon, J. F.; Vogt, A. P.; Sumerlin, B. S.; Boyes, S. G., Tuning the Magnetic Resonance Imaging Properties of Positive Contrast Agent Nanoparticles by Surface Modification with Raft Polymers. *Langmuir* **2009,** *25* (16), 9487-9499.

101. Liu, D.; Lu, K.; Poon, C.; Lin, W., Metal–Organic Frameworks as Sensory Materials and Imaging Agents. *Inorganic Chemistry* **2014,** *53* (4), 1916-1924.

102. Terreno, E.; Castelli, D. D.; Viale, A.; Aime, S., Challenges for Molecular Magnetic Resonance Imaging. *Chemical Reviews* **2010,** *110* (5), 3019-3042.

103. Lusic, H.; Grinstaff, M. W., X-Ray-Computed Tomography Contrast Agents. *Chemical Reviews* **2013,** *113* (3), 1641-1666.

104. deKrafft, K. E.; Xie, Z.; Cao, G.; Tran, S.; Ma, L.; Zhou, O. Z.; Lin, W., Iodinated Nanoscale Coordination Polymers as Potential Contrast Agents for Computed Tomography. *Angewandte Chemie International Edition* **2009,** *48* (52), 9901-9904.

105. Nishiyabu, R.; Hashimoto, N.; Cho, T.; Watanabe, K.; Yasunaga, T.; Endo, A.; Kaneko, K.; Niidome, T.; Murata, M.; Adachi, C.; Katayama, Y.; Hashizume, M.; Kimizuka, N., Nanoparticles of Adaptive Supramolecular Networks Self-Assembled from Nucleotides and Lanthanide Ions. *Journal of the American Chemical Society* **2009,** *131* (6), 2151-2158.

106. Wang, Y.; Yang, J.; Liu, Y.-Y.; Ma, J.-F., Controllable Syntheses of Porous Metal–Organic Frameworks: Encapsulation of Lniii Cations for Tunable Luminescence and Small Drug Molecules for Efficient Delivery. *Chemistry – A European Journal* **2013,** *19* (43), 14591-14599.

107. Lucky, S. S.; Soo, K. C.; Zhang, Y., Nanoparticles in Photodynamic Therapy. *Chemical Reviews* **2015,** *115* (4), 1990-2042.

2. Cargo Delivery on Demand from Photodegradable MOF Nano-Cages

This chapter has been adapted from a published manuscript by C.C. Epley, K. L. Roth, S. Lin S.R. Ahrenholtz, T. Z. Grove, and A.J. Morris from the following reference: *Dalton Trans.*, **2017**, 46, 4917-4922.

2.1 Abstract

We report the photo-induced degradation of and cargo release from a nanoscale metal-organic framework (nMOF) incorporating photo-isomerizable 4,4´-azobenzenedicarboxylate (AZB) linkers. The structure matches a UiO-type framework where 12 4,4´-azobenzenedicarboxylate moieties are connected to a $Zr_6O_4(OH)_4$ cluster, referred to as UiO-AZB. Due to the incorporation of photo-isomerizable struts, the degradation of UiO-AZB is accelerated by irradiation with white light (1.3 ± 0.1 %/h under dark conditions vs. 8.4 ± 0.4 %/h when irradiated). Additionally, we show slow release of Nile Red (NR) which is triggered by irradiation (0.04 ± 0.01 %/h under dark conditions vs. 0.36 ± 0.02 %/h when irradiated).

2.2 Introduction

The term "caging", first devised in 1978,[1] has been used to describe chemical designs containing an active component, liberated "on demand" when a stimulus is applied. Challenges when developing these systems lie in the ability to secure active cargos until they are needed and controllably release them when prompted. Several triggers are available for controlled release such as thermal changes,[2-3] pH adjustments,[4] and photo irradiation[5-6] among others. However, light as a primary stimulus is the most useful for a variety of practical materials because; i) it can function autonomously from

the chemical system to which it is being applied, ii) it offers tunability in terms of available wavelength, intensity, and time of exposure to control desired processes, and iii) it is relatively cheap (free in some cases) and easy to use.

Applications, from long-lived fragrances[7-9] and gas release,[10-11] to fertilizers[12-15] and drug delivery[16-17] are among the utilities for these photo-caged systems. This class of materials consists of molecular designs that release their cargo via covalent bond cleavage,[5] metal complexes with photo-labile ligands,[16] or larger structural assemblies (i.e. nanoparticles) serving to encapsulate and/or anchor payloads.[18-21] Of these photo-caging approaches, studies involving *photo-active nanoparticles* have become a major research interest,[22] especially for biological applications, due to the tumor targeting capability of nanoparticles via the enhanced permeation and retention (EPR) effect. This field has grown vastly in recent decades to include polymers,[23-25] liposomes,[26-27] micelles,[28-31] and vesicles[32-33] among others.[34-36]

Photo-initiated release from nanocarrier cages can be achieved in a number of ways.[37] For example, in a report from Murphy and coworkers,[38] gold nanorods were coated with poly(acrylic acid sodium salt) and poly(allylamine hydrochloride) layers. Rhodamine 6G (R6G) was embedded within the surface polyelectrolyte layers and photothermal release of the R6G (~6 % after 60 min) was demonstrated upon irradiation of the material. The release of the dye was attributed to the absorption of light by the surface plasmon resonance bands and subsequent non-radiative decay from the nanorods to generate localized heat. This heat served to disrupt the polyelectrolyte layers and release the R6G cargo. In another example,[39] micelles made of a photo-responsive poly(S-(*o*-nitrobenzyl)-L-cysteine)-*b*-poly(ethylene glycol) copolymer (PNBC-*b*-PEO) arranged in β-sheets were

shown to "contract" upon irradiation at 365 nm. This contraction, resulting from the cleavage of the NB groups from the core polymer backbone and subsequent reassembly to smaller micelles, resulted in the release of doxorubicin (maximum of ~40 % released over 110 h) encapsulated in the PNBC core polymer matrix.

Yet another cargo release approach is via photo-degradation. This mechanism relies on the *irreversible* instability of the nanocarrier under irradiation with light that produces significant decreases in structural integrity of the material and serves to release the active component. While there are several reports of this design in polymeric and micellular systems,[33] in general, material degradation is not advantageous in biological systems due to the "burst release" phenomenon that plagues polymeric nanoparticles. While inorganic nanoparticles are inherently more robust, they typically do not degrade upon photo-irradiation. Additionally, biodistribution and biodegradability of inorganic nanoparticles is a concern, as they tend to accumulate in soft tissues and are not easily metabolized. Hybrid metal-organic frameworks (MOFs), on the other hand, have tremendous potential in this regard. MOFs, originally aimed at gas storage and separation,[40-41] have since shown promise in areas ranging from heterogeneous catalysis[42-43] to MRI imaging[44-45] and drug delivery.[46-47] With exceptionally high surface areas (up to 7000 m^2/g), these materials have the potential to hoard abundant payloads. Additionally, the synthetic tunability of MOF systems and the hydrolytic nature of metal-linker bonds (better biodegradability), offer a handle by which to develop photo-degradable nanocarriers.[48]

MOFs have been explored as potential nanocarriers[45, 47] and in a few reports, stimuli-responsive (not photo-induced) drug delivery.[49-52] In the context of photo-responsive materials, there is a report of photo-controlled drug delivery from Abderrazzak Douhal et

al. where they demonstrated photo-enhanced release of topotecan (an approved drug for several cancer types) with ~4 vs. ~28 wt% released in the dark and via irradiation with 780 nm light, respectively.[52] Additionally, Wenbin Lin and co-workers[53-54] have developed MOFs incorporating a chlorin-based photosensitizer and indoleamine 2,3-dioxygenase for dual mode photodynamic therapy (PDT) and immunotherapy respectively. More recently, Cheng Wang et al.[55] have demonstrated rhodamine 6G (R6G) release from MOFs equipped with pendant azobenzenes capped with β-cyclodextrin units. Upon irradiation, the azobenzene units isomerize and disrupt the surface capping moieties, thus releasing the R6G cargo. Additionally, it should be noted that photo-responsive MOFs have been reported for other applications as well. For example, in a report from De Vos et al.,[56] MIL-88B (MIL = Materials of Institute Lavoisier) MOFs encapsulated in a photo-cleavable polyurea shell were released upon irradiation with UV-light which was the result of degradation of the capsule. This MOF is a catalyst for the oxidation of tetramethylbenzidine (TMB) with H_2O_2 and indeed the rate of this reaction was significantly enhanced when the capsules were irradiated (~0.4 M/h vs. 0.025 M/h in the dark over a 25 h time frame), due to the degradation of the capsule and subsequent release of the catalytic MOF. Another interesting photochemical tool for MOF development is the ability to incorporate photo-liable protecting groups into MOF backbone linkers. These groups can then be cleaved post-synthetically to deprotect active groups and enhance the functionality of the MOF system. This approach has been demonstrated by Seth Cohen and Corrine Allen[57] where they constructed MOFs with nitrobenzyl protecting groups attached to a terephthalate-like linker component. Upon irradiation, the nitrobenzyl groups were cleaved to leave a phenolic group otherwise not

achievable via direct synthesis. These reports and others clearly demonstrate the scope of applications for photo-responsive MOF nanoparticles.

In this report, we have designed photo-degradable MOFs incorporating photo-isomerizable azobenzenedicarboxylate (AZB) linkers (Scheme 2.1). Isomerization of the organic struts upon irradiation with white light results in the breakdown of the MOF and subsequent release of a cargo. To our knowledge, the results presented herein are the first example of cargo release from MOFs occurring as a result of linker photo-isomerization and MOF degradation. We have chosen a UiO-type MOF UiO-AZB $[Zr_6O_4(OH)_4(C_{14}H_8N_2O_4)_6]$ to study our initial hypothesis and demonstrate photo-controlled cargo release. This MOF has been reported in the literature[58-59] however, this is the first report of particle size control. Synthetic optimization of the reported procedure[58] revealed increasing particle sizes with an increase in the acetic acid modulator, as evidenced via scanning electron microscopy (SEM, Figure 2.1). In contrast, no size dependence was previously reported with benzoic acid. We also found that at higher concentrations of modulator, the particle sizes became less uniform as indicated by larger standard deviations (Figure 2.1, F).

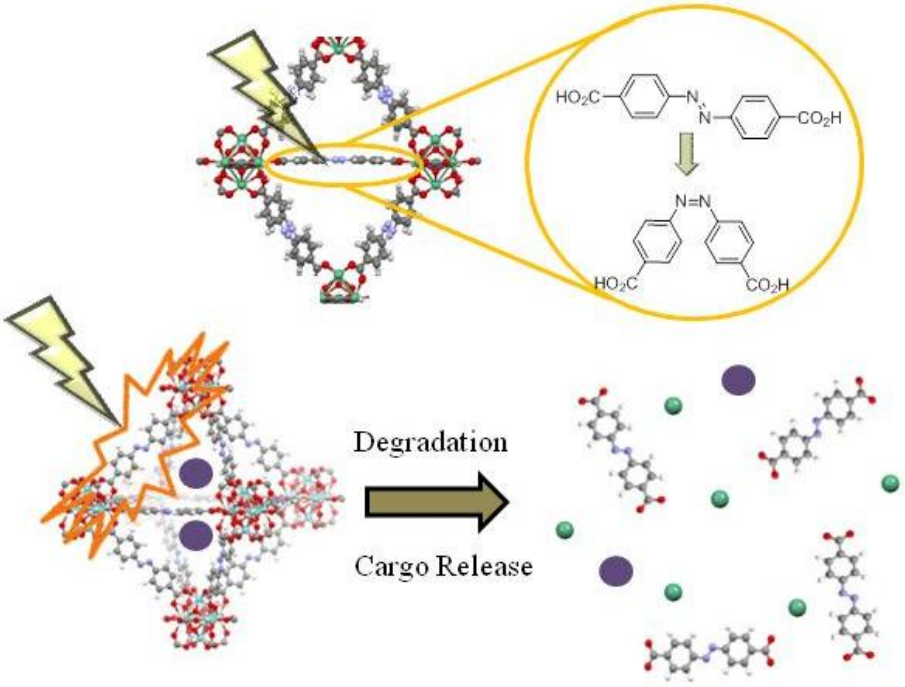

Scheme 2.1 Schematic representation of the photo-degradation of UiO-AZB MOFs (crystal structure: Zr, green; O, red; C, gray; N, blue; H, white) upon isomerization of the AZB linker from the trans-form to the cis-form and subsequent cargo (purple spheres) release from the degraded material.

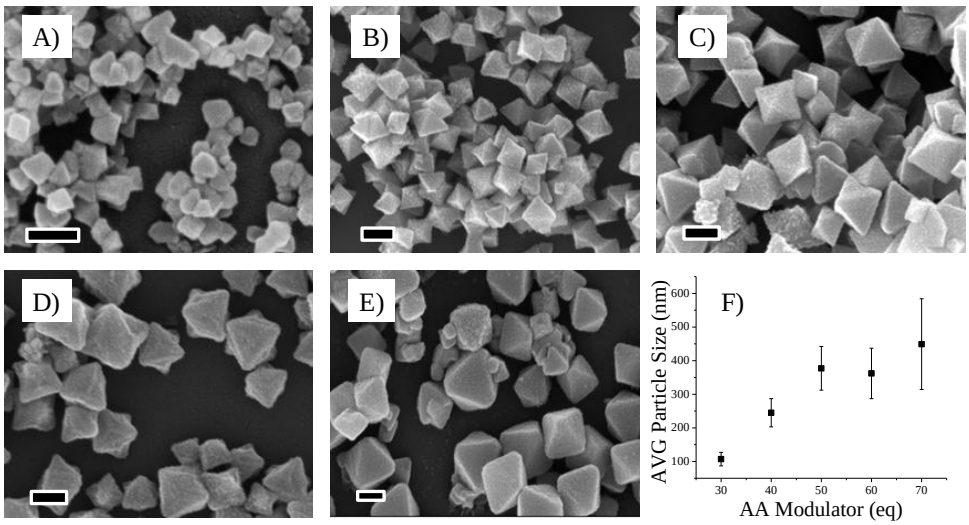

Figure 2.1 SEM images of particles made with A) 30, B) 40, C) 50, D) 60, and E) 70 molar equivalents of acetic acid. F) Particles size vs. the concentration of modulator. Scale bars are 200 nm.

2.3 Experimental

2.3.1 Materials

The 4-nitrobenzoic acid (98 %), sodium hydroxide (≥ 98%), D-glucose (≥ 98 %), $ZrCl_4$ (anhydrous, 99.99 %), $MgCl_2$ (anhydrous, 99 %) and Nile red (technical grade) were purchased from Sigma Aldrich and used without further purification. Glacial acetic acid (certified ACS), NaCl (99 %), KCl (99 %), $CaCl_2$ (93 %), HEPES sodium salt (99 %), dimethylsulfoxide (DMSO) and dimethylformamide (DMF, Spectrophotometric grade ≥ 99.8 %) were used as received from Fisher Scientific. Phosphate buffered saline (PBS), Dulbecco's Modified Eagle Medium (DMEM), and (3-(4,5-Dimethylthiazol-2-yl)-2,5,Diphenyltetrazolium bromide (MTT) were used as received from Thermo Fisher Scientific.

2.3.2 Synthesis of 4,4´-azobenzenedicarboxylic acid (AZB)[60]

4-nitrobenzoic acid (13 g) and 250 mL of 5 M NaOH were heated to 50 °C in a 500 mL round bottom flask. An aqueous solution of 3.7 M D-glucose (150 mL) was added slowly (30 mL/min) to the flask with vigorous stirring. The reaction was allowed to stir for 10 minutes and then cooled to room temperature. The solution was aerated for 12 h and 5 M (200 mL) aqueous acetic acid was added to precipitate the AZB. The pink solid was collected via vacuum filtration and dried in a 100 °C oven for 18 h. (9.6 g, ~91 %) ^{1}HNMR (500 MHz, basic D_2O, δ, ppm) trans: 7.94, 7.92 (d, 2H, J= 10 Hz), 7.82, 7.80 (d, 2H, J = 10 Hz), cis: 7.68, 7.66 (d, 2H, J=10 Hz), 6.91, 6.89 (d, 2H, J = 10 Hz), (Predicted m/z= 270.2; M-H^-= 269 m/z).

2.3.3 Synthesis of UiO-AZB nanoparticles

The synthesis described here was adapted from a previous report by changing the identity and concentration of the modulator.[58] In order to control particle sizes, the acetic acid (AA)

modulator was varied from 30-70 molar equivalents to Zr^{4+} (30 mol AA: 1 mol Zr^{4+}, Figure S2.I). For example, a 30 equivalent synthesis follows: to a 20 mL vial, $ZrCl_4$ (0.0234 g, 0.1 mmol), glacial acetic acid (172 μL, 3 mmol), water (10 μL), and DMF (5 mL) were added and the mixture sonicated for 5-10 min. H_2AZB (0.0270 g, 0.1 mmol) was then added and the solution sonicated for ~5 min to give an orange suspension. The mixture was placed in a 100 °C oven for 24 h. While still warm, the contents of the vial were transferred to a 15 mL centrifuge tube and the particles collected via centrifugation (4,000 rpm for ~15 min). After decanting the supernatant, 5 mL fresh DMF was added and the particles redispersed with sonication for 10 minutes. Particles were allowed to soak in the fresh DMF for 0.5-1 h. Particles were again collected via centrifugation and the supernatant decanted. This washing process was repeated for a total of 1 x 5 mL DMF and 5 x 5 mL EtOH. Upon removal of the final supernatant, the particles were dried in a vacuum oven at 50 °C for 24 h.

2.3.4 Simulated Cerebrospinal Fluid (SCF)

Simulated cerebrospinal fluid (SCF) was made following a Cold Spring Harbor Laboratory Press protocol.[61] The solution consists of 135 mM sodium chloride (NaCl), 5.4 mM potassium chloride (KCl), 5 mM4-(2-Hydroxyethyl)piperazine-1-ethanesulfonic acid sodium salt (Na-HEPES buffer), 1.8 mM calcium chloride ($CaCl_2$), and 1 mM magnesium chloride ($MgCl_2$). The pH of the solution was adjusted to 7.3 by adding concentrated (~12 M) hydrochloric acid.

2.3.5 Degradation Studies

The degradation of the UiO-AZB was monitored by submersing 0.5 mg into 3 mL of a 1:1 (v/v) solution of ethanol and SCF in a 24/40 jointed quartz cuvette. The cuvette was capped with a rubber septum and either wrapped in tin foil (dark conditions) or placed in front of the

light source (irradiated conditions). The absorbance at 392 nm (isosbestic point) of the supernatant solution was measured as a function of time. Experiments were replicated 3 times.

2.3.6 Ibuprofen (IBU) loading

50 mg UiO-AZB was suspended into a solution of 150 mg IBU in 30 mL hexane following an impregnation method previously reported.[62] The solution was allowed to stir for 5 h and the nanoparticles were collected via centrifugation of 15 mL aliquots. After decanting the final supernatant, 15 mL hexane was added and the nanoparticles were re-suspended via brief (< 1 min) sonication. Nanoparticles were then centrifuged again for ~5 min and the supernatant decanted. IBU loaded particles were then dried in a vacuum oven for 24 h at 50 °C.

2.3.7 Caffeine loading

50 mg UiO-AZB was suspended into a solution of 150 mg caffeine in 30 mL ethanol following an impregnation method previously reported.[62] The solution was allowed to stir for 24 h and the nanoparticles were collected via centrifugation of 15 mL aliquots. After decanting the final supernatant, 5 mL ethanol was added and the nanoparticles were re-suspended via brief (< 1 min) sonication. Nanoparticles were then centrifuged again for ~5 min and the supernatant decanted. IBU loaded UiO-AZB particles were then dried in a vacuum oven for 24 h at 50 °C.

2.3.8 Nile Red (NR) loading

50 mg UiO-AZB was suspended into 15 mL 48 μM NR in ethanol. Beyond this concentration the structural integrity of the nanoparticles was compromised as evidenced by PXRD (Figure S2.6). The solution was allowed to stir for 24 h and the nanoparticles were collected via centrifugation. After decanting the supernatant, 5 mL ethanol was added and the nanoparticles were re-suspended via brief (< 1 min) sonication. Nanoparticles were then

centrifuged again for ~5 min and the supernatant decanted. NR loaded UiO-AZB particles were then dried in a vacuum oven for 24 h at 50 °C.

2.3.9 Ibuprofen release

The release of IBU from the IBU loaded UiO-AZB nanoparticles was measured using HPLC. 2.7 mg of the IBU loaded UiO-AZB nanoparticles were submersed into 5 mL 1:1 (v/v) ethanol/SCF in a 24/40 jointed quartz cuvette. The cuvettes were capped with a rubber septum and kept either wrapped in tin foil (dark conditions) or placed in front of a 1000 W white light source (irradiated conditions). 100 μL aliquots were removed over time from the cuvettes and placed into a glass LC/MS vial. Aliquots were diluted with 900 μL ethanol/SCF (1:1 v/v) and analyzed using HPLC as described *vide supra*. The 100 μL was replaced with fresh ethanol/SCF solution after the removal of each aliquot. A calibration curve was made by analyzing the peak area as a function of standard concentrations of 0.005, 0.01, 0.02, 0.05 mg/mL IBU in ethanol/SCF (1:1 v/v). Experiments were repeated in triplicate. Figure S2.11 provides the calibration curve as well as the release profile of IBU from UiO-AZB nanoparticles.

2.3.10 Caffeine release

The release profiles of caffeine from the IBU loaded UiO-AZB nanoparticles were measured using HPLC. 2.4 mg of the caffeine loaded UiO-AZB nanoparticles were submersed into 5 mL 1:1 (v/v) ethanol/SCF in a 24/40 jointed quartz cuvette. The cuvettes were capped with a rubber septum and kept either wrapped in tin foil (dark conditions) or placed in front of a 1000 W white light source (irradiated conditions). 100 μL aliquots were removed over time from the cuvettes and placed into a glass LC/MS vial. Aliquots were diluted with 900 μL ethanol/SCF (1:1 v/v) and analyzed using HPLC as described *vide supra*. The 100 μL was replaced with fresh ethanol/SCF solution after the removal of each aliquot. A calibration curve was made by

analyzing the peak area as a function of standard concentrations of 0.0005, 0.001, 0.002, 0.005 mg/mL caffeine in ethanol/SCF (1:1 v/v). Experiments were repeated in triplicate. Figure S2.12 provides the calibration curve as well as the release profile of caffeine from UiO-AZB nanoparticles.

2.3.11 Nile Red (NR) release

The release of NR from the NR loaded UiO-AZB was measured using UV-Vis spectroscopy. 2.0 mg of the NR loaded UiO-AZB nanoparticles were submersed into 3 mL 1:1 (v/v) ethanol/SCF in a 24/40 jointed quartz cuvette. The cuvettes were capped with a rubber septum and kept either wrapped in tin foil (dark conditions) or placed in front of a white light source (irradiated conditions). The absorbance spectra from 200-800 nm of the supernatant solutions were measured over time. From the spectra, the absorbance at 575 nm was plotted as a function of time for each light exposure condition. Figure S2.13 confirms that only NR absorbs at this wavelength. Experiments were repeated in triplicate.

2.3.12 Cellular Uptake

HeLa cells were seeded in 35 mm glass bottom petri dishes (MatTek) at 10,000 cells per well and cultured for 24 h at 37 °C and 5% CO_2. To each dish 300 µL of 0.5 mg/mL UiO-AZB loaded with Nile red was added. After 30 min incubation at 37 °C the solution was removed and the cells were washed three time with PBS. Images were acquired using a confocal laser scanning microscope.

2.3.13 Cellular Toxicity

HeLa cells were seeded at 5,000 cells per well in a 96-well plate and cultured for 24 h at 37 °C and 5% CO_2. Solutions of UiO-AZB (2, 5, 10, 25, 50 µg/mL) in DMEM were added to the wells. After 72 h incubation the media was removed and cells were washed three times with

PBS. To each well 10 μL of 5 mg/mL MTT and 90 μL of DMEM were added and incubated at 37 °C. After 4 h the media was removed and the formazan crystals were dissolved in 100 μL DMSO. The absorbance at 570 nm was measured using a microplate reader. Percent viability of the cells was calculated as the ratio of mean absorbance of triplicate readings with respect to mean absorbance of control wells.

2.3.14 Powder X-ray Diffraction (PXRD)

For X-ray diffraction analysis, a 600 W RigakuMiniFlex powder diffractometer operating with a Cu (K_α = 0.15418 nm) radiation source was used, with asweeping range of 3-50° in continuous scanning mode. Data was collected in 0.1° increments at a scanning rate of 1°/min, andpatterns were generated with PDXL software.

2.3.15 Scanning electron microscopy (SEM)

A Leo (Zeiss) 1550 field-emission scanning electron microscope, equipped with an in-lens detector and operating at 5.0 kV, was used to collect SEM images. NPs were prepared for SEM imaging by first dispersing them in ethanol (0.1 mg/mL) via sonication. The resulting solution was then deposited via drop casting, with a short stem Pasteur pipette (1 drop), onto precut 5 mm x 5 mm glass slides. After room temperature drying, slides were mounted onto an SEM sample peg using double sided Cu tape and the sides of the slides were painted with carbon paint. A Cressington 208 High Resolution Sputter Coater with a Au/Pd target (80/20) was used to deposit a conductive layer on the surface of the slides in order to allow for imaging. Samples were coated for 60 seconds.

2.3.16 Transmission Electron Microscopy (TEM)

TEM images and diffraction patterns were obtained using a JEOL 2100 transmission electron microscopewith an accelerating voltage of 200kV. Samples were prepared by depositing

10 μL of UiO-AZB nanoparticles on a 300 mesh carbon coated copper grid (EM Science) and left to dry overnight.

2.3.17 Dynamic Light Scattering (DLS)

The size distribution of the UiO-AZB nanoparticles was measured using a Malvern ZetasizerNano-ZS, with five measurements taken per trial. Nanoparticles were suspended in ethanol via sonication and passed through a 0.45 μm filter prior to measurement.

2.3.18 Thermogravimetric Analysis (TGA)

A Q-series TGA from TA instruments was used to analyze thermal stability of materials. 10 mg of sample in an aluminum pan or a high temperature platinum pan were heated under nitrogen from 25-40 °C up to 600 or 800 °C (respectively with pans) with a heating rate of 10 °C/min.

2.3.19 Gas Sorption Isotherms

The N_2 sorption isotherm measurements were collected on a Quantachrome Autosorb-1 at 77 K. The samples were placed in a 6 mm large bulb sample cell, which was degassed under vacuum for 24 h at 120 °C. The surface areas of the materials were determined by fitting the adsorption data within the 0.05-0.3 P/P_0 pressure range to the BET and Langmuir equations.

2.3.20 White Light Sources

1000 W white light was generated with a Newport LCS-100 solar simulator (AM 1.5G spectrum) equipped with a detachable IR filter. A commercial clamping desk lamp with a 100 W bulb was used to generate 100 W white light. In the case of the 100 W lamp, the IR filter was removed from the solar simulator and mounted between the light source and the sample.

2.3.21 UV-Vis Spectroscopy

Absorbance measurements were taken using a Cary 5000 UV-Vis-NIR spectrometer controlled with Cary WinUV software. Single point measurements at 392 nm were taken using the Simple Reads application for the degradation of UiO-AZB. The Scan application was used to collect spectra from 200-800 nm to observe the release of NR from the UiO-AZB nanoparticles.

2.3.22 High Performance Liquid Chromatography (HPLC)

An Agilent 1100 series HPLC equipped with a G1367A autosampler, quaternary pump, column heater set at 40°C and DAD detector set at 254 nm was used to measure the release of IBU. Separations were obtained through the C_{18}XBridge column (4.6 mm x 25 mm with 5μm spherical packing) using H_2O/ACN (85%:15%) as the isocratic elution solvent. The flow rate was set to 1 mL/min and each run was 6 min.

2.3.23 Confocal Laser Scanning Microscope

A Zeiss LSM 880 confocal microscope was used to obtain images of HeLa cells. Images were collected using the red channel (550-700 nm) at 0.52 μm intervals and stacked in the Z axis. The image was prepared using Zen imaging software.

2.4 Results and Discussion

2.4.1 Characterization

For ultimate applications as nanocarriers for drug cargos we were satisfied to achieve nano-sized particulates using 30 equivalents of acetic acid (AA, 30 mol AA: 1 mol Zr^{4+}). SEM images of the UiO-AZB nanoparticles (Figure 2.2, A) indicate average particle sizes of ~ 107 ± 20 nm with additional confirmation obtained from TEM (104 ± 12, Figure 2.2, C and Figure S2.1) and dynamic light scattering (DLS) data (128 ± 3 nm, Figure S2.2). The structure was confirmed by comparison of the experimental powder X-ray diffraction (PXRD) pattern to the simulated pattern from single crystal data (Figure 2.2, B).[58] The selected area diffraction (SAD) pattern (Figure 2.2, D) also indicates crystallinity of the bulk UiO-AZB with each bright spot representing a lattice reflection within the crystal structure. Crystallinity of individual particles was further confirmed by a fast Fourier transform (FFT) of a single UiO-AZB nanoparticle (Figure 2.2, D). The BET surface area was found to be ~2500 m^2/g (Figure S2.3), which is comparable to the literature report of 3000 m^2/g for micron sized particles.[58]

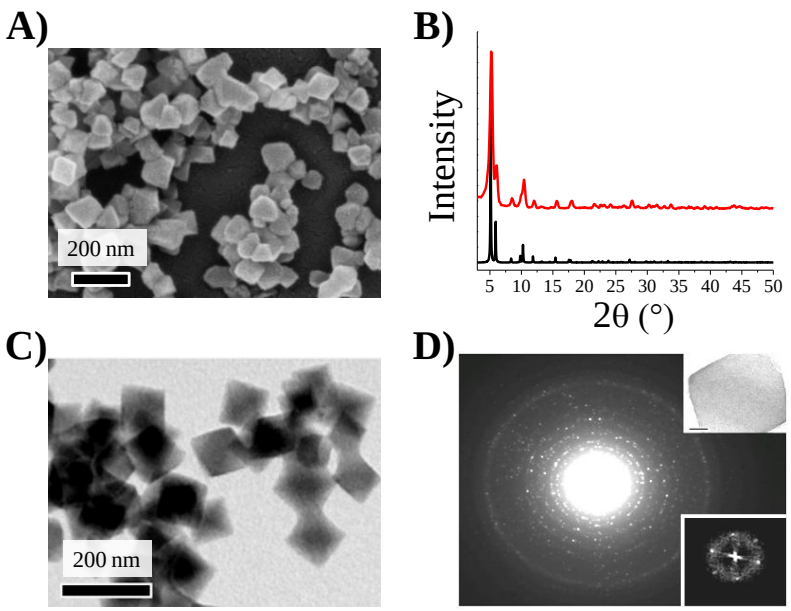

Figure 2.2. A) SEM image of UiO-AZB nanoparticles. B) Experimental (red) and simulated (black) PXRD patterns of UiO-AZB nanoparticles[58] C) TEM image of UiO-AZB nanoparticles. D) Selected area diffraction pattern of UiO-AZB. Top inset shows a high-resolution TEM image. Bottom inset is a fast Fourier transform pattern of a single UiO-AZB nanoparticle.

2.4.2 UiO-AZB Degradation

Upon irradiation with UV light (~330 nm for maximum quantum yield) trans-AZB isomerizes to the cis-AZB form (Scheme 2.1). Trans-AZB exhibits a strong $\pi \rightarrow \pi^*$ absorption at 330 nm (ε ~22000 M^{-1} cm^{-1}) and a weaker $n \rightarrow \pi^*$ at 430 nm (ε ~400 M^{-1} cm^{-1}) (Figure 2.3, A inset and Figure S2.4). Upon transition to the cis-AZB, the $\pi \rightarrow \pi^*$ transition shifts to ~250 nm and decreases in intensity (ε ~11000 M^{-1} cm^{-1}). The $n \rightarrow \pi^*$ transition remains at 430 nm but is intensified (ε ~1500 M^{-1} cm^{-1}). These results mirror the reported values for the decarboxylated parent azobenzene.[63] The transition between the two distinct states occurs with the maintenance of two major isosbestic points (285 nm and 392 nm). These spectral features were used to investigate the degradation profiles of the UiO-AZB nanoparticles.

Submersing the nanoparticles into a solution of simulated cerebrospinal fluid (SCF, chosen for ultimate applications in brain cancer, see Supplemental Information for composition) causes them to decompose and break apart into metal ions and linkers. These labile species are then capable of rapidly diffusing into solution. The absorbance features of the AZB linker mentioned above, due to *free* AZB (no longer bound to the MOF), thus appears over time in the solution above the submersed solid material. Therefore, this absorbance, measured with UV-Vis as a function of time (Figure 2.3A), is a direct measurement of MOF degradation and the % degradation of the UiO-AZB nanoparticles with respect to time (*t*) can then be calculated from the absorbance data using equations 1-3, as adapted from a previous report.[52]

$$\frac{Abs_t}{\varepsilon_{392\ nm}} = C_{AZB(E)} \quad (1)$$

Where Abs_t is the measured absorbance (392 nm) at time *t*, ε is the extinction coefficient, and $C_{AZB(E)}$ is the experimental concentration of AZB.

$$\frac{6m}{(MW_{UiO-AZB})*\mathrm{V}} = C_{AZB\ (T)} \quad (2)$$

Where *m* is the mass of UiO-AZB used, converted to mol AZB by dividing by the molecular weight of UiO-AZB ($MW_{UiO\text{-}AZB}$, 2877.344 g/mol) and multiplying by the molar ratio of 6 mol AZB : 1 mol UiO-AZB. Dividing this value by the volume of SCF added (*V*) gives is the total concentration of AZB ($C_{AZB(T)}$), assuming 100 % degradation of the original UiO-AZB sample.

$$\frac{C_{AZB\ (E)}}{C_{AZB\ (T)}} \times 100\% = \%\ degradation \quad (3)$$

To test the efficacy of this material for photo-induced cargo release, the degradation of UiO-AZB nanoparticles in the dark must be compared to the degradation

during continuous irradiation with white light (Figure 2.3, B). To ensure measurement of total AZB concentration, independent of trans → cis isomerization, the absorbance was monitored at an isosbestic point (392 nm). It was found that the UiO-AZB is relatively stable in the dark (~10 % degraded over 8 h) but degradation is drastically enhanced when irradiated with light as evidenced by ~60 % degradation over the 8 h period.

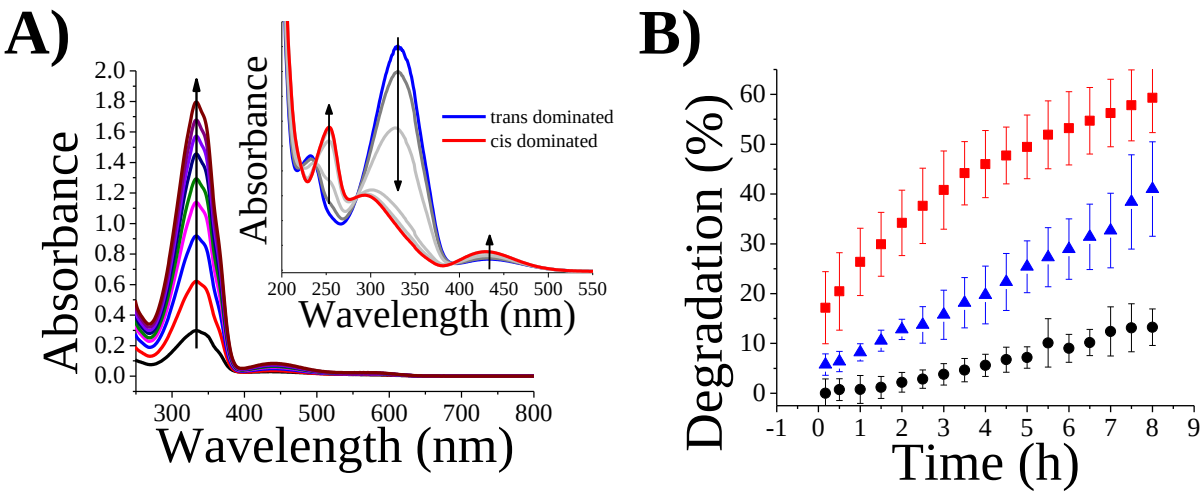

Figure 2.3. A) Representative spectra recorded as a function of time during a degradation experiment of UiO-AZB in simulated cerebrospinal fluid (arrow indicates increased time), inset: the steady state spectra of the trans-dominated AZB form (blue) and cis-dominated AZB form (red). B) Degradation (%) of UiO-AZB nanoparticles over time in the dark (black), under irradiation with 100 W white light (blue), and under irradiation with 1000 W white light (red).

The degradation profile plateaus at the 60 % maximum due to the saturation of AZB in the degradation media. This solubility limit however, will not be reached in biological systems due to the continuous flow of biological fluid. Therefore, the rate of degradation was approximated from the initial linear region of the degradation profile (up to 3 h, Figure S2.5). In the dark, the rate was found to be 1.3 ± 0.1 %/h. The rate of photo-initiated degradation was light intensity dependent, where at lower intensity (100 W) the rate of release was 3.8 ± 0.2 %/h and this rate approximately doubled to 8.4 ± 0.4 %/h at

higher intensity (1000 W, Figure 2.3, B and S5). To avoid the interference of thermal effects on the degradation, an IR filter was used. The temperature was also monitored throughout the measurement and maintained at 23 ± 2 °C.

2.4.3 Drug Loading and Release

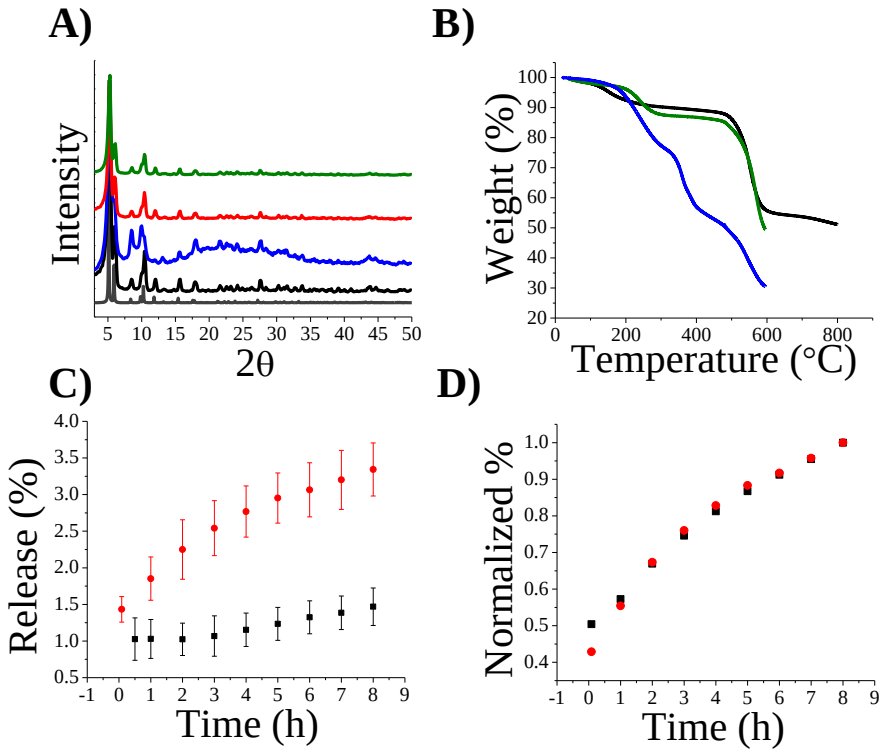

Figure 2.4. A) PXRD of the simulated UiO-AZB pattern[58] (gray), experimental UiO-AZB nanoparticles (black), IBU-loaded UiO-AZB (blue), NR-loaded UiO-AZB (red), and caffeine-loaded UiO-AZB (green). B) TGA of UiO-AZB nanoparticles (black), IBU-loaded UiO-AZB (blue) and caffeine-loaded UiO-AZB (green). C) NR release (%) from loaded UiO-AZB nanoparticles with no irradiation (black) and under irradiation with 1000 W white light (red).D) Normalized degradation (black) and release (red) of NR calculated from the absorbance scans under irradiation with 1000 W white light.

The pore environment of UiO-AZB should be inherently hydrophobic due to the aromatic AZB linkers and so, we speculated that the material would be selective for hydrophobic cargos. To test this hypothesis we loaded model drugs ibuprofen (IBU, hydrophobic) and caffeine (caff, hydrophilic) into the evacuated UiO-AZB nanoparticles via a simple impregnation method. PXRD data (Figure 2.4, A) of the loaded materials confirms that the structure remains intact during the loading procedure. The degree of IBU and caffeine loading (38.2 and 3.4 wt%, respectively) was determined via TGA (Figure 2.4, B). Evidenced by a wt% loading over 10 times greater for the IBU than the caffeine, our original assumption that UiO-AZB would be selective for hydrophobic drug molecules was supported. Additional analysis of the release of these drug models further substantiated our claim. The release profiles of IBU and caffeine were analyzed as a function of time using HPLC (Figure S2.9 and S10, respectively). After an initial small release of IBU into the media, no further release was observed irrespective of irradiation (Figure S2.9), suggesting that the IBU bound to the UiO-AZB nanoparticles, supported by FT-IR data (Figure S2.6). In the case of caffeine release, the entire cargo is released within the first 3 hours when kept in the dark (Figure S2.10) and therefore, no control was offered by UiO-AZB degradation. These results are interesting because they provide evidence regarding the pore environment and potential cargo preferences material. Further investigations are underway to manipulate the pore environment through linker modification.

The dye Nile Red (NR) was also loaded into the UiO-AZB nanoparticles with maintenance of the UiO-AZB structure (Figure 2.4 A). Loading experiments were carried out via the same impregnation method as for the IBU and caffeine loadings. However,

NR was loaded from the impregnation solutions with drastically reduced NR concentration due to loss of structural integrity of UiO-AZB at higher concentrations of NR (Figure S2.7). UV-Vis analysis of a digested solution of NR loaded samples allowed for the calculation of the degree of NR loading. The maximum amount of NR loaded into the nanoparticles was determined to be 4.3 wt%.

NR release was monitored via electronic absorption spectroscopy in the same fashion as the degradation experiments for the naked UiO-AZB. The UV-Vis spectrum of NR contains a peak with λ_{max} at 575 nm (Figure S2.11). This makes the release of NR easily detectable as AZB does not absorb at this wavelength. This also enables the simultaneous measurement of UiO-AZB degradation and NR release. Degradation was measured by the increase in AZB absorbance at 392 nm, while release was calculated from the NR absorbance at 575 nm (Figure S2.11). Upon irradiation of NR-loaded UiO-AZB, we observe the first example of photo-triggered degradation and the resultant release of a cargo from a MOF nanocarrier (Figure 2.4, C). Comparison of the degradation and release profiles (Figure S2.13) shows similar rates for both processes in the dark and under illumination (0.02 ± 0.02 %/h and 0.04 ± 0.01 %/h in the dark, and 0.30 ± 0.01 %/h vs 0.36 ± 0.02 %/h under illumination, respectively). The rate of NR release from UiO-AZB increased 9-fold in comparison to release in the dark (0.04 ± 0.01 %/h vs. 0.36 ± 0.02 %/ h, Figure S2.13). From the quantification of these rates, two conclusions become apparent. 1) The loading of NR into the MOF imparts additionally stability. The degradation of the parent UiO-AZB in the dark decreased from 1.3± 0.1 %/h to an impressive 0.02± 0.02 %/h when loaded. 2) The mechanism of release is dominated by photo-degradation. This is best visualized through normalization and overlay of the degradation and release profiles (Figure 2.4, D). These results provide a platform for the further development of MOF photo-cages.

2.4.4 Cytotoxicity and Cell Uptake

Encouraged by the photo-induced degradation and release data (Figure 2.3, B and 2.4, C), and with our target application being nanocarriers for drug delivery, we tested *in vitro* cellular uptake of UiO-AZB nanoparticles and their cytotoxicity in the absence of light. HeLa cells were incubated for 30 minutes with 0.5 mg/mL of NR loaded UiO-AZB nanoparticles. UiO-AZB nanoparticles were rapidly and efficiently transported across the membrane into the HeLa cells within that time period. Cell uptake was evaluated by acquiring fluorescent confocal microscopy images of 0.52 μm-thick cross-sectional slices perpendicular to the plane of the cell monolayer (Figure 2.5). The z-slices showed that distinct fluorescent nanoparticles were present in different planes throughout the thickness of the cell confirming that nanoparticles were indeed inside the cells and not simply adsorbed to the outer surface. Furthermore, no cytotoxicity was observed when HeLa cells were treated 72 h with UiO-AZB nanoparticles at concentrations of 2-50 μg/mL (Figure S2.14). This extremely low/no toxicity is expected when the LD_{50} of azobenzene (1000 mg/kg; rat) and the inherently nontoxic nature of Zr^{4+} are considered.

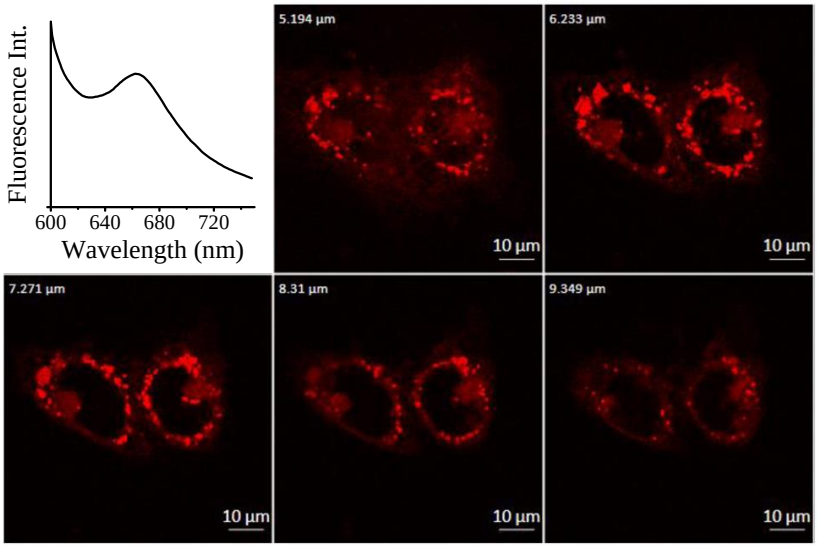

Figure 2.5. Top Left: Emission spectra of NR loaded UiO-AZB with excitation at 575 nm. Remaining Panels: Z-stack of HeLa cells incubated with NR loaded UiO-AZB nanoparticles

2.5 Conclusions

In summary, UiO-AZB MOFs provide a new prototype for the development of MOF photo-cages. Herein, we have demonstrated photo-induced degradation and photo-controlled release of a NR cargo and provided evidence that these MOF photo-cages are selective for hydrophobic cargos. Additionally, the degradation of UiO-AZB was shown to be controllable as faster degradation was observed with increased incident light intensity, potentially offering a mechanism by which to control the rate of cargo release. Additionally, the particles were shown to readily enter cancer cells, as evidenced by confocal microscopy. This preliminary "proof of concept" report establishes a new method by which to design MOF photo-cages, where material degradation is a desirable mechanism to deliver cargo loads. The synthetic tunability of the UiO-AZB pore environment and therefore cargo/MOF interactions provides a platform for tuning MOF materials to a specific application.

2.6 Acknowledgements

The authors would like to thank the VT Department of Chemistry and the Institute for Critical Technology and Applied Science (ICTAS) housed on the campus of VT for support and funding of this work. Additional thanks to Dr. Kristi DeCourcy for help with confocal microscopy imaging and the Nanoscale Characterization and Fabrication Lab (NCFL) at VT for the use of the SEM and TEM facility.

2.7 References

1. J. H. Kaplan, B. F., J. F. Hoffman, Rapid Photolytic Release of Adenosine 5'-Triphosphate from a Protected Analogue: Utilization by the Na:K Pump of Human Red Blood Cell Ghosts. *Biochemistry* **1978,** *17*, 1929-1935.

2. Chilkoti, A.; Dreher, M. R.; Meyer, D. E.; Raucher, D., Targeted Drug Delivery by Thermally Responsive Polymers. *Advanced Drug Delivery Reviews* **2002,** *54* (5), 613-630.

3. Meyer, D. E.; Shin, B. C.; Kong, G. A.; Dewhirst, M. W.; Chilkoti, A., Drug Targeting Using Thermally Responsive Polymers and Local Hyperthermia. *Journal of Controlled Release* **2001,** *74* (1–3), 213-224.

4. Dai, S.; Ravi, P.; Tam, K. C., Ph-Responsive Polymers: Synthesis, Properties and Applications. *Soft Matter* **2008,** *4* (3), 435-449.

5. Brieke, C.; Rohrbach, F.; Gottschalk, A.; Mayer, G.; Heckel, A., Light-Controlled Tools. *Angewandte Chemie International Edition* **2012,** *51* (34), 8446-8476.

6. Sortino, S., Photoactivated Nanomaterials for Biomedical Release Applications. *Journal of Materials Chemistry* **2012,** *22* (2), 301-318.

7. Wang, Z.; Johns, V. K.; Liao, Y., Controlled Release of Fragrant Molecules with Visible Light. *Chemistry – A European Journal* **2014,** *20* (45), 14637-14640.

8. Paret, N.; Trachsel, A.; Berthier, D. L.; Herrmann, A., Controlled Release of Encapsulated Bioactive Volatiles by Rupture of the Capsule Wall through the Light-Induced Generation of a Gas. *Angewandte Chemie International Edition* **2015,** *54* (7), 2275-2279.

9. Herrmann, A., Controlled Release of Volatiles under Mild Reaction Conditions: From Nature to Everyday Products. *Angewandte Chemie International Edition* **2007,** *46* (31), 5836-5863.

10. Wang, B.; Côté, A. P.; Furukawa, H.; O'Keeffe, M.; Yaghi, O. M., Colossal Cages in Zeolitic Imidazolate Frameworks as Selective Carbon Dioxide Reservoirs. *Nature* **2008,** *453* (7192), 207-211.

11. He, Y.; Zhou, W.; Qian, G.; Chen, B., Methane Storage in Metal-Organic Frameworks. *Chemical Society Reviews* **2014,** *43* (16), 5657-5678.

12. Yamamoto, C. F.; Pereira, E. I.; Mattoso, L. H. C.; Matsunaka, T.; Ribeiro, C., Slow Release Fertilizers Based on Urea/Urea–Formaldehyde Polymer Nanocomposites. *Chemical Engineering Journal* **2016,** *287*, 390-397.

13. Rashidzadeh, A.; Olad, A., Slow-Released Npk Fertilizer Encapsulated by Naalg-G-Poly(Aa-Co-Aam)/Mmt Superabsorbent Nanocomposite. *Carbohydrate Polymers* **2014,** *114*, 269-278.

14. Ni, B.; Liu, M.; Lü, S.; Xie, L.; Wang, Y., Multifunctional Slow-Release Organic−Inorganic Compound Fertilizer. *Journal of Agricultural and Food Chemistry* **2010,** *58* (23), 12373-12378.

15. Zhan, F.; Liu, M.; Guo, M.; Wu, L., Preparation of Superabsorbent Polymer with Slow-Release Phosphate Fertilizer. *Journal of Applied Polymer Science* **2004,** *92* (5), 3417-3421.

16. Ciesienski, K. L.; Franz, K. J., Keys for Unlocking Photolabile Metal-Containing Cages. *Angewandte Chemie International Edition* **2011,** *50* (4), 814-824.

17. Zayat, L.; Calero, C.; Alborés, P.; Baraldo, L.; Etchenique, R., A New Strategy for Neurochemical Photodelivery: Metal−Ligand Heterolytic Cleavage. *Journal of the American Chemical Society* **2003,** *125* (4), 882-883.

18. Huang, Y.; Dong, R.; Zhu, X.; Yan, D., Photo-Responsive Polymeric Micelles. *Soft Matter* **2014,** *10* (33), 6121-6138.

19. Fan, N.-C.; Cheng, F.-Y.; Ho, J.-a. A.; Yeh, C.-S., Photocontrolled Targeted Drug Delivery: Photocaged Biologically Active Folic Acid as a Light-Responsive Tumor-Targeting Molecule. *Angewandte Chemie International Edition* **2012,** *51* (35), 8806-8810.

20. Esser-Kahn, A. P.; Odom, S. A.; Sottos, N. R.; White, S. R.; Moore, J. S., Triggered Release from Polymer Capsules. *Macromolecules* **2011,** *44* (14), 5539-5553.

21. Bansal, A.; Zhang, Y., Photocontrolled Nanoparticle Delivery Systems for Biomedical Applications. *Accounts of Chemical Research* **2014,** *47* (10), 3052-3060.

22. Alvarez-Lorenzo, C.; Bromberg, L.; Concheiro, A., Light-Sensitive Intelligent Drug Delivery Systems. *Photochemistry & Photobiology* **2009,** *85* (4), 848-860.

23. Deniz, E.; Kandoth, N.; Fraix, A.; Cardile, V.; Graziano, A. C. E.; Lo Furno, D.; Gref, R.; Raymo, F. M.; Sortino, S., Photoinduced Fluorescence Activation and Nitric Oxide Release with Biocompatible Polymer Nanoparticles. *Chemistry – A European Journal* **2012,** *18* (49), 15782-15787.

24. Swaminathan, S.; Garcia-Amoros, J.; Fraix, A.; Kandoth, N.; Sortino, S.; Raymo, F. M., Photoresponsive Polymer Nanocarriers with Multifunctional Cargo. *Chemical Society Reviews* **2014,** *43* (12), 4167-4178.

25. Stoffelen, C.; Voskuhl, J.; Jonkheijm, P.; Huskens, J., Dual Stimuli-Responsive Self-Assembled Supramolecular Nanoparticles. *Angewandte Chemie International Edition* **2014,** *53* (13), 3400-3404.

26. Shum, P.; Kim, J.-M.; Thompson, D. H., Phototriggering of Liposomal Drug Delivery Systems. *Advanced Drug Delivery Reviews* **2001,** *53* (3), 273-284.

27. Yavlovich, A.; Smith, B.; Gupta, K.; Blumenthal, R.; Puri, A., Light-Sensitive Lipid-Based Nanoparticles for Drug Delivery: Design Principles and Future Considerations for Biological Applications. *Molecular Membrane Biology* **2010,** *27* (7), 364-381.

28. Wang, Y.; Li, G.; Cheng, R.; Zhang, X.; Jiang, J., NIR- and UV-Dual Responsive Amphiphilic Copolymer Micelles with Light-Dissociable Pag-Side Groups. *Colloid and Polymer Science* **2017**, 1-8.

29. Du, X.; Jiang, G.; Li, L.; Liu, Y.; Chen, H.; Huang, Q., Photo-Induced Synthesis Glucose-Responsive Carriers for Controlled Release of Insulin in Vitro. *Colloid and Polymer Science* **2015,** *293* (7), 2129-2135.

30. Zhao, Y., Photocontrollable Block Copolymer Micelles: What Can We Control? *Journal of Materials Chemistry* **2009,** *19* (28), 4887-4895.

31. Schumers, J.-M.; Fustin, C.-A.; Gohy, J.-F., Light-Responsive Block Copolymers. *Macromolecular Rapid Communications* **2010,** *31* (18), 1588-1607.

32. Huabing Chen, L. X., Yasutaka Anraku, Peng Mi, Xueying Liu, Horacio Cabral, Aki Inoue, Takahiro Nomoto, Akihiro Kishimura, Nobuhiro Nishiyama, and Kazunori Kataoka

Polyion Complex Vesicles for Photoinduced Intracellular Delivery of Amphiphilic Photosensitizer. *Journal of the American Chemical Society* **2014,** *136* (1), 157-163.

33. Cabane, E.; Malinova, V.; Menon, S.; Palivan, C. G.; Meier, W., Photoresponsive Polymersomes as Smart, Triggerable Nanocarriers. *Soft Matter* **2011,** *7* (19), 9167-9176.
34. Ruggiero, E.; Alonso-de Castro, S.; Habtemariam, A.; Salassa, L., Upconverting Nanoparticles for the near Infrared Photoactivation of Transition Metal Complexes: New Opportunities and Challenges in Medicinal Inorganic Photochemistry. *Dalton Transactions* **2016,** *45* (33), 13012-13020.
35. Fallah, M.; MacKenzie, K.; Hanna, J.; Page, S., Novel Photoactive Inorganic Polymer Composites of Inorganic Polymers with Copper(I) Oxide Nanoparticles. *Journal of Materials Science* **2015,** *50* (22), 7374-7383.
36. Kamat, P. V., Photophysical, Photochemical and Photocatalytic Aspects of Metal Nanoparticles. *The Journal of Physical Chemistry B* **2002,** *106* (32), 7729-7744.
37. Fomina, N.; Sankaranarayanan, J.; Almutairi, A., Photochemical Mechanisms of Light-Triggered Release from Nanocarriers. *Advanced Drug Delivery Reviews* **2012,** *64* (11), 1005-1020.
38. Huang, J.; Jackson, K. S.; Murphy, C. J., Polyelectrolyte Wrapping Layers Control Rates of Photothermal Molecular Release from Gold Nanorods. *Nano Letters* **2012,** *12* (6), 2982-2987.
39. Liu, G.; Dong, C.-M., Photoresponsive Poly(S-(O-Nitrobenzyl)-L-Cysteine)-B-Peo from a L-Cysteine N-Carboxyanhydride Monomer: Synthesis, Self-Assembly, and Phototriggered Drug Release. *Biomacromolecules* **2012,** *13* (5), 1573-1583.

40. McDonald, T. M.; Lee, W. R.; Mason, J. A.; Wiers, B. M.; Hong, C. S.; Long, J. R., Capture of Carbon Dioxide from Air and Flue Gas in the Alkylamine-Appended Metal–Organic Framework Mmen-Mg2(Dobpdc). *Journal of the American Chemical Society* **2012,** *134* (16), 7056-7065.

41. Furukawa, H.; Cordova, K. E.; O'Keeffe, M.; Yaghi, O. M., The Chemistry and Applications of Metal-Organic Frameworks. *Science* **2013,** *341* (6149).

42. Lee, J.; Farha, O. K.; Roberts, J.; Scheidt, K. A.; Nguyen, S. T.; Hupp, J. T., Metal-Organic Framework Materials as Catalysts. *Chemical Society Reviews* **2009,** *38* (5), 1450-1459.

43. Liu, J.; Chen, L.; Cui, H.; Zhang, J.; Zhang, L.; Su, C.-Y., Applications of Metal-Organic Frameworks in Heterogeneous Supramolecular Catalysis. *Chemical Society Reviews* **2014,** *43* (16), 6011-6061.

44. Della Rocca, J.; Liu, D.; Lin, W., Nanoscale Metal–Organic Frameworks for Biomedical Imaging and Drug Delivery. *Accounts of Chemical Research* **2011,** *44* (10), 957-968.

45. Horcajada, P.; Chalati, T.; Serre, C.; Gillet, B.; Sebrie, C.; Baati, T.; Eubank, J. F.; Heurtaux, D.; Clayette, P.; Kreuz, C.; Chang, J.-S.; Hwang, Y. K.; Marsaud, V.; Bories, P.-N.; Cynober, L.; Gil, S.; Férey, G.; Couvreur, P.; Gref, R., Porous Metal–Organic-Framework Nanoscale Carriers as a Potential Platform for Drug Delivery and Imaging. *Nature Materials* **2010,** *9* (2), 172-178.

46. He, C.; Liu, D.; Lin, W., Nanomedicine Applications of Hybrid Nanomaterials Built from Metal–Ligand Coordination Bonds: Nanoscale Metal–Organic Frameworks and Nanoscale Coordination Polymers. *Chemical Reviews* **2015,** *115* (19), 11079-11108.

47. Horcajada, P.; Gref, R.; Baati, T.; Allan, P. K.; Maurin, G.; Couvreur, P.; Férey, G.; Morris, R. E.; Serre, C., Metal–Organic Frameworks in Biomedicine. *Chemical Reviews* **2012,** *112* (2), 1232-1268.

48. Tamames-Tabar, C.; Cunha, D.; Imbuluzqueta, E.; Ragon, F.; Serre, C.; Blanco-Prieto, M. J.; Horcajada, P., Cytotoxicity of Nanoscaled Metal-Organic Frameworks. *The Journal of Materials Chemistry B* **2014,** *2* (3), 262-271.

49. An, J.; Geib, S. J.; Rosi, N. L., Cation-Triggered Drug Release from a Porous Zinc−Adeninate Metal−Organic Framework. *Journal of the American Chemical Society* **2009,** *131* (24), 8376-8377.

50. Tan, L.-L.; Li, H.; Qiu, Y.-C.; Chen, D.-X.; Wang, X.; Pan, R.-Y.; Wang, Y.; Zhang, S. X.-A.; Wang, B.; Yang, Y.-W., Stimuli-Responsive Metal-Organic Frameworks Gated by Pillar[5]Arene Supramolecular Switches. *Chemical Science* **2015,** *6* (3), 1640-1644.

51. Nagata, S.; Kokado, K.; Sada, K., Metal-Organic Framework Tethering Pnipam for on-Off Controlled Release in Solution. *Chemical Communications* **2015,** *51* (41), 8614-8617.

52. di Nunzio, M. R.; Agostoni, V.; Cohen, B.; Gref, R.; Douhal, A., A "Ship in a Bottle" Strategy to Load a Hydrophilic Anticancer Drug in Porous Metal Organic Framework Nanoparticles: Efficient Encapsulation, Matrix Stabilization, and Photodelivery. *Journal of Medicinal Chemistry* **2014,** *57* (2), 411-420.

53. Lu, K.; He, C.; Lin, W., A Chlorin-Based Nanoscale Metal–Organic Framework for Photodynamic Therapy of Colon Cancers. *Journal of the American Chemical Society* **2015,** *137* (24), 7600-7603.

54. Lu, K.; He, C.; Lin, W., Nanoscale Metal–Organic Framework for Highly Effective Photodynamic Therapy of Resistant Head and Neck Cancer. *Journal of the American Chemical Society* **2014,** *136* (48), 16712-16715.

55. Meng, X.; Gui, B.; Yuan, D.; Zeller, M.; Wang, C., Mechanized Azobenzene-Functionalized Zirconium Metal-Organic Framework for on-Command Cargo Release. *Science Advances* **2016,** *2* (8).

56. Willem P. R. Deleu, G. R., Roberto F. A. Teixeira, Filip E. Du Prez, and Dirk E. De Vos, Metal–Organic Frameworks Encapsulated in Photocleavable Capsules for Uv-Light Triggered Catalysis. *Chemistry of Materials* **2015,** *27* (16), 5495-5502.

57. Allen, C. A.; Cohen, S. M., Near-Uv Photo-Induced Modification in Isoreticular Metal-Organic Frameworks. *Journal of Materials Chemistry* **2012,** *22* (20), 10188-10194.

58. Schaate, A.; Dühnen, S.; Platz, G.; Lilienthal, S.; Schneider, A. M.; Behrens, P., A Novel Zr-Based Porous Coordination Polymer Containing Azobenzenedicarboxylate as a Linker. *European Journal of Inorganic Chemistry* **2012,** *2012* (5), 790-796.

59. Yang, Q.; Guillerm, V.; Ragon, F.; Wiersum, A. D.; Llewellyn, P. L.; Zhong, C.; Devic, T.; Serre, C.; Maurin, G., Ch4 Storage and Co2 Capture in Highly Porous Zirconium Oxide Based Metal-Organic Frameworks. *Chemical Communications* **2012,** *48* (79), 9831-9833.

60. Mary, L. J. F.; Kannan, P., Synthesis, Characterization and Thermal Behaviour of Poly(Pyromellitimide-Ester)S and (Imide-Urethane)S Containing Azobenzene Units. *European Polymer Journal* **1998,** *35* (1), 17-26.

61. Artificial Cerebrospinal Fluid, Hepes-Buffered. *Cold Spring Harbor Protocols* **2011,** *2011* (10), pdb.rec066696.

62. Horcajada, P.; Serre, C.; Vallet-Regí, M.; Sebban, M.; Taulelle, F.; Férey, G., Metal–Organic Frameworks as Efficient Materials for Drug Delivery. *Angewandte Chemie International Edition* **2006,** *45* (36), 5974-5978.

63. Bandara, H. M. D.; Burdette, S. C., Photoisomerization in Different Classes of Azobenzene. *Chemical Society Reviews* **2012,** *41* (5), 1809-1825.

2.8 Supporting Information

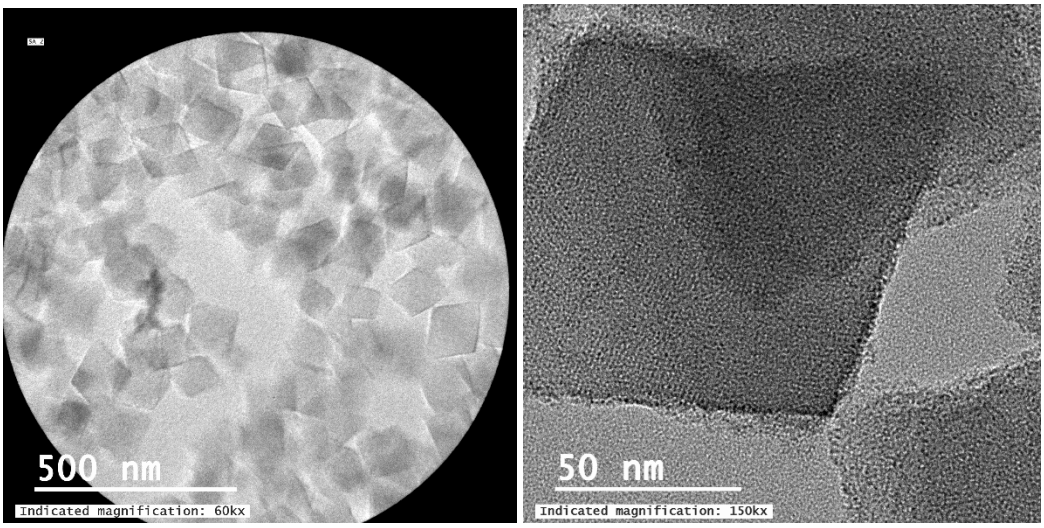

Figure S2.1. Left: High-resolution TEM image showing area selected for selected area diffraction. Right:Additional high-resolution TEM image of UiO-AZB nanoparticles showing sharp defined edges.

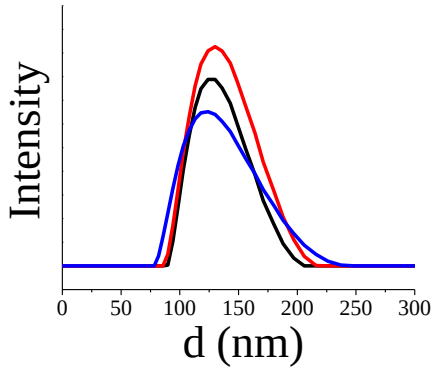

Figure S2.2. The DLS of UiO-AZB nanoparticles indicates an average particle size of 128 ± 3 nm.

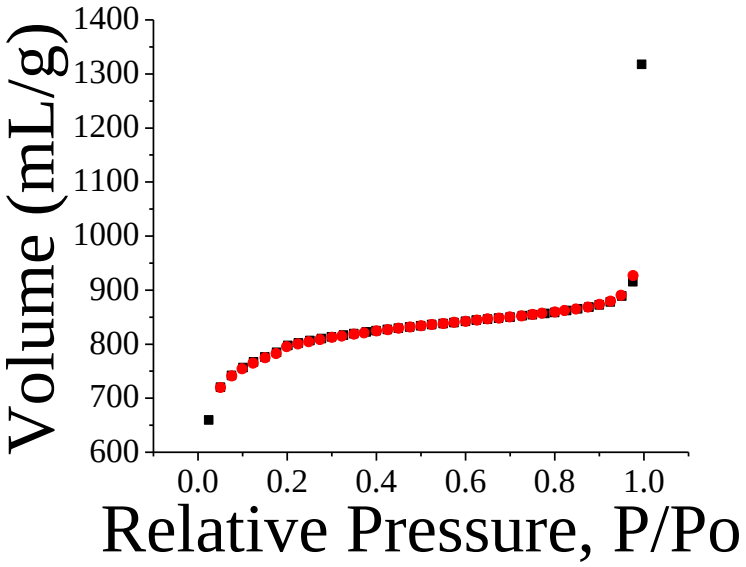

Figure S2.3. N_2 adsorption (black) and desorption (red) isotherms used to calculate BET surface area of 2465 m^2/g. The shape is indicative of a type II isotherm which is characteristic of macroporous materials.

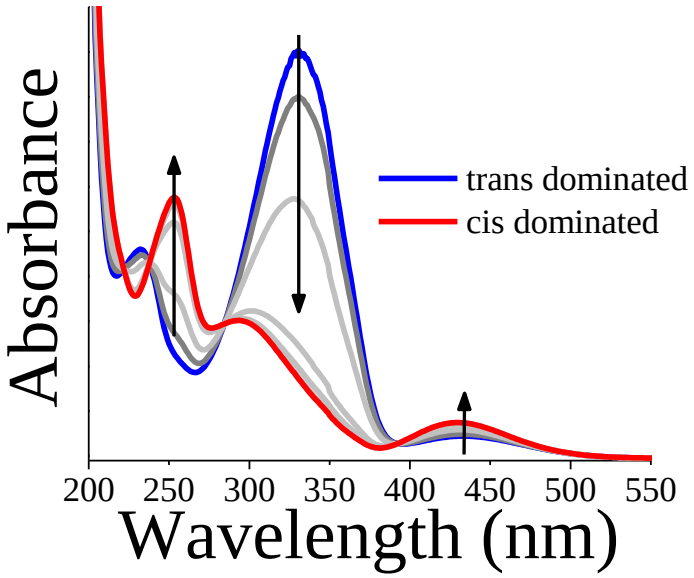

Figure S2.4. Isomerization of trans-AZB (blue) to cis-AZB (red) upon irradiation with a 355 nm laser as measured in a 0.3 mM solution of AZB in basic water.

The degradation of the UiO-AZB was monitored by submersing 0.5 mg into 3 mL of a 1:1 (v/v) solution of ethanol and SCF in a 24/40 jointed quartz cuvette. The cuvette was capped with a rubber septum and either wrapped in tin foil (dark conditions) or placed in front of the light source (irradiated conditions). The absorbance at 392 nm (isosbestic point) of the supernatant solution was measured as a function of time. Experiments were replicated 3 times.

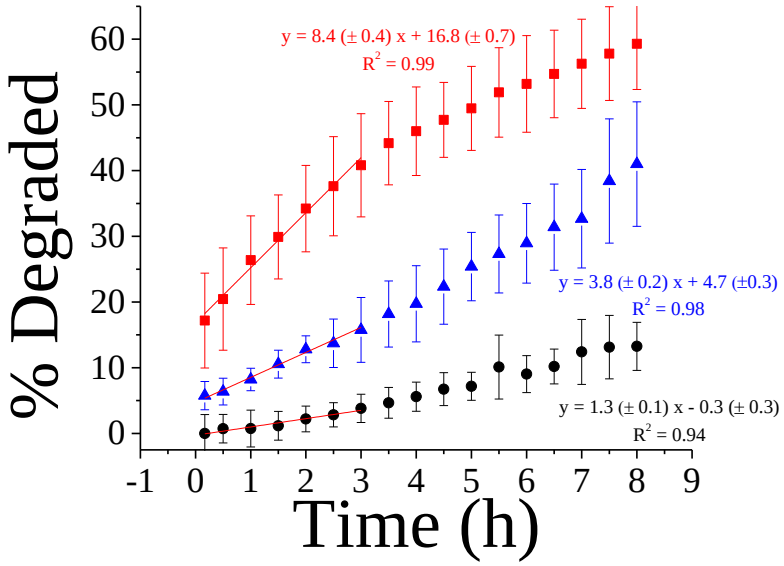

Figure S2.5. Initial degradation rates of the UiO-AZB nanoparticles in the dark (black), under irradiation with 1000 W light (red), and with 100 W light (blue).

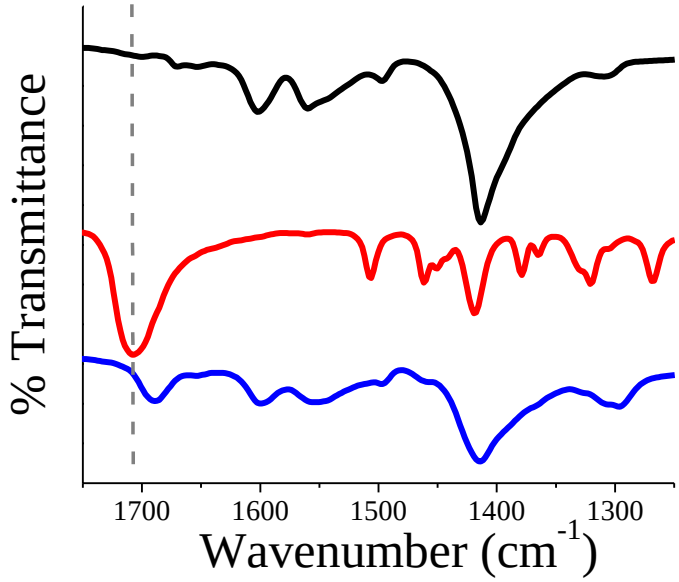

Figure S2.6. FTIR of UiO-AZB (black), IBU (red), and IBU loaded UiO-AZB (blue). The peak from the C=O stretch of pure IBU at 1706 cm^{-1} shifts to 1690 cm^{-1} when loaded into the UiO-AZB nanoparticles, indicative of IBU binding to the metal nodes.

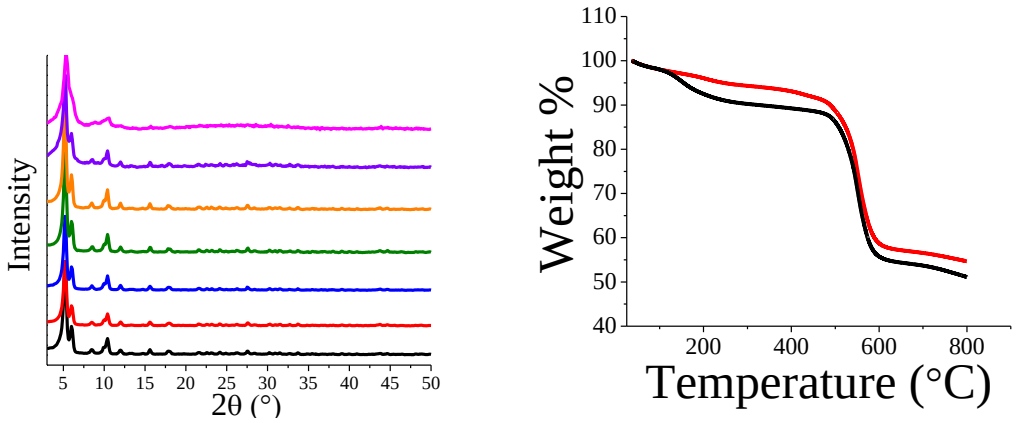

Figure S2.7. Left: PXRD taken of the NR loaded UiO-AZB with increasing concentrations of NR in the loading solution (black, 29 μM; red, 34 μM; blue, 38 μM; green, 43 μM; orange, 48 μM; purple, 60 μM; magenta, 72 μM). Right: TGA of NR loaded UiO-AZB (red) compared with UiO-AZB (black). Therefore, TGA could not be used to accurately determine NR loading.

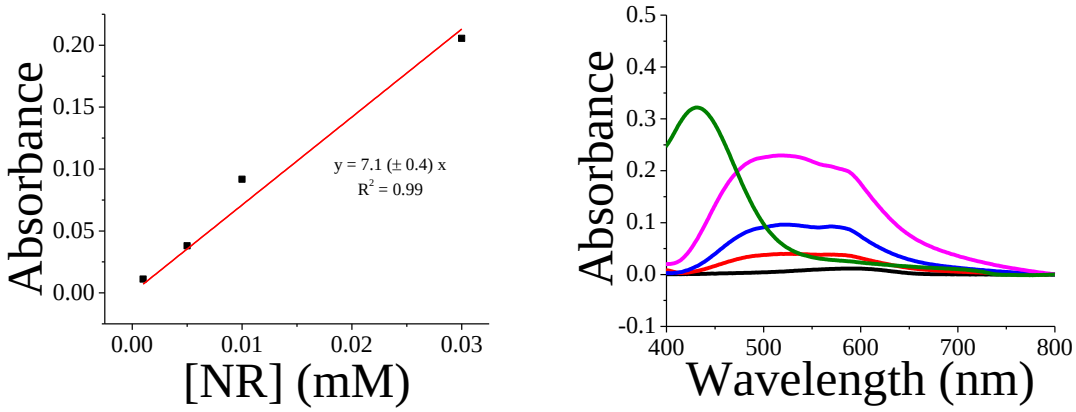

Figure S2.8. Left: Calibration curve of NR in 50 mM NaH_2PO_4at 575 nm. Right: UV-Vis spectra of the standard solutions of NR (black, 0.001 mM; red 0.005 mM; blue, 0.01 mM; magenta, 0.03 mM) and the digested NR loaded UiO-AZB nanoparticles (green).

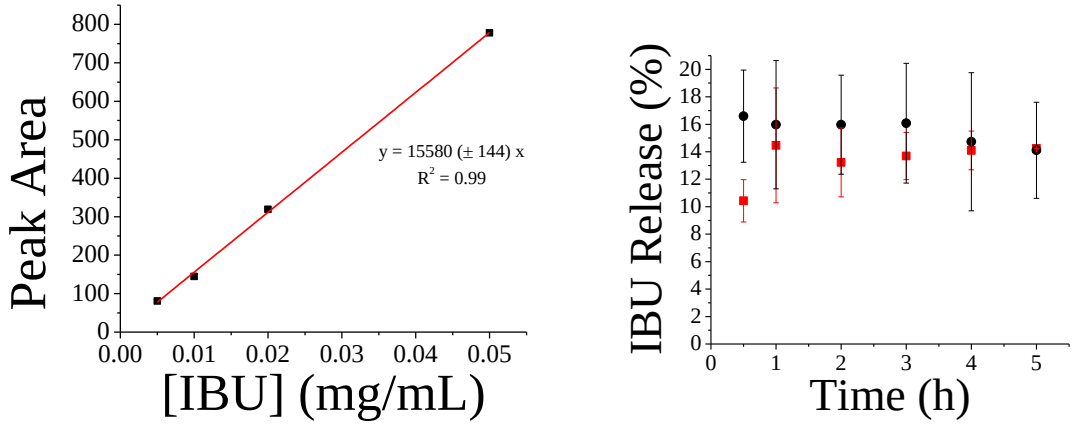

Figure S2.9. Left: Calibration curve of IBU. Right: IBU release from UiO-AZB in the dark (black circles) and upon irradiation with 1000 W white light (red squares) indicating rapid diffusion from the material and no release dependence on irradiation.

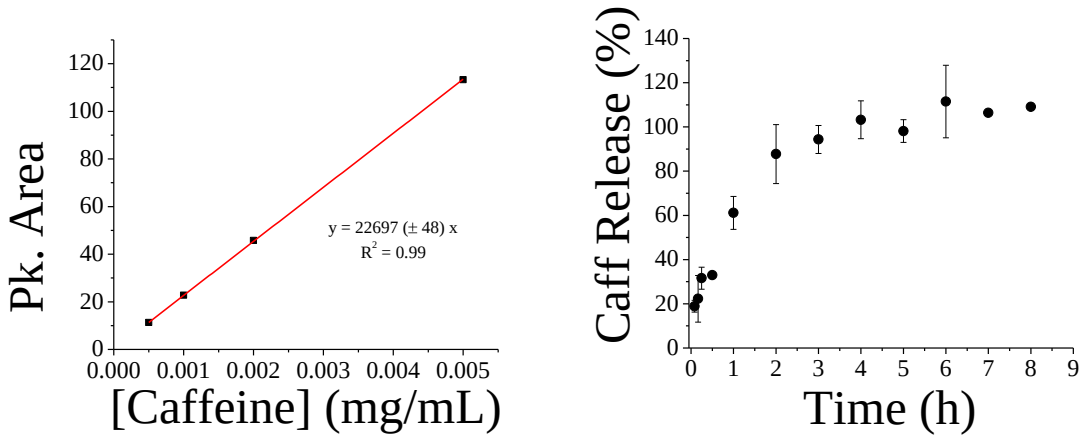

Figure S2.10. Left: Calibration curve for caffeine. Right: caffeine release from UiO-AZB in the dark (black circles) indicating rapid diffusion of caffeine from the material in the dark.

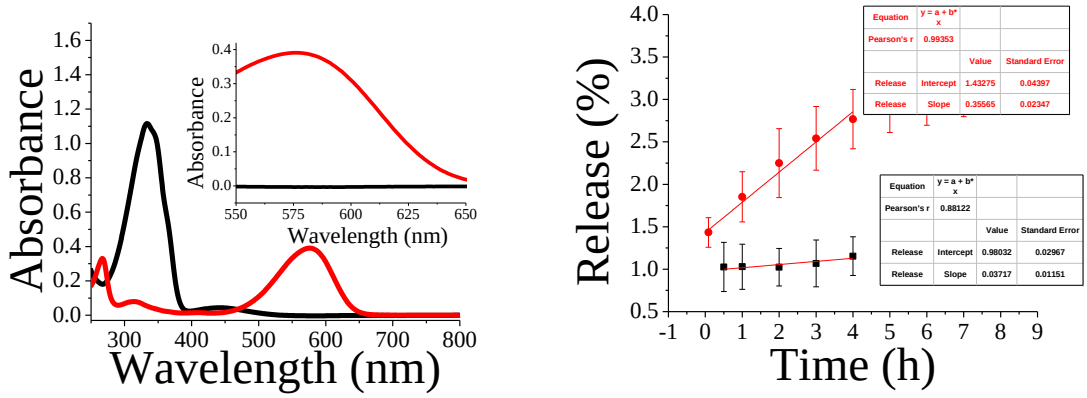

Figure S2.11. Left: Absorbance of AZB (black, 0.05 mM) and NR (red, 0.01 mM) demonstrating that AZB does not absorb at 575 nm where NR absorbance is monitored for release studies (inset). Right: Release of NR (%) in the dark (black) and under irradiation with 1000 W light (red).

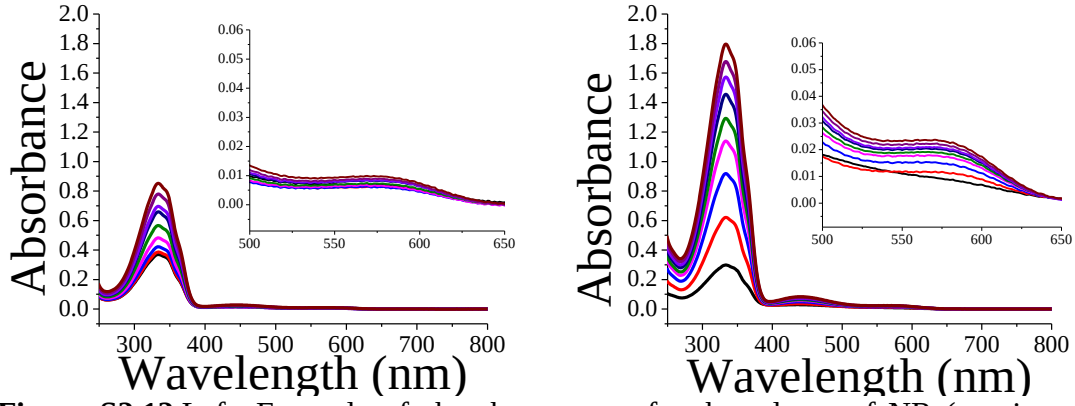

Figure S2.12.Left: Example of absorbance scansfor the release of NR (monitored at 575 nm, inset) under dark conditions (black, 30 min; red, 1 h; blue, 2 h; magenta, 3 h; green, 4 h; indigo, 5 h; light purple, 6 h; dark purple, 7 h; maroon, 8 h). Right: Example of absorbance scans for the release of NR (monitored at 575 nm, inset) under irradiation with 1000 W white light (black, 5 min; red, 1 h; blue, 2 h; magenta, 3 h; green, 4 h; indigo, 5 h; light purple, 6 h; dark purple, 7 h; maroon, 8 h).

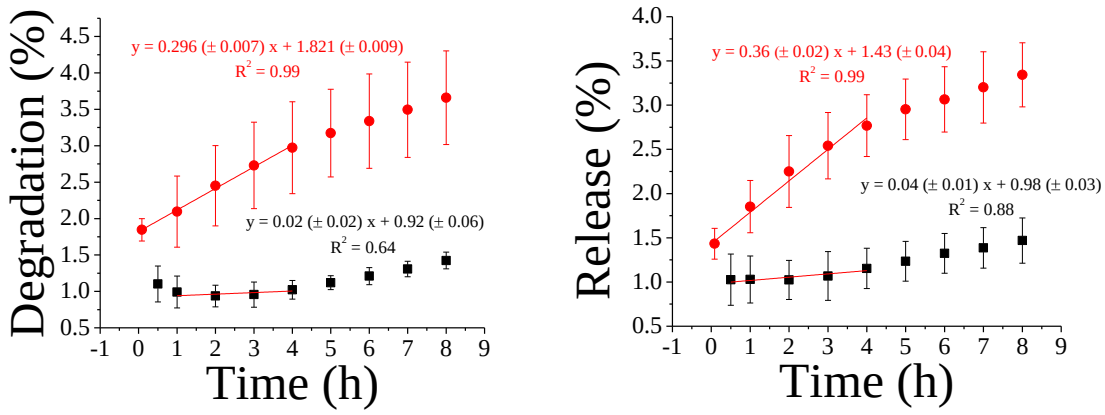

Figure S2.13. Left: Degradation (%, measured at 392 nm from the absorbance scans above) as a function of time in the dark (black squares) and under irradiation with 1000 W white light (red circles). The initial rates of degradation have been fitted to a linear profile to estimate how the material would behave in continuous flow conditions. Right: NR release (%, measured at 575 nm from the absorbance scans above) as a function of time in the dark (black squares) and under irradiation with 1000 W white light (red circles).

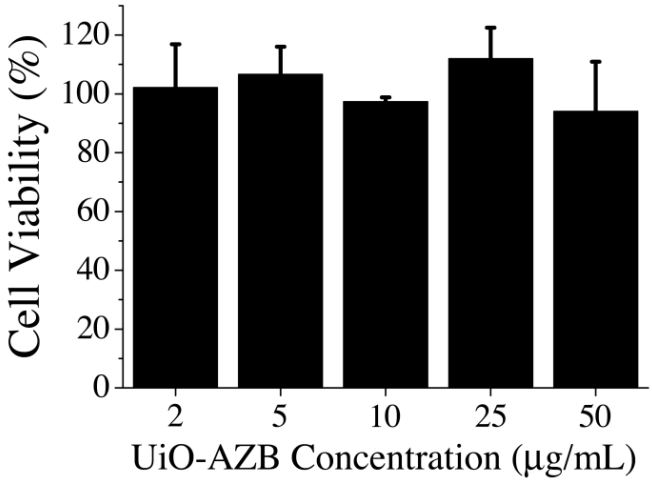

Figure S2.14. *In vitro* cytotoxicity of UiO-AZB against HeLa cells at different concentrations of UiO-AZB. Untreated cells were used as a control. Each data point is the average of three independent experiments.

3. Characterizing Defects in a UiO-AZB Metal-Organic Framework

This chapter has been prepared for publication by C.C. Epley, M. D. Love, and A.J. Morris.

3.1 Abstract

Exploring defect sites in metal-organic framework materials has quickly become an interesting topic of discussion in the literature. With reports of the enhancement of material properties with increasing defect sites, we were interested in probing the defect nature of UiO-AZB (UiO = University of Oslo, AZB = 4,4´-azobenzenedicarboxylate) nanoparticles. In this report, we investigate the use of acetic, formic, and benzoic acids as the modulators to prepare UiO-AZB. The results of H^1 NMR techniques and BET surface area analysis to elucidate the extent of defects in our samples are provided along with detailed discussions of the experimental trends. Although benzoic acid samples resulted in the most missing linkers per $Zr_6O_4(OH)_4$ cluster (as high as ~4), the increase in benzoic acid concentration drastically reduced the accessible SA from 2682 m^2/g to as low as 903 m^2/g, due to the creation of large macropores as the concentration of benzoic acid is increased. Overall, we found that using acetic acid as the modulator resulted in samples with the highest surface areas (2687 ± 218 m^2/g) and indentified a range of AA concentrations to produce nanoparticles from ~100-400 nm. These results highlight the best choice of modulator, found to be AA, to produce UiO-AZB nanoparticles with high surface areas.

3.2 Introduction

Metal-organic framework (MOF) research has flourished over the past several decades. MOFs are assemblies of metal clusters linked through multidentate organic

molecules and have been proposed for a variety of applications from gas storage/separation,[1-2] to toxin sequestration[3-5] and drug delivery.[6-8] Many structural motifs have been discovered and extensively characterized over the years; however, the crystalline nature of some MOFs renders them susceptible to bulk crystallographic defects, typically not distinguished with general single crystal diffraction. While defective materials may intuitively be considered undesirable, crystalline defects in MOFs have been shown to increase catalytic activity,[9-11] enhance conductivity,[12-13] and improve adsorption[14-16] of the bulk material. These material augmentations have led to increasing interest and debate regarding the essence of defects and the best approaches of how to control and quantify them, especially concerning the University of Oslo (UiO) series of MOFs.

UiO materials are specifically attractive due to the reports of exceptional chemical, thermal, and mechanical stability of UiO-66 (containing the 1,4-benzenedicarboxylate linker).[17] The use of "modulators" in the synthesis of UiO materials, to form octahedral $Zr_6O_4(OH)_4$ secondary building units (SBUs), renders these materials disposed to increased incidences of crystalline defects. Modulators serve not only to form the SBUs, but also to competitively bind with the chosen linker and direct MOF crystal growth. Therefore, in the final bulk material, the modulator may remain attached to the SBU, resulting in missing linkers. Additionally, it has been proposed that OH^-, H_2O, and Cl^- can also occupy missing linker sites.[10-11, 16, 18-20]

Several reports in the literature have attempted to describe the quantity of defect sites in bulk materials using various methods, mostly for UiO-66.[17, 21-26] Structural evidence quantifying missing linkers in UiO-66 came from a report by Zhou et al.,[26]

where they used neutron diffraction of samples synthesized with varying concentrations of acetic acid modulator. They reported an average of 1 in every 12 linkers to be missing, bringing network connectivity to 11 instead of the 12 expected for an ideal UiO-66 sample. Farha[10, 27] and co-workers indentified a maximum of 1.8 missing linkers for UiO-66 (Hf)[10] using titration techniques to evaluate defects in several UiO materials. Thermogravimetric analysis (TGA) is another technique reported to quantify defects in UiO-66[17, 22] and using this method, it has been shown that different batches of UiO-66 MOF prepared by a single synthesis can result in materials with drastically different degrees of missing linkers (up to 6 missing linkers per the 12 expected in an ideal UiO-66).[17] Finally, H^1 NMR techniques have also been used to elucidate the quantity of missing linker defects in UiO MOFs.[21-22] Samples are digested in a deuterated solvent and the integration corresponding to linker and modulator peaks present in the spectra are compared to find the modulator : linker ratio (discussed further in the results and discussion section). Using, this technique, Lillerud et al.[22] have reported ratios ranging from <0.1 to ~0.8 for UiO-66 materials synthesized using acetic acid and trifluoroacetic acid respectively. A value of 0.8 corresponds to an impressive 5 missing linkers per cluster and supports the assertion that UiO-66 can accommodate high levels of missing linkers. They were also able to demonstrate an increase in this ratio with increasing concentrations of modulator, indicating that higher levels of modulator used, resulted in more missing linkers under their synthetic conditions. For example, when formic acid concentrations were increased from 6 to 100 molar equivalents (mol modulator : mol Zr^{4+}), their integration ratios ranged from ~0.1 to 0.35.

Although the point vacancy defects (missing linkers and missing clusters) of UiO-

66 have been well documented, there are only a few reports addressing these defects for UiO materials with longer linkers.[10, 28-29] In fact, reports suggest that UiO-67, incorporating 1,4-biphenyldicarboxylate (BPDC), is not as stable as UiO-66 that incorporates 1,4-benzenedicarboxylate (BDC),[30-31] and this is likely due to increases in the defect nature of UiO-67 materials. It is also known that minor changes in the synthetic procedure (i.e. changing the concentration or identity of the modulator) can drastically alter the properties of the final bulk material.[17, 26] Therefore, we were interested in probing the defect nature of UiO-AZB (AZB = 4,4´-azobenzenedicarboxylate, Figure 3.1) nanoparticles.[32] We identified 3 different modulators appropriate to produce highly crystalline UiO-AZB materials: acetic (AA), formic (FA), and benzoic acids (BA) and explored a range of concentrations for each modulator: 30-70 molar equivalents for AA and FA, and 10-30 molar equivalents for BA. It was found that AA and FA gave materials with the highest surface areas (as high as 2982 and 2769 m^2/g, respectively). Despite having the lowest surface areas (as low as 903 m^2/g), the BA materials presented the highest levels of missing linkers. In this report, we provide the results of H^1 NMR analysis and N_2 adsorption isotherms to elucidate the extent of missing linkers in all samples generated using our synthetic procedure.

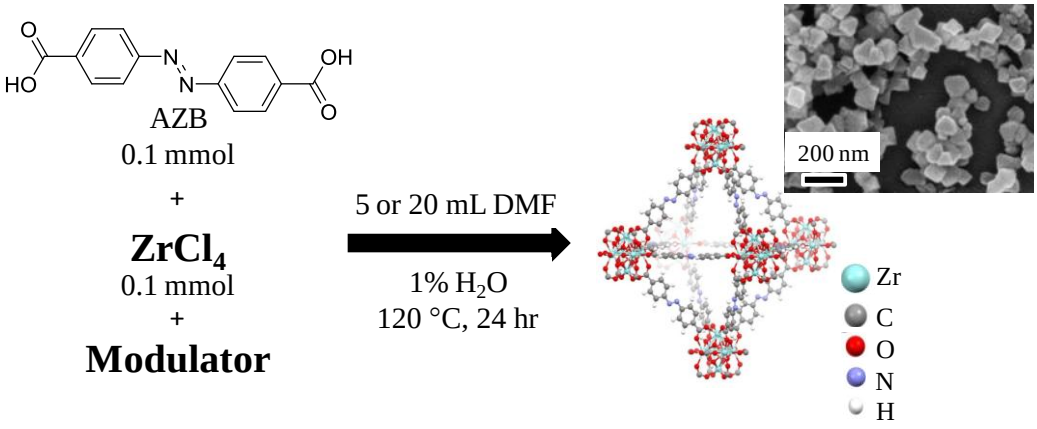

Figure 3.1. Representative diagram depicting the general synthetic conditions used. The octahedral cage on the right was generated using single crystal data from reference 30.

3.3 Experimental

3.3.1 Materials

The 4-nitrobenzoic acid (98 %), sodium hydroxide (≥ 98%), D-glucose (≥ 98 %), $ZrCl_4$ (anhydrous, 99.99 %), and benzoic acid (≥ 99.5 %) were purchased from Sigma Aldrich and used without further purification. Glacial acetic acid (certified ACS), formic acid (certified ACS) and dimethylformamide (DMF, Spectrophotometric grade ≥ 99.8 %) were used as received from Fisher Scientific.

3.3.2 Synthesis of 4,4´-azobenzenedicarboxylic acid (AZB)[33]

4-nitrobenzoic acid (13 g) and 250 mL of 5 M NaOH were heated to 50 °C in a 500 mL round bottom flask. An aqueous solution of 3.7 M D-glucose (150 mL) was added slowly (30 mL/min) to the flask with vigorous stirring. The reaction was allowed to stir for 10 minutes and then cooled to room temperature. The solution was aerated for 12 h and 5 M (200 mL) aqueous acetic acid was added to precipitate the AZB. The pink solid was collected via vacuum filtration and dried in a 100 °C oven for 18 h. (9.6 g, ~91 %) ^{1}H NMR (500 MHz, basic D_2O, δ, ppm) trans: 7.94, 7.92 (d, 2H, J= 10 Hz), 7.82, 7.80 (d, 2H, J = 10 Hz), cis: 7.68, 7.66 (d, 2H, J=10 Hz), 6.91, 6.89 (d, 2H, J = 10 Hz), (Predicted *m/z* = 270.2; $M\text{-}H^-$ = 269 *m/z*).

3.3.3 Synthesis of UiO-AZB nanoparticles

UiO-AZB materials were made by a procedure previously reported by our group.[32] AA (30-70 equivalents), FA (30-70 equivalents), and BA (10-30 equivalents) as the modulators in the synthesis were explored. The general procedure consisted of adding 0.0233 g $ZrCl_4$ (0.1 mmol), 0.0270 g H_2AZB (0.1 mmol), 5 mL DMF (20 mL when benzoic acid was the modulator),

10 μL H_2O, and the appropriate equivalents of modulator (x mol mod. : 1 mol Zr^{4+}) to a glass vial. The mixture was sonicated for ~1 min and then placed into a 120 °C oven for 24 h. The material was collected via centrifugation and washed with DMF. All materials were then flushed of DMF solvent by soaking in EtOH with fresh EtOH replacement every hour. A total of 5 EtOH soaking cycles were performed. Materials were then evacuated in a vacuum oven at 50 °C for 24 h. Evacuations at temperatures beyond this resulted in loss of crystallinity.

3.3.4 Powder X-ray Diffraction (PXRD)

For X-ray diffraction analysis, a 600 W Rigaku MiniFlex powder diffractometer operating with a Cu (K_α = 0.15418 nm) radiation source was used, with asweeping range of 3-50° in continuous scanning mode. Data was collected in 0.1° increments at a scanning rate of 1°/min, and patterns were generated with PDXL software.

3.3.5 Scanning Electron Microscopy (SEM)

A Leo (Zeiss) 1550 field-emission scanning electron microscope, equipped with an in-lens detector and operating at 5.0 kV, was used to collect SEM images. NPs were prepared for SEM imaging by first dispersing them in ethanol (0.1 mg/mL) via sonication. The resulting solution was then deposited via drop casting, with a short stem Pasteur pipette (1 drop), onto precut 5 mm x 5 mm glass slides. After room temperature drying, slides were mounted onto an SEM sample peg using double sided Cu tape and the sides of the slides were painted with conductive carbon paint. A Cressington 208 High Resolution Sputter Coater with a Au/Pd target (80/20) was used to deposit a conductive layer on the surface of the slides in order to allow for imaging. Samples were coated for 60 seconds.

3.3.6 Thermogravimetric Analysis (TGA)

A Q-series TGA from TA instruments was used to analyze thermal stability of materials. 10 mg of sample in a high temperature platinum pan were heated under air from 25 °C up to 1000 °C with a heating rate of 10 °C/min.

3.3.7 Gas Sorption Isotherms

The N_2 sorption isotherm measurements were collected on a Quantachrome Autosorb-1 at 77 K. The samples were placed in a 6 mm large bulb sample cell, which was degassed under vacuum for 24 h at room temperature. The surface areas of the materials were determined by fitting the adsorption data within the P/P_0 pressure range appropriate to the BET equation, ensuring that the y-intercept of the linear BET plot was positive.

3.3.8 H^1 Nuclear Magnetic Resonance

H^1 NMR measurements were made using an Agilent U4-DD2 400 MHz NMR with a 96 sample robot. Samples were prepared for NMR by digesting ~1.0 mg in 600 μL 50 mM Na_2HPO_4 in D_2O via sonication for 1 h. 50 μL of an 8 mM 3-(trimethylsilyl)propionic-2,2,3,3-d_4 acid sodium salt (TMSP) standard was added to each sample and the sample was transferred to an NMR tube for analysis.

3.4 Results and Discussion

We chose to investigate the addition of 3 different monocarboxylate modulators (AA, FA, and BA) with varying concentrations of each. The optimum concentration ranges for AA and FA was found to be 30-70 equivalents, and 10-30 equivalents for BA. Varying the concentration of the modulator has been shown to control particle sizes,[30, 34] where an increase in

modulator concentration typically results in larger particles. This is explained by faster MOF nucleation at lower concentrations of modulator, therefore reducing crystal growth and resulting in smaller particles. Indeed, upon increasing the modulator concentration, particle sizes increased as evidenced by SEM (Figure 3.2). We originally attempted to synthesize UiO-AZB without adding a modulator but were not able to obtain a crystalline product, evidenced by broadened amorphous features in the powder X-ray diffraction (PXRD) patterns of these syntheses. The PXRD patterns obtained for all modulated samples matched single crystal data reported in the literature[35] (Figure S3.1), confirming that the modulators used produced bulk materials isostructural with the reported UiO-AZB.

With conformation of crystalline samples, the focus became quantifying the defect nature of the materials. Therefore, we evaluated H^1 NMR spectra and N_2 adsorption isotherms in order to elucidate the extent of missing linker defects in our UiO-AZB materials. Due to the presence of the azo group in the linker, we felt that the possibility of linker protonation may interfere with the acid-base titration method and so, that technique was not explored in this study. Also, we were not able to effectively use TGA to evaluate defects due to a consistent gradual loss in the TGA curve below ~440 °C (Figure S3.2) and therefore, no clear plateau region in this range. This specific complication with TGA defect analysis was highlighted by Farha and co-workers.[10]

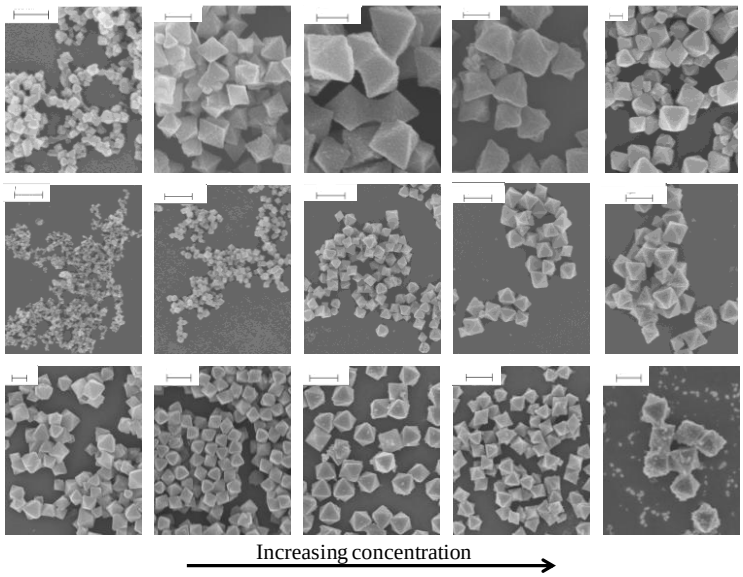

Figure 3.2. Particles sizes determined from SEM images of materials synthesized using AA (top, scale bars are 200 nm), B) FA (middle, scale bars are 1 μm), and C) BA (bottom, scale bars are 1 μm except for 10 equivalents BA whose scale bar is 200 nm).

3.4.1 H^1 Nuclear Magnetic Resonance (H^1 NMR)

UiO MOFs are unstable in basic environments, and so, can be digested in these conditions for H^1 NMR analysis. This is a powerful tool for the quantitative investigation of missing linkers. Not only can it provide a precise concentration of linkers in solution when a known amount of sample is digested, it can also be used to deem whether missing linkers are replaced by modulator species. In the H^1 NMR spectra, the integration of signals is proportional to the number of protons responsible for the signal. When multiple species are present in solution (e.g. linker and modulator) the integrations of signals assigned to each species can be used to determine the relative amounts of the various components. Furthermore, the addition of a H^1 NMR standard allows for the determination of exact concentrations of compounds in solution. This technique has been utilized in the literature to investigate and quantify missing linker defects for UiO-66.[15, 22]

To obtain samples for H^1 NMR analysis, materials were digested in a 50 mM Na_2HPO_4 solution in D_2O (see supplemental information for detailed digestion procedure). We followed a technique reported by Lillerud[22] et al. using H^1 NMR to investigate missing linkers. By using the relative integrations of each component, we are able to calculate the modulator to AZB ratio (mod/AZB) using equation (1),

$$\left(\frac{I_{MOD}}{H_{MOD}}\right) * \left(\frac{H_{AZB}}{I_{AZB}}\right) = \frac{Mod}{AZB} \text{ ratio} \quad (1)$$

where, I_{MOD} is the summed integration of all the signals due to the modulator, H_{MOD} is the number of protons attributed to the modulator in solution, H_{AZB} is the number of protons corresponding to AZB (16 due to 8 for each isomer), and I_{AZB} is the summed integration of all signals due to AZB. This ratio can be used to quantify the extent of modulator that remains bound to the structure after synthesis, washing, and evacuation. For example, a ratio value of 1.0 would mean there are equal concentrations of modulator and AZB linker, signifying that 50 % of the linkers are missing per cluster (or 6 of the expected 12).

Figure 3.3 shows example H^1 NMR spectra for BA and AA samples. Spectra of the digested samples synthesized using BA displayed a doublet at 7.88 ppm, and 2 triplets at 7.56, and 7.48 ppm. The spectra of digested samples synthesized using AA display a singlet at 1.92 ppm. Samples synthesized using FA only had the FA peak at 8.46 ppm, already visible in the example spectra given, and so, we omitted an example of FA spectra for this reason. A FA spectrum is provided in the Supplemental Information (Figure S3.3). No soaking regime was able to fully wash DMF from our materials suggesting that the solvent is trapped in UiO-AZB. Due to the acid/base hydrolysis of DMF to formic

acid and dimethylamine, especially at elevated temperatures, the peak corresponding to the formate proton is visible in all spectra.

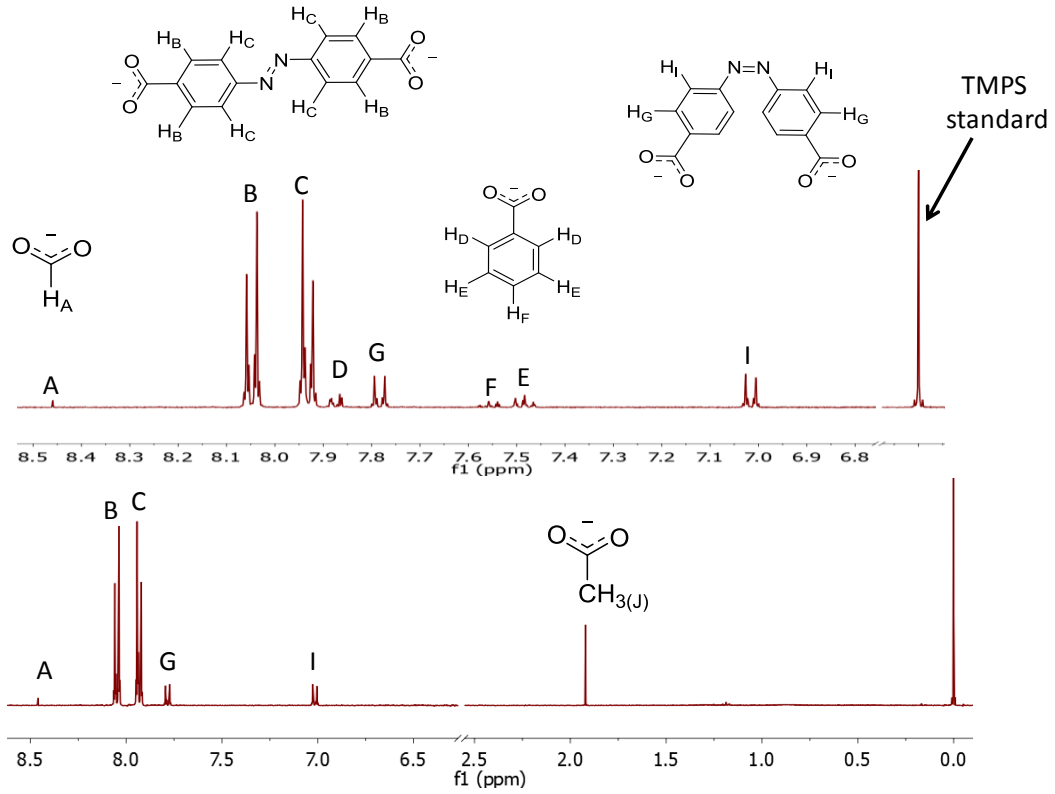

Figure 3.3. Top: Example spectrum of digested samples synthesized with BA. Bottom: Example spectrum of digested samples synthesized with AA.

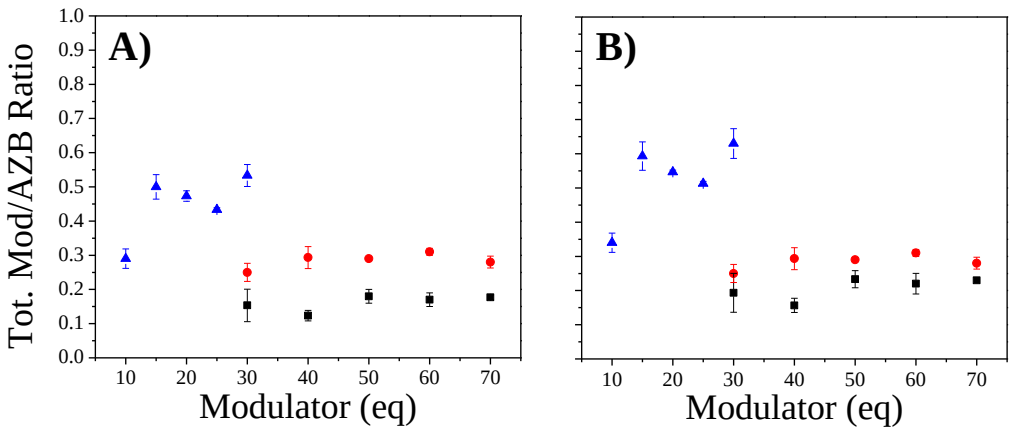

Figure 3.4. Total Modulator (Tot. Mod) to AZB ratio as a function of modulator concentration for samples synthesized using AA (black squares), FA (red circles), and BA (blue triangles) as the modulator.

To assess the total modulator to AZB ratio for all samples, the ratio was plotted as a function of modulator concentration. The question was how to approach the presence of formate in BA and AA samples. To address this, we calculated the ratio under two separate assumptions: 1) that the formate present is binding to the structure (Figure 3.4, A) such that it's integration must be included in the consideration of the mod/AZB ratio or 2) that it is not bound (Figure 3.4, B) and is the result of trapped DMF and therefore not included in the calculation. From the comparison of these two assumptions, we see that the assumption of trapped DMF results in values that are slightly higher for the AA and BA samples. Due to batch to batch variation, we could not correct for the trapped DMF in the spectra, and so we expected the ratio for the FA samples to be artificially high. Despite this obstacle, the overall trends are clear. First there seems to be no significant increase in the ratio with increasing concentrations of modulator for all samples, except in the case of 10 equivalents of BA, whose value was lower at ~0.3 than the rest of the BA samples. BA samples overall gave the highest ratios, up to ~0.5 for samples synthesized beyond 10 equivalents of BA. A ratio of 0.5 (1 BA unit per 2 AZB units) corresponds to 33 % of linkers missing or 4 of the 12 expected per cluster. The samples synthesized with AA display ratios at ~0.2, indicating 1 unit of modulator per 5 units of AZB or ~ 17 % of modulator remaining (2 missing linkers per cluster). The samples synthesized with FA show ratios of ~0.3, but again, we expected the FA ratios to be artificially high. A ratio of 0.3 corresponds to 23 % or roughly 3 missing linkers per cluster.

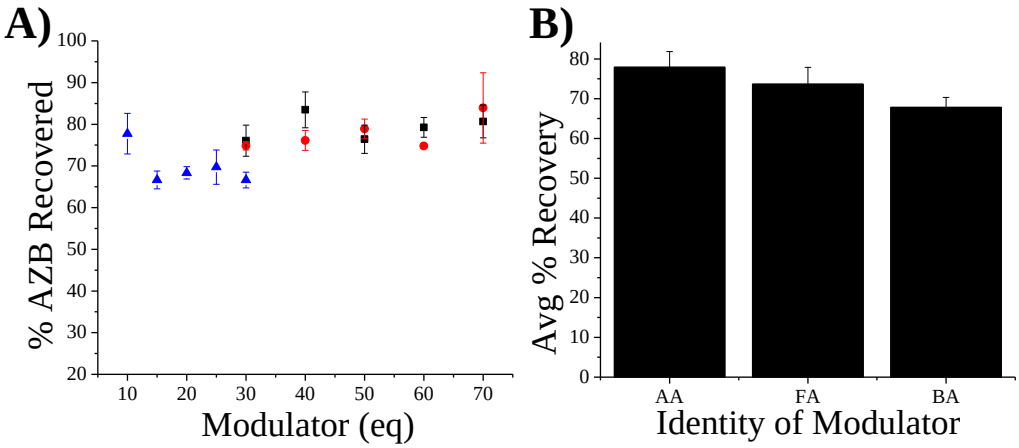

Figure 3.5. A)The % recovery of AZB calculated from H^1 NMR spectra according to equations (2-4) as a function of modulator equivalents for samples synthesized using AA (black squares), FA (red circles), and BA (blue triangles). B) Average % recovery of each modulator.

The issue of trapped DMF was circumvented by the addition of a 3-(trimethylsilyl)propionic-2,2,3,3-d_4 acid sodium salt (TMPS) standard to the samples. This allows us to calculate the AZB concentration in solution, independent of the presence of varying modulators. Knowing the concentration of the standard, the integration of standard signals and the integration of AZB signals can be used to calculate the concentration of AZB in solution, using equation (2). This gives an experimental value of AZB and by calculating the theoretical value of AZB based on the amount of sample digested; we can calculate a "% recovery" of AZB based on how much we expected from an "ideal" material with no missing linkers according to equations (3) and (4). In equation (2), [AZB] is the experimental concentration of AZB in solution, I_{AZB} is the summed integration from the signals attributed to both trans and cis-AZB, [S] is the concentration of the standard, and I_S is the integration of the signal from the standard (normalized to 9 in the case of TMPS).

$$[\mathrm{AZB}] = \frac{I_{AZB} * [S]}{I_S} \qquad (2)$$

In equation (3), mg_{UiOAZB} is the mass of material digested, $mol_{AZB\text{-}ideal}$ is the moles of AZB present in an ideal sample (6 mol AZB/1 mol UiOAZB), MW_{UiOAZB} is the molecular weight of ideal UiO-AZB = 2287.34 g/mol, V is the total volume of solution analyzed (650 µL in our case), and $Theo_{AZB}$ is the theoretical concentration of AZB expected for the sample assuming no missing linkers.

$$\frac{(mg_{UiOAZB})(mol_{AZB-ideal})}{(MW_{UiOAZB})(V)} = Theo_{AZB} \quad (3)$$

$$\frac{[AZB]}{Theo_{AZB}} * 100\ \% = \%\ \text{recovery} \quad (4)$$

Again, for all of the modulators (except 10 equivalents of BA), there did not seem to be a distinct difference in the average % recovery of AZB when the concentration of the modulators was increased (Figure 3.5, A). Therefore, we averaged all the % recovery values obtained for each modulator regardless of the concentration (Figure 3.5, B). For BA, we omitted the % recovery from the samples made with 10 equivalents. When comparing the modulators to each other (Figure 3.5, B), it is clear that overall, AA and FA samples had more AZB in solution, ~78 and 74 % recovery respectively. The BA samples made with 10 equivalents resulted in ~77 % recovery while those made with more than 10 equivalents gave ~68 % recovery. The results from the total modulator to AZB ratio (Figure 3.4) qualitatively agrees with the results of the % recovery calculation (Figure 3.5). For example, the mod/AZB ratio for BA samples above 10 equivalents was ~0.5. This value corresponds to 1 unit of modulator per 2 units of AZB, representing ~ 33% modulator and 67 % AZB or ~4 missing linkers per cluster. This correlates with the average % recovery calculated for BA samples beyond 10 equivalents (68 %), using a calculation method that ignores the BA signals in the H^1 NMR. The mod/AZB ratio of ~0.2 for AA correlates to 2 missing linkers per cluster or ~17 % AA and 83 % AZB. We were able to

recover 78% AZB on average for the AA samples. For FA samples, the mod/AZB ratio was ~0.3, corresponding to 1 unit of modulator to 3.3 units of AZB, or 23 % modulator and 77 % AZB. We recovered 74 % AZB for the FA samples. However, once again, the FA mod/AZB ratio is expected to be a slight overestimate due to trapped DMF in UiO-AZB materials. From the comparisons of these two techniques, we can make the determination that the modulator remaining is replacing AZB and is responsible for the lack of AZB in solution. Therefore, we postulated that in general there are ~4 missing linkers per cluster when BA above 10 equivalents (~3 when using 10 equivalents BA) is used as the modulator to make UiO-AZB and ~2 and ~3 when the modulator of choice is AA or FA, respectively.

3.4.2 N_2 adsorption isotherms

Gas sorption isotherms have been extensively used throughout MOF literature as a benchmark to provide insights into the porosity of frameworks. We measured N_2 isotherms for all of our samples and applied the BET theory to the appropriate pressure ranges governed by the criteria outlined in the literature.[36-38] All samples resulted in type II isotherms, and example isotherms for AA and BA are shown in Figure 3.6 (A and B respectively). Several reports indicate that increases in the modulator concentration result in an increase in gas uptake and thus the SA of UiO-66.[22, 26] This experimental evidence supports the logical hypothesis that increased modulator concentrations result in more defects that open more surface area for gas sorption. Of the samples investigated in this study, we did not observe this trend (Figure 3.6, C). We point out that in the case of UiO-66, there have only been two main types of defects suggested and evidenced in the literature: missing linker defects and missing clusters. In fact, drastic increases in SAs of

UiO-66 as more modulator is added have been attributed mainly to missing cluster defects.[22] Based on our PXRD patterns; we find no evidence of missing clusters. However, these reports only address the "point-like" vacancy defects characteristic of crystalline materials. During crystal growth, other crystal defects are possible including line and planar imperfections. For example, Siperstein[25] and co-workers show that decreasing CO_2 uptake can be attributed to pore blockage defects in $Cu_3(BTC)_2$ (BTC = 1,3,5-benzenetricarboxylate). These types of defects may arise from pockets of trapped solvent or as a result of crystal growth around synthetic byproducts (such as ZrO_2). The same MOF has also been shown to contain plane slipping defects[39] and crystal fractures[40] that can result from post-synthetic activation treatments. Furthermore, systematic experimental SA analyses, and how SA changes as more modulator is added, have not been conducted for UiO materials with longer linkers than UiO-66 incorporating BDC.

Type II isotherms are indicative of mesoporous or macroporous materials. Although, they can be observed in the case of non-porous materials, the fact that large volumes of gas are taken up rules out non-porous samples. In the low pressure region of the isotherm, the formation of a monolayer of N_2 is occurring on the adsorption sites of the framework "walls". At higher pressures, once the monolayer has formed, adsorption becomes dominated by pore filling and the sharp rise in the isotherm at relative pressures near unity indicates unrestricted adsorption where saturation of the pores is taking place.[41] In the case of a sample with large mesopores (2-50 nm pore widths) and macropores (> 50 nm), the surface area decreases compared to a microporous (< 2 nm) sample of the same framework, because the "walls" for gas sorption are absent in these large cavities. However, the void volume should increase as these pores become larger or more

abundant. The introduction of meso/macroporosity in our samples explains why we observe lower surface areas than the theoretical SA of the fully intact structure, which was found to be 3352 m^2/g (see supplemental information for calculation parameters).

Overall, AA samples gave the highest SAs and so, we conducted several trials to evaluate the batch variation of AA over the concentration range. It seems that all AA materials gave SAs within error of each other and therefore we conclude that the SA and porosity does not depend on the concentration of modulator for AA in the range from 30-70 equivalents. When all results were averaged, the SA for AA materials was 2687 ± 218 m^2/g (~10 % batch variation), with average pore widths of ~30 ± 12 Å.

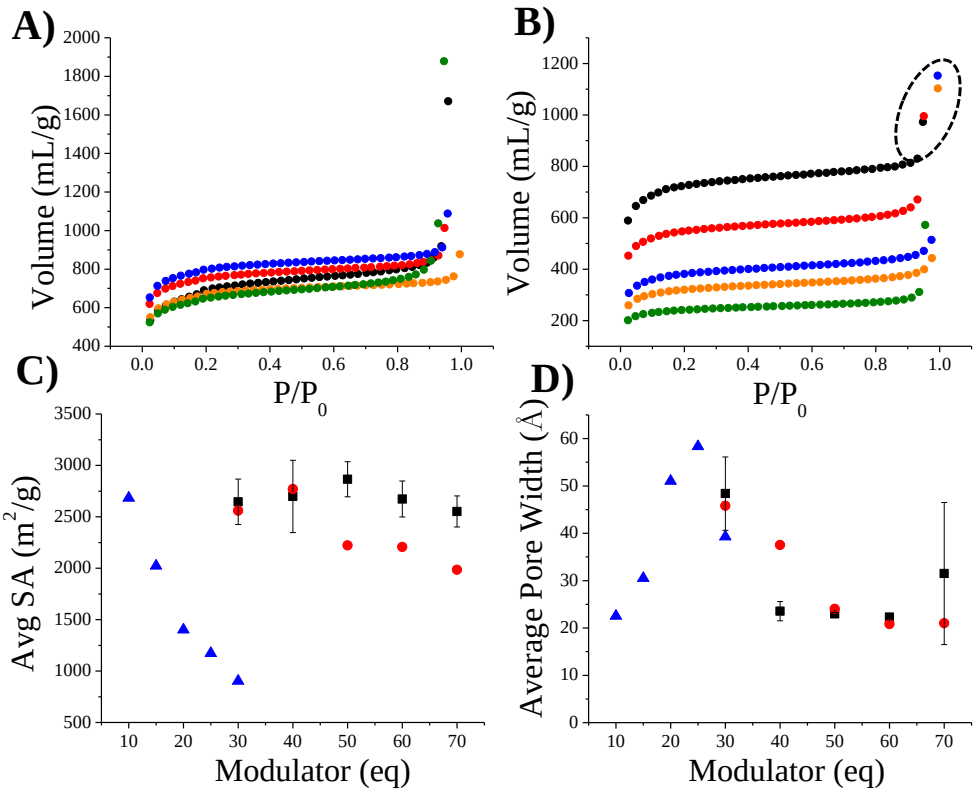

Figure 3.6. A) N_2 isotherms for materials synthesized with 30 eq. (black), 40 eq. (red), 50 eq. (blue), 60 eq. (orange), 70 eq. (green) AA. B) N_2 isotherms for materials synthesized with 10 eq. (black), 15 eq. (red), 20 eq. (blue), 25 eq. (orange), 30 eq. (green) BA. C) SA of materials synthesized with AA (black squares), FA (red circles), and BA (blue

triangles). D) Average pore width for AA (black squares), FA (red circles), and BA (blue triangles) as a function of modulator concentration.

BA and FA gave the most interesting results that showed opposite trends for the SA than have been observed in the literature for UiO-66 (Figure 3.6, C). FA resulted in SAs that increased from 2559 m^2/g at 30 equivalents FA to 2769 m^2/g with 40 equivalents however, above 40 equivalents, the SA dropped as low as 1985 m^2/g with 70 equivalents FA. When the lowest amount of BA was used, we observed a SA of 2682 m^2/g which consistently fell to 903 m^2/g when the BA concentration was increased from 10 to 30 equivalents. We noticed however, that the total uptake of N_2 increased with increasing amounts of BA up to 25 equivalents (dotted circle Figure 3.6, B), which pointed to increasing porosity. The Barrett-Joyner-Halenda method was then used to determine average pore widths for the FA and BA samples (Figure 3.6, D). For the FA samples, the pore width is decreasing as the concentration of FA increases. If no other factors are playing a role, the SA should therefore increase. However, we observe a decrease in the SA above 40 equivalents FA, indicating that other aspects of the defectivity should be considered other than the pore width. From the H^1 NMR analysis, it is clear that in the case of FA, the concentration of modulator does not affect the mod/AZB ratio and therefore, does not serve to introduce the occurrence of more defects. However, we see that increasing the FA concentration does affect the porosity of UiO-AZB, evidenced by a decrease in the SA and pore width. This means that at higher concentrations of FA, the total void volume decreases which points to increasing pore blockage defects. These pore blockages are not due to more trapped solvent, because the amount of solvent in the H^1 NMR spectra are not significantly different as the concentration of modulator is

increased. However, they could be due to more ZrO_2 being produced at higher concentrations of FA, resulting in crystal growth around these contaminates or samples that become more polluted with the inseparable byproduct.

For BA samples, when the concentration of BA is raised, the pore width drastically increases up to ~60 Å at 25 equivalents. Therefore, the drop in the BET SA is a result of large pores being generated in the BA samples as the concentration of BA is raised. This was a surprising result so we rationalized how this may occur. From H^1 NMR analysis, we see that when the concentration of BA is raised beyond 10 equivalents, the number of missing linkers per cluster increases from ~3 to ~4. In a report by Coudert and co-workers,[28] where they model several possible defect scenarios and simulate the CO_2 uptake of the resulting "three-site model" (assumed to be three linked clusters that posses the defect of interest), they point out that two missing linkers on a UiO SBU cluster can either be linear or not (i.e. adjacent or not). The orientation of missing linkers that are replaced by modulator species becomes more complex as the number of missing linkers per cluster is increased. For example, imagine a fully decorated cluster (Figure 3.7, top). If 4 missing linkers are placed the furthest apart from one another (Figure 3.7, bottom left), then crystal growth can proceed in all directions. However, if the 4 missing linkers are all coplanar (Figure 3.7, bottom right), a whole face of the cluster is restricted from crystal growth. This restriction allows for nano-regions of crystal inhibition and results in the formation of large vacant pockets in the final material. Due to π-π stacking and known dimer formation of BA, increasing the concentration of BA causes these vacancies to become larger and therefore increases the average pore spaces in the bulk samples.

In summary, using AA as the modulator was found to result in ~2 missing linkers per cluster and increasing the concentration of AA had no effect on the porosity of the samples. However, in the case of FA, with ~3 missing linkers per cluster, the average pore width decreases with increasing concentration as does the SA. This suggests that increasing the FA concentration either results in pore blockage defects or more inseparable byproducts that contaminate the samples, thus lowering the SA. When BA is increased beyond 10 equivalents, the number of missing linkers per cluster increases from ~3 to ~4, and increasing the BA concentration further results in large meso/macropores that serve to decrease the SA.

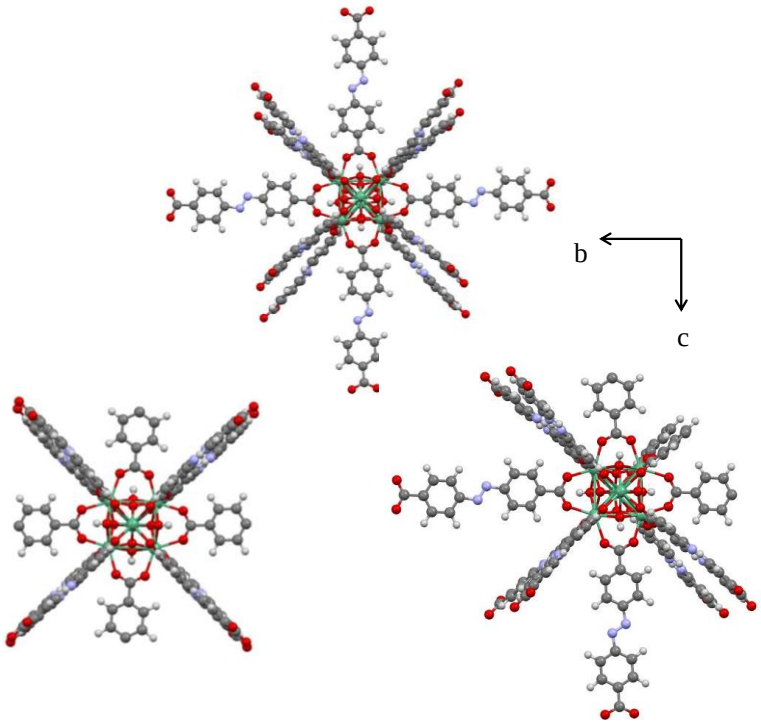

Figure 3.7. Diagram of missing linkers on a UiO-AZB cluster. Top: Fully decorated cluster. Bottom left: 4 missing clusters oriented 90° from the others. Bottom right: 4 missing clusters that are all coplanar. The colors represent: O (red), C (gray), N (blue), Zr (green), and H (white).

3.5 Conclusions

Although more work is needed to investigate the defect nature of MOF materials, practical application for determining the extent of missing linkers is necessary. Several factors are responsible for introducing missing linkers into framework structures. The use of modulators in the synthesis of UiO-AZB, results in the modulator remaining attached to the SBU and provides a way to tune the defect nature of these materials. The choice of modulator in these syntheses is crucial to the defect nature of the final products. Also, when adjusting synthetic conditions for any MOF synthesis, the properties of the bulk materials should be scrutinized.

The bulk products from our synthetic procedure were studied in order to attempt to quantify the defect nature of our samples. Missing linker analysis using H^1 NMR can be a powerful tool for the quantitative investigation of the defects in UiO MOFs, especially those with longer linkers that are challenging to grow as single crystals. It provides a quick technique that allows for the determination of the type of capping moiety that replaces missing linkers. Using this method, we were able to show that in the case of UiO-AZB, modulators used in the synthesis remain attached to the Zr_6 clusters. The use of BA as a modulator resulted in more missing linkers (~4 beyond 10 equivalents) when compared to samples made using AA and FA (~2 or 3, respectively). Analyzing the SA of these materials, we found that there was not a significant change in the SA when the concentration of the AA modulator was adjusted. However, samples made with above 40 equivalents of FA resulted in lower SAs. BA showed a decrease from 2682 to 903 m^2/g when the concentration was increased from 10 to 30 equivalents of BA, while the pore width increased suggesting increasing meso/macroporosity.

3.6 References

1. McDonald, T. M.; Lee, W. R.; Mason, J. A.; Wiers, B. M.; Hong, C. S.; Long, J. R., Capture of Carbon Dioxide from Air and Flue Gas in the Alkylamine-Appended Metal–Organic Framework Mmen- Mg2(Dobpdc). *Journal of the American Chemical Society* **2012,** *134* (16), 7056-7065.

2. Furukawa, H.; Cordova, K. E.; O'Keeffe, M.; Yaghi, O. M., The Chemistry and Applications of Metal-Organic Frameworks. *Science* **2013,** *341* (6149).

3. Bobbitt, N. S.; Mendonca, M. L.; Howarth, A. J.; Islamoglu, T.; Hupp, J. T.; Farha, O. K.; Snurr, R. Q., Metal-Organic Frameworks for the Removal of Toxic Industrial Chemicals and Chemical Warfare Agents. *Chemical Society Reviews* **2017**.

4. Saleem, H.; Rafique, U.; Davies, R. P., Investigations on Post-Synthetically Modified Uio-66-Nh2 for the Adsorptive Removal of Heavy Metal Ions from Aqueous Solution. *Microporous and Mesoporous Materials* **2016,** *221*, 238-244.

5. Dias, E. M.; Petit, C., Towards the Use of Metal-Organic Frameworks for Water Reuse: A Review of the Recent Advances in the Field of Organic Pollutants Removal and Degradation and the Next Steps in the Field. *Journal of Materials Chemistry A* **2015,** *3* (45), 22484-22506.

6. He, C.; Liu, D.; Lin, W., Nanomedicine Applications of Hybrid Nanomaterials Built from Metal–Ligand Coordination Bonds: Nanoscale Metal–Organic Frameworks and Nanoscale Coordination Polymers. *Chemical Reviews* **2015,** *115* (19), 11079-11108.

7. Horcajada, P.; Gref, R.; Baati, T.; Allan, P. K.; Maurin, G.; Couvreur, P.; Férey, G.; Morris, R. E.; Serre, C., Metal–Organic Frameworks in Biomedicine. *Chemical Reviews* **2012,** *112* (2), 1232-1268.

8. Huxford, R. C.; Della Rocca, J.; Lin, W., Metal–Organic Frameworks as Potential Drug Carriers. *Current Opinion in Chemical Biology* **2010,** *14* (2), 262-268.

9. Vermoortele, F.; Ameloot, R.; Alaerts, L.; Matthessen, R.; Carlier, B.; Fernandez, E. V. R.; Gascon, J.; Kapteijn, F.; De Vos, D. E., Tuning the Catalytic Performance of Metal-Organic Frameworks in Fine Chemistry by Active Site Engineering. *Journal of Materials Chemistry* **2012,** *22* (20), 10313-10321.

10. Liu, Y.; Klet, R. C.; Hupp, J. T.; Farha, O., Probing the Correlations between the Defects in Metal-Organic Frameworks and Their Catalytic Activity by an Epoxide Ring-Opening Reaction. *Chemical Communications* **2016,** *52* (50), 7806-7809.

11. Vermoortele, F.; Bueken, B.; Le Bars, G.; Van de Voorde, B.; Vandichel, M.; Houthoofd, K.; Vimont, A.; Daturi, M.; Waroquier, M.; Van Speybroeck, V.; Kirschhock, C.; De Vos, D. E., Synthesis Modulation as a Tool to Increase the Catalytic Activity of Metal–Organic Frameworks: The Unique Case of Uio-66(Zr). *Journal of the American Chemical Society* **2013,** *135* (31), 11465-11468.

12. Montoro, C.; Ocón, P.; Zamora, F.; Navarro, J. A. R., Metal–Organic Frameworks Containing Missing-Linker Defects Leading to High Hydroxide-Ion Conductivity. *Chemistry – A European Journal* **2016,** *22* (5), 1646-1651.

13. Jared M. Taylor, S. D., Ryuichi Ikeda, and Hiroshi Kitagawa, Defect Control to Enhance Proton Conductivity in a Metal–Organic Framework. *Chemistry of Materials* **2015,** *27* (7), 2286-2289.

14. Liang, W.; Coghlan, C. J.; Ragon, F.; Rubio-Martinez, M.; D'Alessandro, D. M.; Babarao, R., Defect Engineering of Uio-66 for Co2 and H2o Uptake - a Combined Experimental and Simulation Study. *Dalton Transactions* **2016,** *45* (11), 4496-4500.

15. Wang, K.; Li, C.; Liang, Y.; Han, T.; Huang, H.; Yang, Q.; Liu, D.; Zhong, C., Rational Construction of Defects in a Metal–Organic Framework for Highly Efficient Adsorption and Separation of Dyes. *Chemical Engineering Journal* **2016,** *289*, 486-493.

16. Ghosh, P.; Colon, Y. J.; Snurr, R. Q., Water Adsorption in Uio-66: The Importance of Defects. *Chemical Communications* **2014,** *50* (77), 11329-11331.

17. Valenzano, L.; Civalleri, B.; Chavan, S.; Bordiga, S.; Nilsen, M. H.; Jakobsen, S.; Lillerud, K. P.; Lamberti, C., Disclosing the Complex Structure of Uio-66 Metal Organic Framework: A Synergic Combination of Experiment and Theory. *Chemistry of Materials* **2011,** *23* (7), 1700-1718.

18. Katz, M. J.; Brown, Z. J.; Colon, Y. J.; Siu, P. W.; Scheidt, K. A.; Snurr, R. Q.; Hupp, J. T.; Farha, O. K., A Facile Synthesis of Uio-66, Uio-67 and Their Derivatives. *Chemical Communications* **2013,** *49* (82), 9449-9451.

19. Ling, S.; Slater, B., Dynamic Acidity in Defective Uio-66. *Chemical Science* **2016,** *7* (7), 4706-4712.

20. Vandichel, M.; Hajek, J.; Vermoortele, F.; Waroquier, M.; De Vos, D. E.; Van Speybroeck, V., Active Site Engineering in Uio-66 Type Metal-Organic Frameworks by Intentional Creation of Defects: A Theoretical Rationalization. *CrystEngComm* **2015,** *17* (2), 395-406.

21. Gutov, O. V.; Hevia, M. G.; Escudero-Adán, E. C.; Shafir, A., Metal–Organic Framework (Mof) Defects under Control: Insights into the Missing Linker Sites and Their Implication in the Reactivity of Zirconium-Based Frameworks. *Inorganic Chemistry* **2015,** *54* (17), 8396-8400.

22. Shearer, G. C.; Chavan, S.; Bordiga, S.; Svelle, S.; Olsbye, U.; Lillerud, K. P., Defect Engineering: Tuning the Porosity and Composition of the Metal–Organic Framework Uio-66 Via Modulated Synthesis. *Chemistry of Materials* **2016,** *28* (11), 3749-3761.

23. Lee, S. J.; Doussot, C.; Baux, A.; Liu, L.; Jameson, G. B.; Richardson, C.; Pak, J. J.; Trousselet, F.; Coudert, F.-X.; Telfer, S. G., Multicomponent Metal–Organic Frameworks as Defect-Tolerant Materials. *Chemistry of Materials* **2016,** *28* (1), 368-375.

24. Hu, Z.; Castano, I.; Wang, S.; Wang, Y.; Peng, Y.; Qian, Y.; Chi, C.; Wang, X.; Zhao, D., Modulator Effects on the Water-Based Synthesis of Zr/Hf Metal–Organic Frameworks: Quantitative Relationship Studies between Modulator, Synthetic Condition, and Performance. *Crystal Growth & Design* **2016,** *16* (4), 2295-2301.

25. Al-Janabi, N.; Fan, X.; Siperstein, F. R., Assessment of Mof's Quality: Quantifying Defect Content in Crystalline Porous Materials. *The Journal of Physical Chemistry Letters* **2016,** *7* (8), 1490-1494.

26. Wu, H.; Chua, Y. S.; Krungleviciute, V.; Tyagi, M.; Chen, P.; Yildirim, T.; Zhou, W., Unusual and Highly Tunable Missing-Linker Defects in Zirconium Metal–Organic Framework Uio-66 and Their Important Effects on Gas Adsorption. *Journal of the American Chemical Society* **2013,** *135* (28), 10525-10532.

27. Klet, R. C.; Liu, Y.; Wang, T. C.; Hupp, J. T.; Farha, O. K., Evaluation of Bronsted Acidity and Proton Topology in Zr- and Hf-Based Metal-Organic Frameworks Using Potentiometric Acid-Base Titration. *Journal of Materials Chemistry A* **2016,** *4* (4), 1479-1485.

28. Thornton, A. W.; Babarao, R.; Jain, A.; Trousselet, F.; Coudert, F. X., Defects in Metal-Organic Frameworks: A Compromise between Adsorption and Stability? *Dalton Transactions* **2016,** *45* (10), 4352-4359.

29. Cliffe, M. J.; Castillo-Martínez, E.; Wu, Y.; Lee, J.; Forse, A. C.; Firth, F. C. N.; Moghadam, P. Z.; Fairen-Jimenez, D.; Gaultois, M. W.; Hill, J. A.; Magdysyuk, O. V.; Slater, B.; Goodwin, A. L.; Grey, C. P., Metal–Organic Nanosheets Formed Via Defect-Mediated Transformation of a Hafnium Metal–Organic Framework. *Journal of the American Chemical Society* **2017,** *139* (15), 5397-5404.

30. Schaate, A.; Roy, P.; Godt, A.; Lippke, J.; Waltz, F.; Wiebcke, M.; Behrens, P., Modulated Synthesis of Zr-Based Metal–Organic Frameworks: From Nano to Single Crystals. *Chemistry – A European Journal* **2011,** *17* (24), 6643-6651.

31. DeCoste, J. B.; Peterson, G. W.; Jasuja, H.; Glover, T. G.; Huang, Y.-g.; Walton, K. S., Stability and Degradation Mechanisms of Metal-Organic Frameworks Containing the Zr6o4(Oh)4 Secondary Building Unit. *Journal of Materials Chemistry A* **2013,** *1* (18), 5642-5650.

32. Epley, C. C.; Roth, K. L.; Lin, S.; Ahrenholtz, S. R.; Grove, T. Z.; Morris, A. J., Cargo Delivery on Demand from Photodegradable Mof Nano-Cages. *Dalton Transactions* **2017,** *46* (15), 4917-4922.

33. Mary, L. J. F.; Kannan, P., Synthesis, Characterization and Thermal Behaviour of Poly(Pyromellitimide-Ester)S and (Imide-Urethane)S Containing Azobenzene Units. *European Polymer Journal* **1998,** *35* (1), 17-26.

34. Düren, T.; Millange, F.; Férey, G.; Walton, K. S.; Snurr, R. Q., Calculating Geometric Surface Areas as a Characterization Tool for Metal−Organic Frameworks. *The Journal of Physical Chemistry C* **2007,** *111* (42), 15350-15356.

35. Tsuruoka, T.; Furukawa, S.; Takashima, Y.; Yoshida, K.; Isoda, S.; Kitagawa, S., Nanoporous Nanorods Fabricated by Coordination Modulation and Oriented Attachment Growth. *Angewandte Chemie International Edition* **2009,** *48* (26), 4739-4743.

36. Schaate, A.; Dühnen, S.; Platz, G.; Lilienthal, S.; Schneider, A. M.; Behrens, P., A Novel Zr-Based Porous Coordination Polymer Containing Azobenzenedicarboxylate as a Linker. *European Journal of Inorganic Chemistry* **2012,** *2012* (5), 790-796.

37. Wang, T. C.; Bury, W.; Gómez-Gualdrón, D. A.; Vermeulen, N. A.; Mondloch, J. E.; Deria, P.; Zhang, K.; Moghadam, P. Z.; Sarjeant, A. A.; Snurr, R. Q.; Stoddart, J. F.; Hupp, J. T.; Farha, O. K., Ultrahigh Surface Area Zirconium Mofs and Insights into the Applicability of the Bet Theory. *Journal of the American Chemical Society* **2015,** *137* (10), 3585-3591.

38. Walton, K. S.; Snurr, R. Q., Applicability of the Bet Method for Determining Surface Areas of Microporous Metal−Organic Frameworks. *Journal of the American Chemical Society* **2007,** *129* (27), 8552-8556.

39. Ameloot, R.; Vermoortele, F.; Hofkens, J.; De Schryver, F. C.; De Vos, D. E.; Roeffaers, M. B. J., Three-Dimensional Visualization of Defects Formed During the Synthesis of Metal–Organic Frameworks: A Fluorescence Microscopy Study. *Angewandte Chemie International Edition* **2013,** *52* (1), 401-405.

40. Shoaee, M.; Agger, J. R.; Anderson, M. W.; Attfield, M. P., Crystal Form, Defects and Growth of the Metal Organic Framework Hkust-1 Revealed by Atomic Force Microscopy. *CrystEngComm* **2008,** *10* (6), 646-648.

41. Gómez-Gualdrón, D. A.; Moghadam, P. Z.; Hupp, J. T.; Farha, O. K.; Snurr, R. Q., Application of Consistency Criteria to Calculate Bet Areas of Micro- and Mesoporous Metal–Organic Frameworks. *Journal of the American Chemical Society* **2016,** *138* (1), 215-224.

3.7 Supporting Information

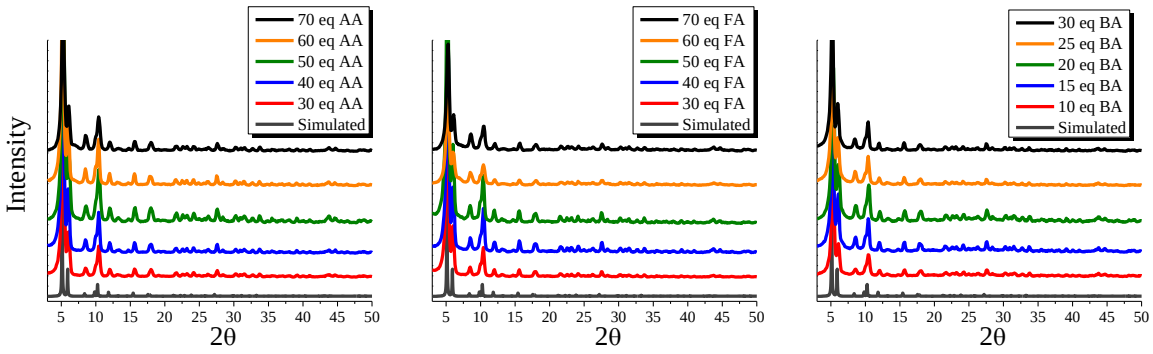

Figure S3.1. PXRD patterns of all materials.

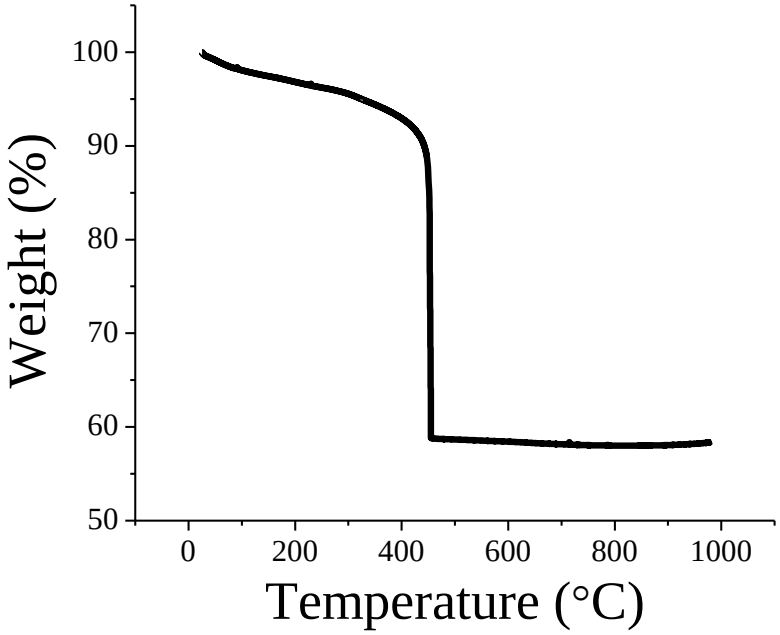

Figure S3.2. TGA examples of materials synthesized using AA, FA, and BA.

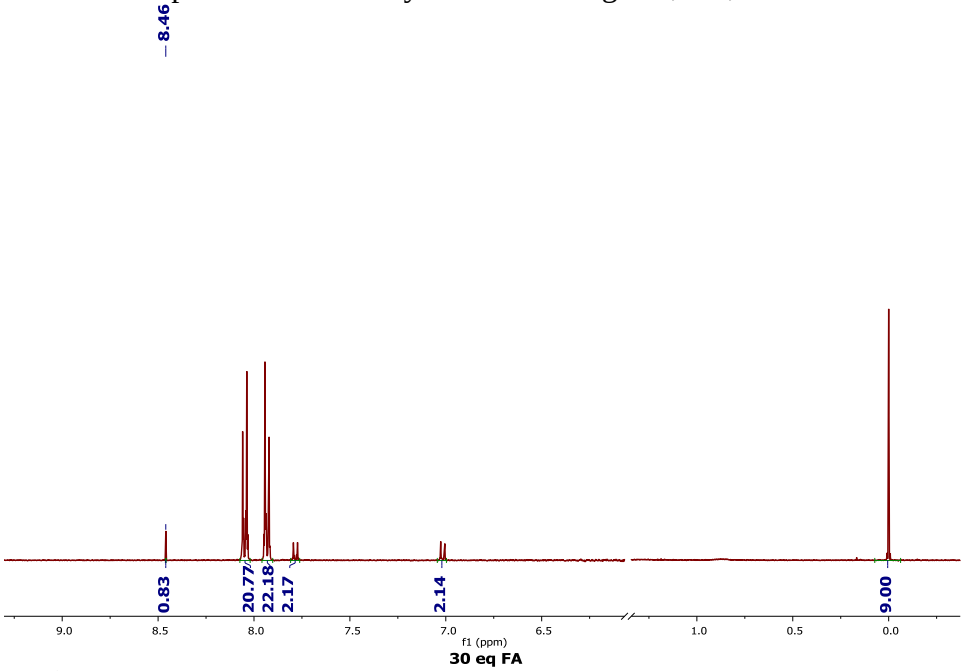

Figure S3.3. H^1 NMR of a FA sample.

4. Photo-triggered release of 5-fluorouracil from a MOF drug delivery system

This chapter has been prepared for publication in collaboration with C. C. Epley*, K. L. Roth*, M. Ashraf-Khorassani, M. L. McAndrew, J. J. Novak, A. J. Morris, and T. Z. Grove. *Authors contributed equally.

4.1 Abstract

Metal organic framework (MOF) nanocarriers offer advantages of high surface area and synthetic diversity that fosters interest in their potential for drug delivery applications. We have previously demonstrated that the incorporation of photo-isomerizable struts into the MOF scaffold allows for the development of stimuli-responsive drug delivery systems. To explore further, we were motivated to target cancer treatment using the core UiO-AZB nanoparticles stabilized by a surface coating of aminated polyethylene glycol (PEG-NH_2). Herein, we report the design and successful photo-triggered degradation of a PEG-NH_2 functionalized UiO-AZB nanoparticle loaded with 5-fluorouracil (15 wt%), referred to as PEGNH_2@5-FU-UiOAZB. The PEGNH_2@5-FU-UiOAZB nanoparticles are highly stable in biological conditions and undergo degradation and subsequent release of 5-FU upon irradiation with 340 nm light.

4.2 Introduction

Metal organic frameworks (MOFs) have shown value in many applications ranging from gas separation[1] to catalysis[2]. Although originally discovered in the late 1980's, it was not until 2006 when Horcajada et al. illustrated their use as possible drug delivery systems with remarkable loading capacities (up to 140 wt% for ibuprofen).[3] MOFs exhibit high surface areas (up to 7000 m^2/g)[4] and tunable pore sizes, both of which allow for unprecedented cargo loading,

making MOFs great candidates for drug delivery platforms.[5] MOFs have also been shown to encapsulate a wide variety of drug classes. For example, MIL-100 (MIL = Materials of Institute Lavoisier) has shown uptake of hydrophilic drug agents azidothymidine triphosphate (AZT-Tp), cidofovir (CDV), and sulisobenzone[6]; hydrophobic agents doxorubicin and oxybenzone; and the amphiphilic anticancer drug busulfan.[7] The fact that a single MOF exhibits appreciable uptake for a wide variety of drug types demonstrates the versatility of these systems as nanocarriers.

Obstacles with developing and implementing drug delivery systems come from the ability to secure cargos until they reach an active site and controllably release them when commanded. Having control over where nanocarriers go systemically and additional control of the release of therapeutic cargos, reduces toxicity of the overall system and decreases unwanted off target effects.[8] The primary approach to deliver nanoparticles (NPs) to a specific site for cancer therapy is through the enhanced permeability and retention (EPR) effect, where molecules of a certain size demonstrate greater accumulation in tumor tissues.[8] This is due to disorganized angiogenesis that results in vascular pores ranging from 100-780 nm[9] and therefore, circulation through tumors concentrates NPs in these tissues.[10] Once NPs have collected within the site of action, a stimulus can trigger the release of a therapeutic cargo, ensuring no release until the system enters the tumor. The use of external-stimuli, such as heat, light, or magnetic field, offer the advantages of spatial and temporal control over the use of internal or biological stimuli.[11]

Another important design feature to consider when developing a drug delivery system is the rate and mechanism by which they release drug cargos. A common method to design stimuli-responsive MOFs is to add a capping agent to the surface of the MOF that can control the release of the loaded cargo. This capping approach is demonstrated by Tan et al. where they utilize heat as an external-stimulus to trigger the release of 5-fluorouracil (5-FU) from pillarene capped UiO-

66 MOFs.[12] Cation exchange is another release mechanism where biologically relevant cations are used to trigger the controlled release of cargo. This competitive binding technique was first shown using Na^+ as a trigger to release procainamide from a zinc-adeninate MOF[13], and latter combined with the capping method when Zn^{2+} binds to the capping pillarenes implanted on a UiO-66 MOF to achieve up to ~70 % release of 5-FU within an hour.[12] A third mechanism for stimuli-responsive drug release is through a controlled dissolution of the material and subsequent release of the loaded cargo. Sun et al. demonstrates pH triggered degradation of ZIF-8 by introducing the system to acidic conditions, resulting in sustained release of 5-FU over 7 days.[5]

The future of personalized cancer care relies in part on the discovery of targeted treatment methods to alleviate the systemic side effects of traditional chemotherapeutics. Photodynamic therapy (PDT) has been proposed as an effective method for the selective targeting of cancer tumors with light as an external-stimulus. Traditional PDT operates via an oxygen-dependent mechanism. Upon irradiation with light, a photosensitizer promoted to an excited state reacts with the oxygen naturally present in tissues to generate $^1O_2$. However, rapidly growing tumors often deplete the blood's supply of oxygen leaving parts of tumors with dramatically decreased oxygen levels compared to healthy tissue.[14] Therefore, patients with solid tumors containing a large fraction of hypoxic cells are ineffectively treated with traditional PDT, leaving surgery and systemic chemotherapy as the best treatment option. For PDT to play the primary clinical role in the treatment of cancers, a new paradigm for the utilization of light in targeted therapies must be developed. The development of small molecule O_2-independent PDT agents is a major goal of the field.[15-17]

In this work, we discuss the design of a photo-degradable MOF drug delivery system where a photo-responsive linker, 4,4´-azobenzenedicarboxylate (AZB), is incorporated into the

backbone to give a UiO-type MOF referred to as UiO-AZB. AZB undergoes isomerization upon irradiation with light and, as previously shown,[18] results in degradation of the UiO-AZB nanocarriers. The cancer therapeutic, 5-FU, was loaded into the framework with a maximum of 14.9 wt% achieved after 3 days. In order to increase the aqueous stability, biocompatibility, and half-life of the system, an aminated polyethylene glycol (PEG-NH_2) coating was post-synthetically attached to give a material loaded with 5-FU, herein referred to as PEGNH_2@5-FU-UiOAZB. The system was irradiated with 340 nm light and photo-triggered degradation was monitored as a function of time. PEGNH_2@5-FU-UiOAZB was found to be stable in the dark and to degrade upon irradiation with 340 nm light. The light induced degradation provided a means to deliver the loaded 5-FU *in vitro,* and concentration dependent cell death was observed upon irradiation. This study highlights the scope and applicability of MOF drug delivery systems and emphasizes the germane need for investigation of these materials in biological applications.

4.3 Experimental

4.3.1 Synthesis of UiO-AZB nanoparticles

The synthesis described here was adapted from a previous report by changing the modulator to acetic acid at 30 equivalents to zirconium.[18-19] To a 20 mL vial, H_2AZB (0.0270 g, 0.1 mmol), $ZrCl_4$ (0.0234 g, 0.1 mmol), glacial acetic acid (172 μL, 3 mmol), and DMF (5 mL) were added and the solution sonicated for ~5 min to give a bright orange solution. The mixture was placed in a 120 °C oven for 24 h. While still warm, the contents of the vial were transferred to a 15 mL centrifuge tube and the particles collected via centrifugation (4,000 rpm for ~15 min). After decanting the supernatant, 5 mL fresh DMF was added and the particles redispersed with

sonication for 10 minutes. Particles were allowed to soak in the fresh DMF for 15-30 min. Particles were again collected via centrifugation and the supernatant decanted. This washing process was repeated for a total of 1 x 5 mL DMF and 5 x 5 mL EtOH. Upon removal of the final supernatant, the particles were dried in a vacuum oven at 50 °C for 24 h.

4.3.2 Synthesis of NH_2-PEG-NH_2 polymer

Commercial polyethylene glycol (PEG; M_n = 2,000 g/mol) was dried on a Dean-Stark trap for 1 hour in toluene. Excess toluene was refluxed off and 6 equivalents (1.77 g) of Fmoc-glycine, 6 equivalents (1.23 g) DCC (N,N'-Dicyclohexylcarbodiimide), and 0.2 equivalents (0.024 g) DMAP (4-Dimethylaminopyridine) were added to the mixture in DMF. After stirring at 24 °C for 12 h, the polymer mixture was precipitated in cold diethyl ether. The Fmoc group was removed by dissolving the collected polymer in 20% piperidine in DMF and stirring for 30 min. The diamine terminated PEG was precipitated in cold diethyl ether, collected through vacuum filtration, and dried in a vacuum oven overnight.

4.3.3 Synthesis of PEGNH_2@5-FU-UiOAZB

5-fluorouracil (400 mg) along with 150 mL EtOH, were added to a 200 mL round bottom flask. The solution was heated to 70 °C and allowed to stir until dissolved. After cooling, 200 mg UiO-AZB was then added to the solution and the flask was sonicated for ~30 min to form a cloudy orange suspension. The solution was allowed to stir vigorously. After 72 hours of vigorous stirring, a solution of 5.0664 g NH_2-PEG_{2k}-NH_2 in 50 mL EtOH was added to the flask and stirred for an additional 24 h. The coated 5-FU loaded nanoparticles, referred to as PEG-NH_2@5-FU-UiOAZB, were collected in 10 mL aliquots via centrifugation (in 2 x 15 mL centrifuge tubes), washed via centrifugation with 10 mL EtOH in each tube, then dried in a vacuum oven at 50 °C for 24 h.

4.3.4 ^{1}H nuclear magnetic resonance spectroscopy (NMR)

All NMR experiments were performed using an Agilent U4-DD2 (400 MHz) instrument. The PEG solutions were prepared in $CDCl_3$. The $PEGNH_2$@5-FU-UiOAZB digestion was prepared in 50 mM Na_2HPO_4 in D_2O.

4.3.5 Fourier Transform Infrared spectroscopy (FT-IR)

A Varian 670 FT-IR spectrometer with a diamond Specac Golden Gate attenuated total reflectance (ATR) attachment was used to collect infrared spectra. A background of air was collected and subtracted from each sample spectra. For both background and sample collection, 64 scans with a resolution of 4 cm^{-1} were obtained from 4000-400 cm^{-1}.

4.3.6 Thermogravimetric analysis (TGA)

A Q-series TGA from TA instruments was used to analyze thermal stability of materials. The samples (10 mg) were placed in aluminum pans and heated under nitrogen from 0 °C to 950 °C with a heating rate of 5 °C/min.

4.3.7 Transmission electron microscopy (TEM)

TEM images were obtained using a Philips EM 420 transmission electron microscope with an accelerating voltage of 120 kV. Samples were prepared by depositing 10 μL of UiO-AZB nanoparticles on a 300 mesh carbon coated copper grid (EM Science) and left to dry overnight.

4.3.8 Dynamic light scattering (DLS)

The size distribution of the NPs was measured using a Malvern Zetasizer Nano-ZS. $PEGNH_2$@5-FU-UiOAZB NPs were suspended in 50 mM disodium phosphate buffer (pH=7.6). Samples were sonicated for 60 minutes and passed through a 0.45 μm filter prior to measurement. For the fetal bovine serum (FBS) incubation the $PEGNH_2$@5-FU-UiOAZB NPs

(1 mg/mL) were incubated with 500 µL undiluted FBS (Life Technologies) for 2 hours at 37 °C under constant agitation. The NPs were centrifuged at 14,000 rpm for 20 min. The pellet was resuspended in water and washed two times by centrifuging at 14,000 rpm for 20 min. The final pellet was resuspened in 1 mL of DI water.

4.3.9 Degradation studies

A typical experiment consists of adding 10 mg $PEGNH_2$@5-FU-UiOAZB to a vial, along with 10 mL simulated cerebrospinal fluid (method in SI). The vial was sonicated for 30 seconds and incubated in the dark for 90 min. After incubation, the contents of the vial were either transferred to a well plate to be inserted into the LED array (340 nm, 53 mW) built in-house, or kept in the dark. 160 µL aliquots were removed every 30 min for 5 h, then every hour for a total of 12 h. Upon removal, each aliquot was centrifuged at 13,000 rpm for 5 min and the supernatant was collected for UV-Vis and HPLC analysis. The concentration of AZB in the resulting solution was calculated through the measured absorption at 392 nm, using the following equation.

$$\frac{Abs_t}{\varepsilon_{392\,nm}} = C_{AZB(E)} \qquad 1)$$

where Abs_t is the measured absorbance at 392 nm at time t, ε is the extinction coefficient of AZB, and $C_{AZB(E)}$ is the experimental concentration of AZB. As described previously[18] the percent degradation of the UiO-AZB MOF is determined by comparing the experimental ($C_{AZB(E)}$) and total ($C_{AZB(T)}$) concentration of AZB.

$$\frac{C_{AZB(E)}}{C_{AZB(T)}} \times\ 100\% = \%\ degradation \qquad 2)$$

where the total AZB concentration is determined using the equation below.

$$\frac{6m}{(MW_{UiO-AZB})V} = C_{AZB(T)} \quad (3)$$

where m is the mass of UiO-AZB, $MW_{UiO\text{-}AZB}$ is the molecular weight of 2,877.34 g/mol, and V is the added volume of simulated cerebrospinal fluid. The moles of AZB are then multiplied by the molar ratio of AZB to UiO-AZB (6:1).

An Agilent 1100 series HPLC equipped with a G1367A autosampler, quaternary pump, column heater set at 40°C and DAD detector set at 254 nm was used to measure the release of AZB. Separations were obtained through the C_{18}XBridge column (4.6 mm x 25 mm with 5μm spherical packing) using H_2O/ACN (85%:15%) as the isocratic elution solvent. The flow rate was set to 1 mL/min and each run was 6 min.

4.3.10 In vitro studies

MCF7 cells were seeded at 8,000 cells per well in a 96-well plate and cultured for 24 h at 37 °C and 5 % CO_2. Two plates were made for each concentration tested. Solutions of PEGNH_2@5-FU-UiOAZB (10, 50, 100, 500, 1000, 2000, 3000 μg/mL) in DMEM were added to the wells. After 1 h incubation one plate was placed on the bench top in the dark and one plate was placed in the LED array and irradiated for 30 min in 15 min intervals to prevent the temperature of the solution from rising. The plates were then incubated for 1 h before the media was removed and cells were washed three times with PBS. To each well 10 μL of 5 mg/mL MTT and 90 μL of DMEM were added and incubated at 37 °C. After 4 h the media was removed and the formazan crystals were dissolved in 100 μL DMSO. The absorbance at 570 nm was measured using a microplate reader. Percent viability of the cells was calculated as the ratio of mean absorbance of triplicate readings with respect to mean absorbance of control wells.

4.3.11 Cell Uptake studies

MCF7 cells were seeded at 8,000 cells per well in a 96-well plate and cultured for 24 h at 37 °C and 5 % CO_2. Solutions of $PEGNH_2$@5-FU-UiOAZB (0.1, 1, 3 mg/mL) in DMEM were added to the wells. After 1 h incubation the solutions were removed and cells were washed three times with PBS. The cells were removed with 100 μL of trypsin-EDTA (Thermo-Fisher). After a 10 min incubation, the solution was transferred to a glass vial and 1 mL of 0.1 % Triton-X-100 in a 1:1 sulfuric acid and nitric acid solution was added. After a 10 min incubation the solutions were diluted to 6 mL with DI water. Control cells without NPs were prepared as above. Total amounts of zirconium in the cells were determined by ICP-MS (Thermo Electron X-Series).

4.4 Results and Discussion

External-stimuli responsive nanomaterials are the next-generation of drug delivery systems.[11] Customization of physicochemical properties of the delivery platform along with control over the external stimulus offers the advantage of spatiotemporal control. The NP drug delivery system described in this report consists of a previously reported[18] MOF nanocarrier, UiO-AZB, loaded with 5-FU and surface functionalized with aminated PEG, PEG-NH_2. A maximum 5-FU loading of 14.9 wt% was achieved after 3 days of stirring in an ethanolic solution with a UiO-AZB : 5-FU ratio of 1 : 2. The subsequent attachment of the PEG-NH_2 enhances colloidal stability and offers resistance to degradation in biological media. Upon irradiation with light (340 nm), the AZB linkers isomerize resulting in photo-triggered degradation and 5-FU release (Scheme 4.1).

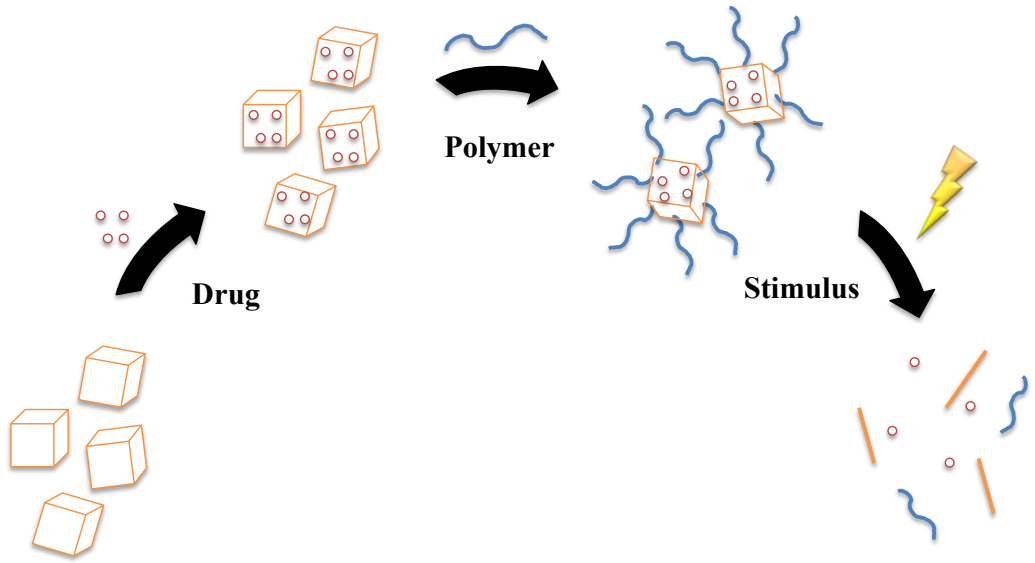

Scheme 4.1 Schematic illustration of the formation of the drug (red spheres) loaded and polymer (blue lines) coated UiO-AZB. The presence of the external stimulus triggers the degradation of the UiO-AZB and release of the drug is achieved.

4.4.1 NH_2-PEG_{2k}-NH_2 synthesis and characterization

PEG is widely used as a surface modification for drug delivery platforms, as it is water soluble, bio-inert, nontoxic, and extends the circulation time of the drug system in the blood stream.[20] Commercial PEG, with terminal alcohol groups, does not directly coordinate to the surface of the UiO-AZB NPs. In order to achieve coordination to the NP, as opposed to non-specific encapsulation, primary amine functional groups, which would interact with the zirconium metal nodes, were added to the PEG chains. Studies show that using a low molecular weight PEG with a high coating density better shields the NP from protein adsorption than using a high molecular weight polymer.[21] Therefore, we chose a low molecular weight PEG (2,000 M_n) for the surface coating of UiO-AZB. The primary amine functionality was added through coupling the carboxylic acid on Fmoc-glycine to the terminal alcohol using DCC coupling

(Scheme 4.2). The Fmoc group protecting the primary amine is removed with 20% piperidine in DMF. The resulting product is aminated PEG, NH_2-PEG_{2k}-NH_2.

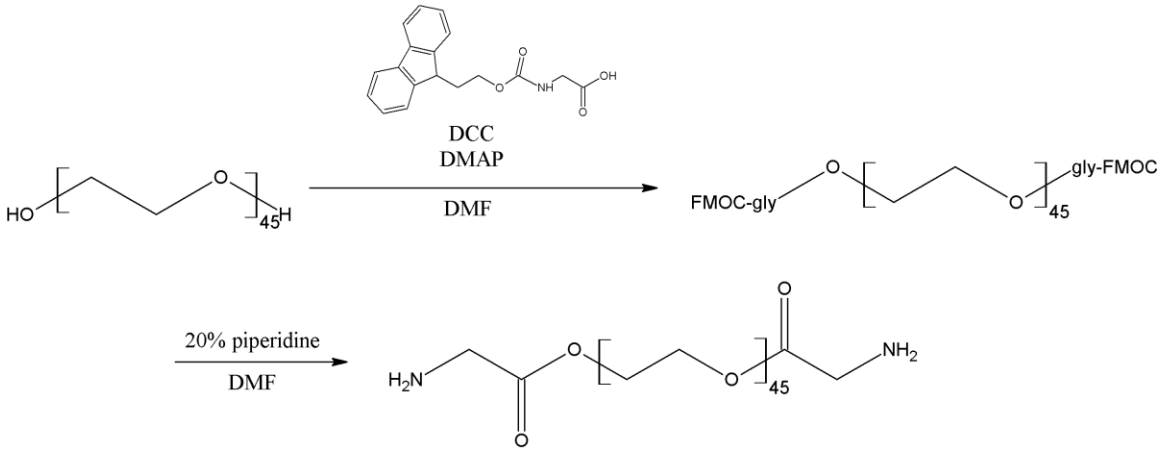

Scheme 4.2. The two-step synthesis of amine functionalized PEG. In the first step PEG is reacted with Fmoc-glycine-OH through DCC coupling. The Fmoc protecting group is then removed resulting in NH_2-PEG-NH_2.

Figure S4.1 shows the ^{1}H-NMR of aminated PEG. All ^{1}H-NMR samples were prepared in $CDCl_3$ (7.26 ppm) after polymer precipitation into diethyl ether (residual solvent peak at 3.48 ppm). There is no observable amine shift seen for NH_2-PEG_{2k}-NH_2, possibly due to overlap with the large PEG peak. Therefore, in order to quantify the percentage of final amination the Fmoc groups are quantified assuming a primary amine for every Fmoc group (Figure S4.1, A). Integrating to the known molecular weight of PEG allows for the percentage of Fmoc attachment to be determined as 92% end group conversion. The ^{1}H-NMR spectrum shows complete removal of the Fmoc group from the PEG, resulting in primary amine terminated PEG (Figure S4.1, B). The Kaiser test, a sensitive colorimetric assay that tests for the presence of primary amines, also confirms that removal of the Fmoc groups results in aminated PEG. In the absence of free primary amino groups the Kaiser test yields a light yellow color, seen in the Fmoc-PEG-Fmoc

sample (Figure S4.1, A). A deep blue color indicates the presence of primary amine groups, seen after the removal of the Fmoc protecting groups (Figure S4.1, B).

The FT-IR spectrum of H_2N-PEG-NH_2 (Figure 4.2, B, red) agrees with literature reports of PEG.[22] The characteristic C-H stretching frequencies at 2860 cm^{-1} and C-O stretch at 1460 cm^{-1} are seen. In addition, a C=O stretching peak at 1660 cm^{-1} is present due to the ester bond from the addition of the glycine group (Scheme 4.2). This reconfirms the successful attachment of the glycine group to the PEG terminus.

4.4.2 Synthesis of PEGNH_2@5-FU-UiOAZB

UiO-AZB NPs were made using a solvothermal procedure developed in our lab in which $ZrCl_4$, H_2AZB, acetic acid, and DMF are mixed in a vial and placed in a 120 °C oven for 24 h (see section 4.3.1 for the detailed synthetic procedure). The cancer drug 5-fluorouracil (5-FU) is used clinically to treat breast, cervical, esophageal, and stomach cancers (among others) and was chosen as the therapeutic for this study.[23] UiO-AZB NPs were loaded with 5-FU via a simple impregnation method commonly used in the literature[24] prior to coating with the PEG-NH_2 polymer, and the loaded samples will be referred to as PEGNH_2@5-FU-UiOAZB. Powder X-ray diffraction (PXRD, Figure 4.1, A) analysis confirms the crystalline structure remains intact after 5-FU uptake over 3 days, beyond which time period crystallinity is lost. This loss of crystallinity is thought to be due to framework disruption when more 5-FU binds and begins to replace the AZB linker after 3 days. Additionally, upon further analysis, a few of the peaks at lower angles (< 15°) shift slightly to the right (higher angle, Figure S4.2), which according to Braggs Law is indicative of smaller unit cell parameters. A reduction in the size of the unit cell upon 5-FU loading suggests that there are 5-FU molecules binding to the framework, resulting in a slight contraction of the structure. This type of contraction or "breathing" behavior has been healthily

documented in the literature.[25-27] The extent of loading was monitored over the 3 day period and estimated via TGA (Figure 4.1, B). By taking the derivative with respect to temperature, the area under the curve can be integrated to give the extent of loading (Figure S4.3), with maximum loading (~15 wt%) occurring after 3 days. 5-FU binding is also evident in the TGA, as there are 2 losses attributed to both free and bound 5-FU occupying the pore spaces of UiO-AZB.

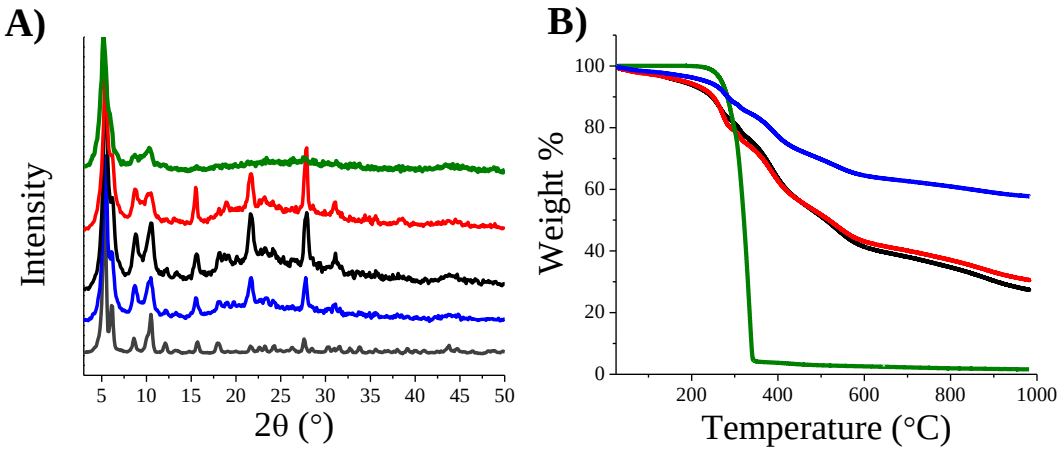

Figure 4.1. A) PXRD of as synthesized (gray) UiO-AZB and $PEGNH_2$@5-FU-UiOAZB with impregnation times of 1 day (blue), 2 days (black), 3 days (red), and 4 days (green). B) TGA of 5-FU (green), $PEGNH_2$@5-FU-UiOAZB with impregnation times of 1 day (blue), 2 days (black), and 3 days (red).

4.4.3 Surface functionalization and stability

Surface modification of NPs is important to stabilize them and avoid elimination by phagocytosis in the reticuloendothelial system.[28] This is typically achieved by the addition of a stabilizing polymer, most commonly PEG due to its ability to provide long blood circulation times of over 40 hours.[29-31] After loading the NPs with 5-FU, the amine terminated PEG was attached to the surface by allowing the material to stir in a solution containing the polymer (see section 4.3.3). TGA data was used to estimate the PEG-NH_2 coverage in the same manner as described for 5-FU loading, and was found to be ~15 wt %. Additionally, NMR was used to

confirm this surface coverage. The UiO-AZB NPs are not stable in phosphate buffer due to ligand exchange of the carboxylate linkers for phosphate groups. $PEGNH_2$@5-FU-UiOAZB was added to a 50 mM Na_2HPO_4 in D_2O solution and sonicated in a water bath for 1 hour. To the digested solution, 4 x 10^{-7} moles of 3-(trimethylsilyl)-1-propionic acid sodium salt (TMPS) was added as an internal standard. A ^{1}H-NMR spectrum of this solution is shown in Figure S4.4. The four azobenzene peaks observed are due to the presence of both the trans and cis forms in the digested solution. Using the internal standard at 0 ppm the surface coating of the UiO-AZB NPs was found to be 16 wt% PEG, which is in agreement with the value determined through TGA. To confirm that the primary amine end functionality of the PEG is obligatory for surface coating, the coating procedure was replicated using un-functionalized HO-PEG-OH. Using the same digestion technique described previously the coating was determined to be 4 wt %, indicating that some non-specific surface coating is achieved without the primary amine functionality. Surface modified UiO-AZB NPs provided increased dispersion, while un-functionalized NPs formed large agglomerates in solution (Figure S4.5). The NPs were dispersed in deionized water and DLS measurements were taken every 30 minutes over 20 hours. The average size of the NPs was found to be 140 ± 4 nm (Figure 4.2, A), and remained colloidally stable over the time studied. The hydrodynamic radius increased 12 nm from the uncoated UiO-AZB (128 ± 3 nm) due to the addition of the PEG coating.

The surface charge of the NPs should also be considered. It has been demonstrated that hydrophobic and highly charged particles are eliminated more rapidly from the blood stream.[32-33] Due to the negatively charged cell membrane of endothelial cells that line blood vessel walls, cationic species are removed quicker. Whereas, particles with slightly negative or neutral charges demonstrate longer circulation half-lives due to decreased plasma protein adsorption.[33-35] The

zeta potential of the $PEGNH_2$@UiOAZB NPs in water was measured to be -5.33 mV, indicating the proper surface charge for longer half-lives and better biodistribution. Additionally, the slight charge also aids in the dispersion and charge repulsion that prevents NP aggregation. To test the effect of protein adsorption on the surface of $PEGNH_2$@5-FU-UiOAZB the NPs were incubated with fetal bovine serum (FBS) at room temperature for 1 hour and the NPs were washed via centrifugation. The size and zeta potential of the NPs were measured (Figure 4.3, B). DLS shows an increase in size of ~100 nm, indicating that the protein corona is composed of more than one layer of adsorbed protein. It is important to note that the size distribution of the NPs stays monodispersed after FBS incubation, indicating a consistent protein corona thickness and no aggregation induced from adsorbed proteins. After FBS incubation the zeta potential decreases to -24.08 mV. This is in agreement with previous studies that show a zeta potential around 20 mV after FBS incubation independent of the original NP surface charge.[36-37]

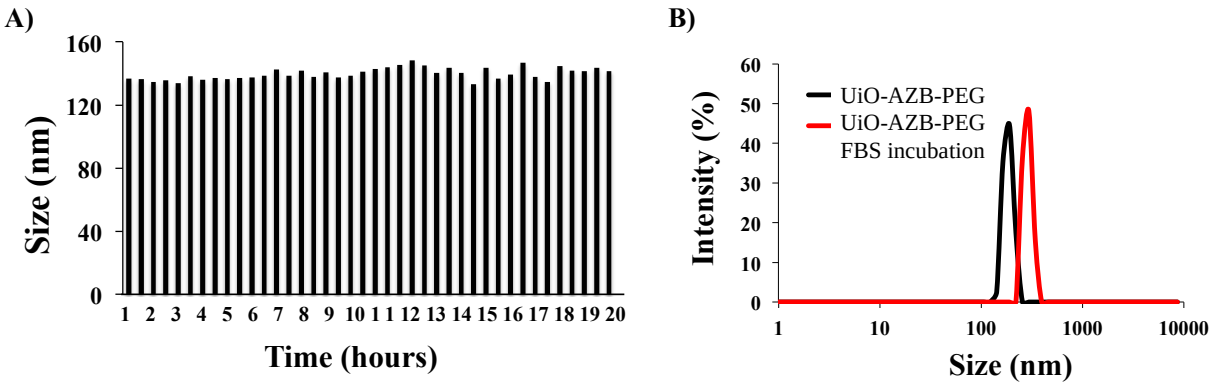

Figure 4.2. A) DLS data over 20 hours showing no change in UiO-AZB size in solution. B) DLS measurements of $PEGNH_2$@UiOAZB before and after incubation with fetal bovine serum.

TEM (Figure 4.3, A) further confirms the size (~100 nm) of the NPs and agrees with previously reported sizes of the nano-MOF.[18] The $PEGNH_2$@5-FU-UiOAZB is further characterized through FT-IR spectroscopy (Figure 4.3, B). UiO-AZB (black) displays

carboxylate stretches at 1600, 1558, and 1415 cm^{-1}, indicative of carboxylate chelation to the metal nodes. The FT-IR spectrum of 5-FU (blue) contains a broad band between 2700 and 3300 cm^{-1} attributed to the NH stretching, a band at 1630 cm^{-1} due to the carbonyl stretching, and a peak at 1238 cm^{-1} from the C-F bond. The final product, $PEGNH_2$@5-FU-UiOAZB (green) exhibits a combination of the stretches seen from UiO-AZB, PEG, and 5-FU. The two sharp peaks from UiO-AZB (1600 and 1558 cm^{-1}) are observed along with a broader PEG peak at 1660 cm^{-1}. This broadening is attributed to the presence of 5-FU that has an overlapping stretch at 1630 cm^{-1}. This data is evidence of successful polymer coating of the material along with evidence of drug encapsulation.

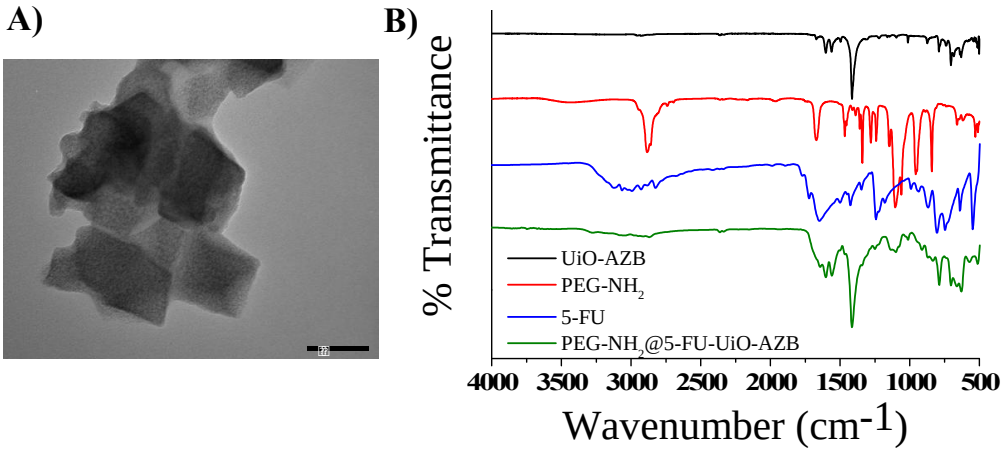

Figure 4.3. A) TEM image of $PEGNH_2$@UiOAZB NPs, scale bar is 80 nm. B) FT-IR analysis of UiO-AZB (black), NH_2-PEG-NH_2 (red), 5-FU (blue), and $PEGNH_2$@5-FU-UiOAZB (green).

4.4.4 Light induced degradation

The degradation of the $PEGNH_2$@5-FU-UiOAZB was studied using UV-Vis in order to probe the light sensitivity of the NPs. Particles were submersed in simulated cerebrospinal fluid (see Supplemental Information for composition) and aliquots of the supernatant solution were

monitored over time for the presence of the azobenzene dicarboxylate (AZB) linker. After centrifuging to remove the $PEGNH_2$@5-FU-UiOAZB NPs, the absorbance of the supernatant was screened. Absorbance due to free AZB in solution is the result of the NPs degrading into their component ions (AZB^{2-} and Zr^{4+}). From the absorbance data, the concentration and subsequent % degradation of the material can be determined (see section 4.3.9). We have demonstrated this approach for evaluating the degradation profiles of the unmodified nanoparticles.[18] HPLC provided a secondary method to determine the concentration of AZB in the samples. Figure 4.4 shows the results of the experiments. There is an initial degradation of ~3-4 % perhaps due to starting material or uncoated NPs that degrade immediately. However, from the data, it is apparent that the particles are stable when no irradiation is present and under irradiation with 340 nm light, the degradation profile is accelerated. The polymer itself is not serving to prevent light from reaching the UiO-AZB particles, because $PEGNH_2$ does not absorb light efficiently at this wavelength. Therefore, isomerization events of the AZB linker occur and cause the material to degrade. We measured the temperature after 12 h of irradiation, and found that there was an increase to ~40 °C. To probe the degradation due to thermal effects, we also measured degradation in the dark with heating. Although the initial ~5 % degradation is slightly higher than the degradation in the dark without heating, the rate (measured after 3 h) was found to be 0.05 ± 0.02 %/h, while the rate under irradiation was 0.72 ± 0.03 %/h (using UV-Vis data) and so we conclude that thermal effects are not significant. Due to the mechanism of drug release relying on the degradation of the material, the prolonged stabilization of the delivery system in the dark is ideal. The degradation profile of the material in the dark and under irradiation indicates that minimal release will occur until the external stimulus is present.

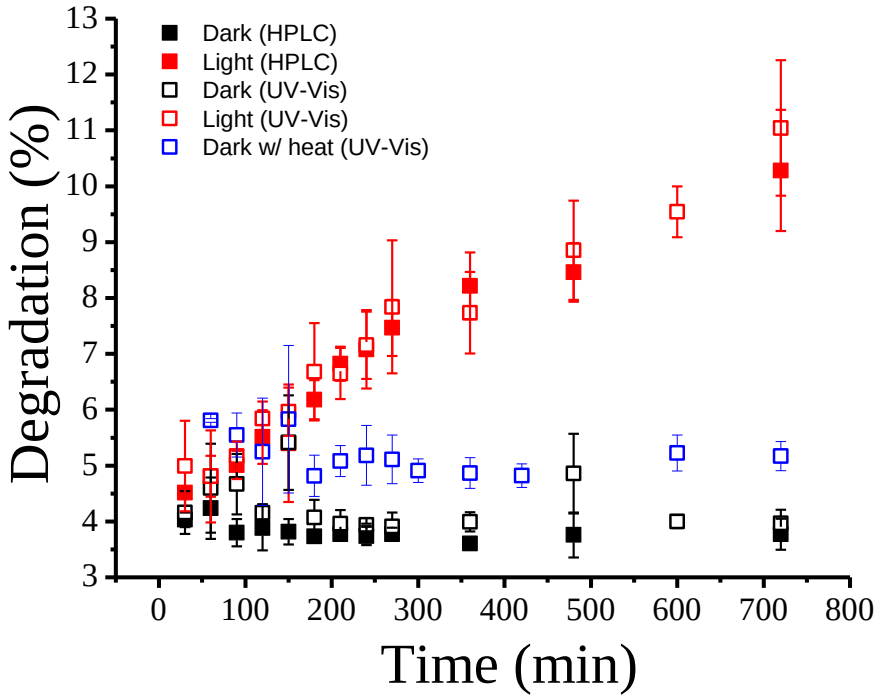

Figure 4.4. The percent degradation for samples kept in the dark (black), in the dark with heating (blue) and those irradiated with 340 nm UV light (red). Open squares represent data measured with UV-Vis and closed squares represent data measured with HPLC.

4.4.5 In vitro degradation studies

The high degree of control over the degradation of the NPs prompted us to demonstrate the biological applicability of $PEGNH_2$@5-FU-UiOAZB as an external stimulus controlled drug delivery vehicle. To this end, we incubated a breast cancer cell line, MCF-7, with varying concentrations of $PEGNH_2$@5-FU-UiOAZB. The cells were then irradiated with 340 nm light for 30 min or kept in the dark. We quantified the number of living cells using the MTT assay and compared the cell viability of the $PEGNH_2$@5-FU-UiOAZB treated cells to untreated cells. Figure 4.5 shows the cell viability of MCF-7 cells treated with $PEGNH_2$@5-FU-UiOAZB in concentrations of 500 – 3000 μg/mL. The cells kept in the dark experienced no NP dependent cell death. The light triggered degradation and subsequent release of the 5-FU is observed through the concentration dependent cell death. Higher concentrations of NPs result in an

increase in the toxicity to the cells. Also, to confirm that the NP components themselves were benign and only served to deliver the drug cargo, the cells were treated with $PEGNH_2$@UiOAZB NPs that were not loaded with 5-FU at the same concentrations that previously resulted in cell death. After irradiation with light no NP dependent cell death is observed. This confirms that it is the release of the 5-FU from the NP system that causes the cell death and not the free Zr, AZB, or PEG that are also present when the system degrades.

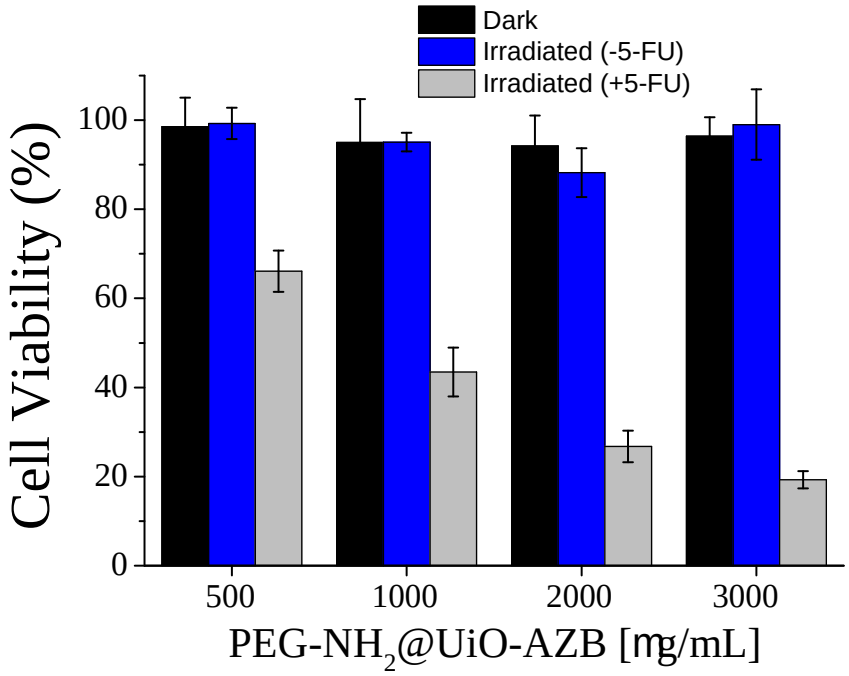

Figure 4.5. The cell viability of MCF-7 cells when treated with $PEGNH_2$@5-FU-UiOAZB and kept in the dark (black) or irradiated with 340 nm light (grey). Cells were also treated with $PEGNH_2$@UiOAZB NPs not loaded with 5-FU and irradiated (blue) to confirm that the NP components were not contributing to the toxicity. Each data point is the average of six independent experiments.

4.5 Conclusions

In summary, we have reported the design and successful photo-triggered degradation of PEG functionalized UiO-AZB nanocarriers. After optimization of 5-fluorouracil loading it was determined that the loaded cargo was both encapsulated and bound to the UiO-AZB NP. After

surface modification with PEG the $PEGNH_2$@5-FU-UiOAZB NPs were determined to be highly stable in biological medium. Upon irradiation with UV light a triggered degradation and subsequent release of 5-FU was observed. Minimal degradation is observed in the dark. In vitro testing of the drug delivery system demonstrated external-stimulus controlled cell death. This study highlights the scope and applicability of a photo-controlled MOF drug delivery system that promotes the utility of oxygen-independent photodynamic therapy.

4.6 Acknowledgements

The authors would like to thank the VT Department of Chemistry and the Institute for Critical Technology and Applied Science (ICTAS) at VT for support and funding of this work.

4.7 References

1. Li, J. R.; Kuppler, R. J.; Zhou, H. C., Selective Gas Adsorption and Separation in Metal-Organic Frameworks. *Chemical Society Reviews* **2009,** *38* (5), 1477-1504.

2. Seo, J. S.; Whang, D.; Lee, H.; Jun, S. I.; Oh, J.; Jeon, Y. J.; Kim, K., A Homochiral Metal-Organic Porous Material for Enantioselective Separation and Catalysis. *Nature* **2000,** *404* (6781), 982-986.

3. Horcajada, P.; Serre, C.; Vallet-Regi, M.; Sebban, M.; Taulelle, F.; Ferey, G., Metal-Organic Frameworks as Efficient Materials for Drug Delivery. *Angewandte Chemie International Edition* **2006,** *45* (36), 5974-8.

4. Farha, O. K.; Eryazici, I.; Jeong, N. C.; Hauser, B. G.; Wilmer, C. E.; Sarjeant, A. A.; Snurr, R. Q.; Nguyen, S. T.; Yazaydın, A. Ö.; Hupp, J. T., Metal–Organic Framework Materials with Ultrahigh Surface Areas: Is the Sky the Limit? *Journal of the American Chemical Society* **2012,** *134* (36), 15016-15021.

5. Sun, C.-Y.; Qin, C.; Wang, X.-L.; Yang, G.-S.; Shao, K.-Z.; Lan, Y.-Q.; Su, Z.-M.; Huang, P.; Wang, C.-G.; Wang, E.-B., Zeolitic Imidazolate Framework-8 as Efficient Ph-Sensitive Drug Delivery Vehicle. *Dalton Transactions* **2012,** *41* (23), 6906-6909.

6. Horcajada, P.; Chalati, T.; Serre, C.; Gillet, B.; Sebrie, C.; Baati, T.; Eubank, J. F.; Heurtaux, D.; Clayette, P.; Kreuz, C.; Chang, J.-S.; Hwang, Y. K.; Marsaud, V.; Bories, P.-N.; Cynober, L.; Gil, S.; Férey, G.; Couvreur, P.; Gref, R., Porous Metal–Organic-Framework Nanoscale Carriers as a Potential Platform for Drug Delivery and Imaging. *Nature Materials* **2010,** *9* (2), 172-178.

7. Horcajada, P.; Gref, R.; Baati, T.; Allan, P. K.; Maurin, G.; Couvreur, P.; Férey, G.; Morris, R. E.; Serre, C., Metal–Organic Frameworks in Biomedicine. *Chemical Reviews* **2012,** *112* (2), 1232-1268.

8. MacEwan, S. R.; Callahan, D. J.; Chilkoti, A., Stimulus-Responsive Macromolecules and Nanoparticles for Cancer Drug Delivery. *Nanomedicine (London, England)* **2010,** *5* (5), 793-806.

9. Hobbs, S. K.; Monsky, W. L.; Yuan, F.; Roberts, W. G.; Griffith, L.; Torchilin, V. P.; Jain, R. K., Regulation of Transport Pathways in Tumor Vessels: Role of Tumor Type and Microenvironment. *Proceedings of the National Academy of Science U S A* **1998,** *95* (8), 4607-12.

10. Amoozgar, Z.; Yeo, Y., Recent Advances in Stealth Coating of Nanoparticle Drug Delivery Systems. *Wiley Interdisciplinary Reviews: Nanomedicine and Nanobiotechnology* **2012,** *4* (2), 219-33.

11. Yao, J.; Feng, J.; Chen, J., External-Stimuli Responsive Systems for Cancer Theranostic. *Asian Journal of Pharmaceutical Sciences* **2016,** *11* (5), 585-595.

12. Tan, L.-L.; Li, H.; Zhou, Y.; Zhang, Y.; Feng, X.; Wang, B.; Yang, Y.-W., Zn2+-Triggered Drug Release from Biocompatible Zirconium Mofs Equipped with Supramolecular Gates. *Small* **2015,** *11* (31), 3807-3813.

13. An, J.; Geib, S. J.; Rosi, N. L., Cation-Triggered Drug Release from a Porous Zinc−Adeninate Metal−Organic Framework. *Journal of the American Chemical Society* **2009,** *131* (24), 8376-8377.

14. Dewhirst, M. W., Mechanisms Underlying Hypoxia Development in Tumors. In *Oxygen Transport to Tissue XXIII: Oxygen Measurements in the 21st Century: Basic Techniques and Clinical Relevance*, Wilson, D. F.; Evans, S. M.; Biaglow, J.; Pastuszko, A., Eds. Springer US: Boston, MA, 2003; pp 51-56.

15. Albani, B. A.; Peña, B.; Leed, N. A.; de Paula, N. A. B. G.; Pavani, C.; Baptista, M. S.; Dunbar, K. R.; Turro, C., Marked Improvement in Photoinduced Cell Death by a New Tris-Heteroleptic Complex with Dual Action: Singlet Oxygen Sensitization and Ligand Dissociation. *Journal of the American Chemical Society* **2014,** *136* (49), 17095-17101.

16. Higgins, S. L. H.; Brewer, K. J., Designing Red-Light-Activated Multifunctional Agents for the Photodynamic Therapy. *Angewandte Chemie International Edition* **2012,** *51* (46), 11420-11422.

17. Naik, A.; Rubbiani, R.; Gasser, G.; Spingler, B., Visible-Light-Induced Annihilation of Tumor Cells with Platinum–Porphyrin Conjugates. *Angewandte Chemie International Edition* **2014,** *53* (27), 6938-6941.

18. Epley, C. C.; Roth, K. L.; Lin, S.; Ahrenholtz, S. R.; Grove, T. Z.; Morris, A. J., Cargo Delivery on Demand from Photodegradable Mof Nano-Cages. *Dalton Transactions* **2017**.

19. Schaate, A.; Dühnen, S.; Platz, G.; Lilienthal, S.; Schneider, A. M.; Behrens, P., A Novel Zr-Based Porous Coordination Polymer Containing Azobenzenedicarboxylate as a Linker. *European Journal of Inorganic Chemistry* **2012,** *2012* (5), 790-796.

20. Shi, J.; Chen, Z.; Wang, L.; Wang, B.; Xu, L.; Hou, L.; Zhang, Z., A Tumor-Specific Cleavable Nanosystem of Peg-Modified C60@Au Hybrid Aggregates for Radio Frequency-Controlled Release, Hyperthermia, Photodynamic Therapy and X-Ray Imaging. *Acta Biomaterialia* **2016,** *29*, 282-297.

21. Xu, Q.; Ensign, L. M.; Boylan, N. J.; Schön, A.; Gong, X.; Yang, J.-C.; Lamb, N. W.; Cai, S.; Yu, T.; Freire, E.; Hanes, J., Impact of Surface Polyethylene Glycol (Peg) Density on Biodegradable Nanoparticle Transport in Mucus Ex Vivo and Distribution in Vivo. *ACS Nano* **2015,** *9* (9), 9217-9227.

22. Chieng, B.; Ibrahim, N.; Yunus, W.; Hussein, M., Poly(Lactic Acid)/Poly(Ethylene Glycol) Polymer Nanocomposites: Effects of Graphene Nanoplatelets. *Polymers* **2014,** *6* (1), 93.

23. Bag, P. P.; Wang, D.; Chen, Z.; Cao, R., Outstanding Drug Loading Capacity by Water Stable Microporous Mof: A Potential Drug Carrier. *Chemical Communications* **2016,** *52* (18), 3669-3672.

24. Horcajada, P.; Serre, C.; Vallet-Regí, M.; Sebban, M.; Taulelle, F.; Férey, G., Metal–Organic Frameworks as Efficient Materials for Drug Delivery. *Angewandte Chemie International Edition* **2006,** *45* (36), 5974-5978.

25. Murdock, C. R.; Hughes, B. C.; Lu, Z.; Jenkins, D. M., Approaches for Synthesizing Breathing Mofs by Exploiting Dimensional Rigidity. *Coordination Chemistry Reviews* **2014,** *258–259*, 119-136.

26. Lv, X.; Li, L.; Tang, S.; Wang, C.; Zhao, X., High Co2/N2 and Co2/Ch4 Selectivity in a Chiral Metal-Organic Framework with Contracted Pores and Multiple Functionalities. *Chemical Communications* **2014,** *50* (52), 6886-6889.

27. Joo, J.; Kim, H.; Han, S. S., Volume Shrinkage of a Metal-Organic Framework Host Induced by the Dispersive Attraction of Guest Gas Molecules. *Physical Chemistry Chemical Physics* **2013,** *15* (43), 18822-18826.

28. Moghimi, S. M.; Patel, H. M., Serum-Mediated Recognition of Liposomes by Phagocytic Cells of the Reticuloendothelial System – the Concept of Tissue Specificity. *Advanced Drug Delivery Reviews* **1998,** *32* (1–2), 45-60.

29. Moghimi, S. M.; Hunter, A. C.; Murray, J. C., Long-Circulating and Target-Specific Nanoparticles: Theory to Practice. *Pharmacological Reviews* **2001,** *53* (2), 283-318.

30. Ebrahimnejad, P.; Dinarvand, R.; Jafari, M. R.; Tabasi, S. A. S.; Atyabi, F., Characterization, Blood Profile and Biodistribution Properties of Surface Modified Plga Nanoparticles of Sn-38. *International Journal of Pharmaceutics* **2011,** *406* (1–2), 122-127.

31. Jokerst, J. V.; Lobovkina, T.; Zare, R. N.; Gambhir, S. S., Nanoparticle Pegylation for Imaging and Therapy. *Nanomedicine* **2011,** *6*, 715+.

32. Yamamoto, Y.; Nagasaki, Y.; Kato, Y.; Sugiyama, Y.; Kataoka, K., Long-Circulating Poly(Ethylene Glycol)–Poly(D,L-Lactide) Block Copolymer Micelles with Modulated Surface Charge. *Journal of Controlled Release* **2001,** *77* (1–2), 27-38.

33. Sheng, Y.; Yuan, Y.; Liu, C.; Tao, X.; Shan, X.; Xu, F., In vitro Macrophage Uptake and In vivo Biodistribution of Pla–Peg Nanoparticles Loaded with Hemoglobin as Blood Substitutes: Effect of Peg Content. *Journal of Materials Science: Materials in Medicine* **2009,** *20* (9), 1881-1891.

34. Yamamoto, Y.; Nagasaki, Y.; Kato, Y.; Sugiyama, Y.; Kataoka, K., Long-Circulating Poly(Ethylene Glycol)-Poly(D,L-Lactide) Block Copolymer Micelles with Modulated Surface Charge. *Journal of Controlled Release* **2001,** *77* (1-2), 27-38.

35. He, C.; Hu, Y.; Yin, L.; Tang, C.; Yin, C., Effects of Particle Size and Surface Charge on Cellular Uptake and Biodistribution of Polymeric Nanoparticles. *Biomaterials* **2010,** *31* (13), 3657-3666.

36. Ritz, S.; Schöttler, S.; Kotman, N.; Baier, G.; Musyanovych, A.; Kuharev, J.; Landfester, K.; Schild, H.; Jahn, O.; Tenzer, S.; Mailänder, V., Protein Corona of Nanoparticles: Distinct Proteins Regulate the Cellular Uptake. *Biomacromolecules* **2015,** *16* (4), 1311-1321.

37. Alkilany, A. M.; Nagaria, P. K.; Hexel, C. R.; Shaw, T. J.; Murphy, C. J.; Wyatt, M. D., Cellular Uptake and Cytotoxicity of Gold Nanorods: Molecular Origin of Cytotoxicity and Surface Effects. *Small* **2009,** *5* (6), 701-8.

38. Artificial cerebrospinal fluid, HEPES-buffered. *Cold Spring Harbor Protocols* **2011,** *2011* (10), pdb.rec066696.

4.8 Supplemental Information

Simulated Cerebrospinal Fluid (SCF) Components

Simulated cerebrospinal fluid (SCF) was made following a Cold Spring Harbor Laboratory Press protocol.[38] The solution consists of 135 mM sodium chloride (NaCl), 5.4 mM potassium chloride (KCl), 5 mM4-(2-Hydroxyethyl)piperazine-1-ethanesulfonic acid sodium salt **(**Na-HEPES buffer), 1.8 mM calcium chloride ($CaCl_2$), and 1 mM magnesium chloride ($MgCl_2$). The pH of the solution was adjusted to 7.3 by adding concentrated (~12 M) hydrochloric acid.

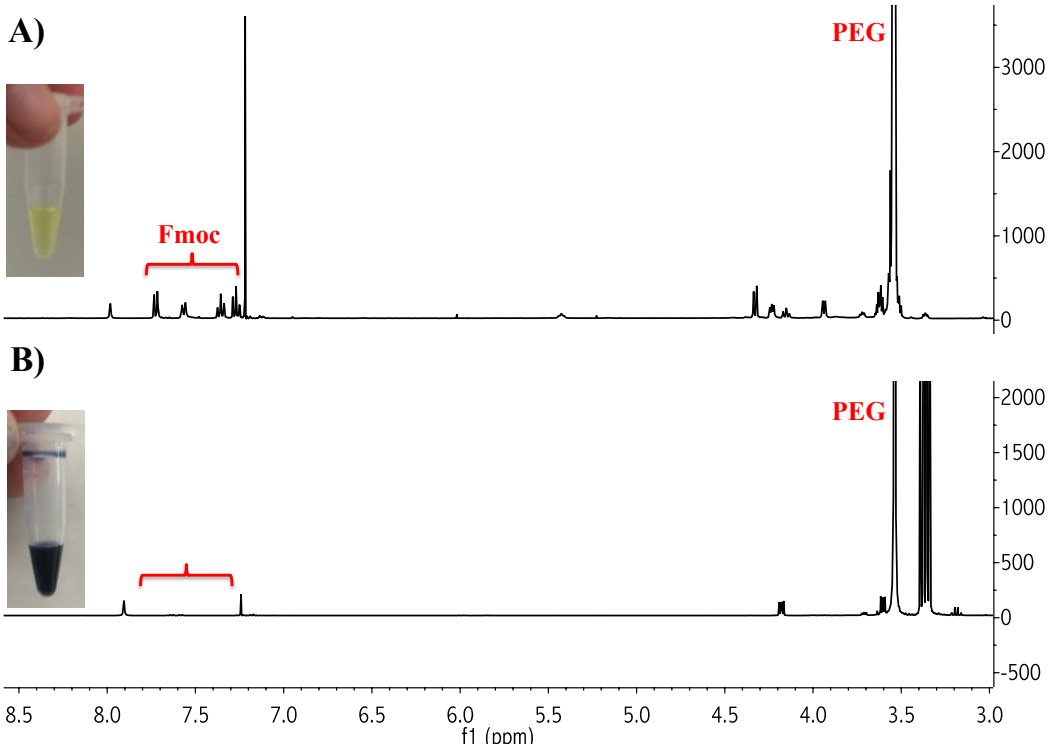

Figure S4.1. A) NMR analysis of Fmoc-PEG-Fmoc showing a peak for PEG and four peaks for the Fmoc group. The inset shows an image of a negative Kaiser test. B) NMR analysis of aminated PEG after removal of the Fmoc protecting groups, no peaks for Fmoc are seen indicating 100% removal. The inset shows an image of a positive Kaiser test.

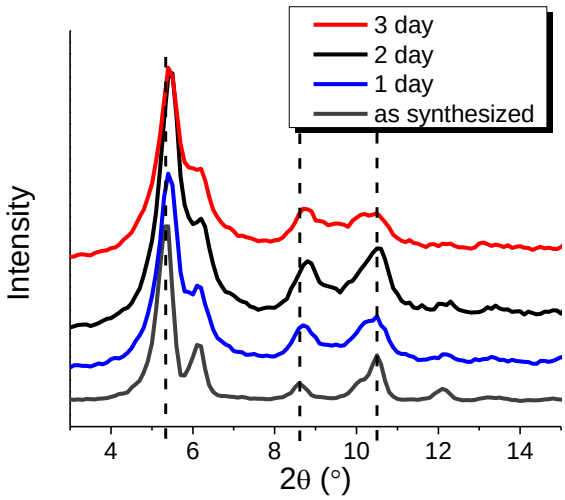

Figure S4.2. Zoomed in view of peaks below 15° to demonstrate a slight shift of some of the peaks to higher angle.

A)

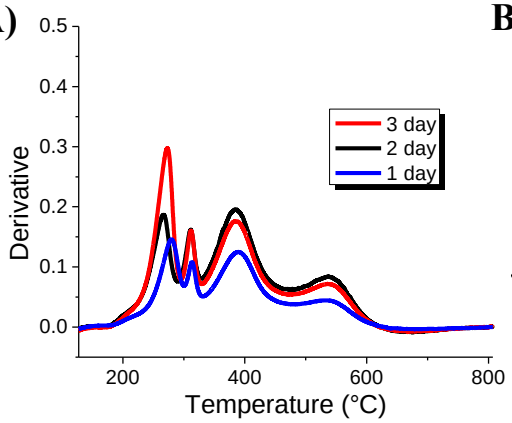

B)

Treatment	Loading (Wt %)
1 day	8.2
2 day	11.9
3 day	14.9

Figure S4.3. A) Derivative weight percent vs. temperature used to determine loading percent. B) Table indicating time of treatment and subsequent loading percent.

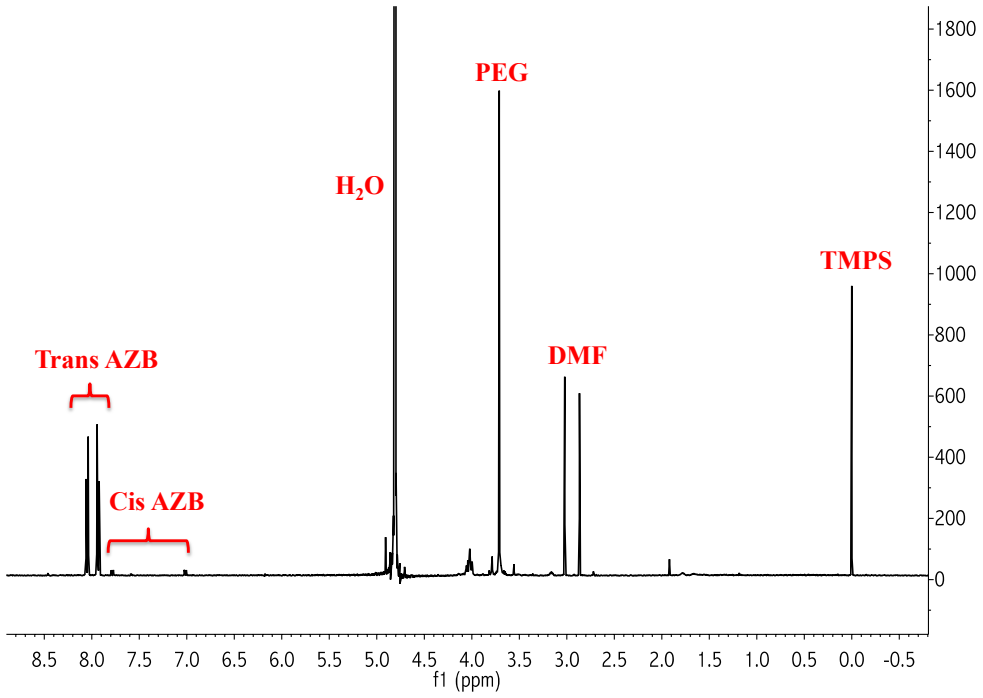

Figure S4.4. ^{1}H-NMR analysis of PEGNH_2@UiOAZB after digestion with Na_2HPO_4.

Figure S4.5. Image of UiO-AZB NPs (left) and PEGNH_2@5-FU-UiOAZB NPs (right) in DI water.

5. Nanoparticulate Manganese-containing Coordination Polymers for Bimodal Imaging Theranostics

This chapter has been prepared for publication in collaboration with C.C. Epley, K. L. Roth, T.Z. Grove, and A.J. Morris.

5.1 Abstract

Bimodal imaging theranostics are the next generation of personalized medicine, which combine the advantages of complementary detection techniques with drug delivery vehicles. In this work, the synthesis of nanoparticulate manganese-based coordination polymers, $[Mn(abdc)(H_2O)_{1.5}(DMF)_{0.17}]_n$, where abdc = 4,4´-azobenzenedicarboxylate, for dual-mode magnetic resonance (MR) and optical imaging concurrent with drug delivery is described. Derivatives of azobenzene have previously shown anti-cancer activity, and, therefore, as the nanoparticles (NPs) degrade, drug is released. The NPs, when functionalized with a biocompatible NH_2-PEG-b-PCL-NH_2 copolymer, exhibited slow controlled release, resisted aggregation, and remained dispersed over a 15 h time period. Covalent attachment of a rhodamine dye to the polymer shell imparted fluorescence imaging ability and the cellular uptake of the nanoparticles was demonstrated to be rapid and efficient. Additionally, the incorporation of Mn^{II} in the coordination polymer allowed for MR imaging with a relaxivity ratio (r_2/r_1) of 13.03 for the polymer-coated materials.

5.2 Introduction

In the early 1900's the idea of designing molecular species incorporating domains capable of varying functionality within the body was at the forefront of medical research.[1] Particularly, the concept of delivering therapeutic moieties specifically to a targeted site while

being able to simultaneously detect or image if/when a system hones problematic areas is especially important for cancer research. Materials combining such properties of therapy and diagnostics in a single system are termed theranostics. Nanoparticles (NPs) as drug delivery vectors[2-4] have been popular in theranostic design since the discovery of the enhanced permeability and retention (EPR) effect.[5] The EPR effect was so named due to the observation that particulates on the order of 50-200 nm preferentially accumulate in tumors, thereby allowing for indirect tumor targeting by simply limiting particle sizes. Inorganic NPs (iNPs), such as iron oxides[6-9] and MnO,[10-12] have received great attention in theranostic system design due to the inclusion of magnetic resonance imaging (MRI) active paramagnetic ions. However, drug loading in iNPs is limited to surface attachment, or integration into a surface bound polymer matrix.[13-15] This typically leads to relatively low loadings and limits theranostic application.[16-17] For this reason, alternative nanoparticulate architectures including porous silica, liposomes, micelles, emulsions, and dendrimers have been studied.[18-21] In particular, micellar structures provide a platform to encapsulate both high concentration of insoluble drugs and imaging agents.[22-24]

Recently, there has been increased interest in the development of multimodal imaging agents that integrate two or more imaging capabilities into one theranostic system.[25-33] Each complementary imaging technique provides advantages (spatial/temporal resolution, sensitivity, tissue penetration, quantitative accuracy) and, therefore, can speed the clinical development of new pharmaceuticals, as well as shorten the time required for disease diagnosis. Commonly, MRI and fluorescence detection are combined.[25-26, 31-32, 34-39] MRI is ideal for whole body images because of the rapid scan time, high spatial resolution, and unlimited tissue penetration. Fluorescence-based imaging provides high sensitivity and high resolution images on the cellular

to subcellular level. Paramagnetic iNPs have been surface-derivatized with fluorescent tags, and polymeric micelles have been utilized to encapsulate both small iNPs for fluorescence detection (quantum dots) and/or MRI (iron oxides).[21, 25-26] Multiple other approaches have been investigated and are the subject of various recent reviews.[27, 29, 40-42]

An alternative to these established approaches for bimodal imaging theranostics is the use of coordination polymers (CPs), including porous metal-organic frameworks (MOFs). Several reviews highlight the use of MOFs and CPs for theranostic applications.[43-47] CPs consist of metal nodes bridged by multidentate organic linkers. Due to their high porosity and surface area, MOFs offer high drug loading capacities in comparison to iNPs and micelles.[48] Additionally, therapeutics can be incorporated as the organic linker, providing an avenue for dual drug delivery (linker and pore bound), which may lead to favorable pharmacokinetics. The incorporation of (super)paramagnetic metal nodes (Gd^{III}, Fe^{II}, Mn^{II}) into the MOF structure also offers the integrated advantage of MR contrast.[49-51] The pioneering work of Lin led to the first example of bimodal (MR and optical) imaging by a lanthanide-doped Gd-based nanoMOF.[52] While these nanoMOFs offered fluorescence imaging (<600 nm) and T_2-weighted MR contrast, to our knowledge, therapeutic capability was not incorporated.

Herein, we report the first investigation of a bimodal CP theranostic. NPs of a Mn^{II}-based CP, designated as $[Mn(abdc)(H_2O)_{1.5}(DMF)_{0.17}]_n$, incorporating 4,4´-azobenzenedicarboxylate (abdc) linkers were synthesized for the first time. In addition to MRI-active paramagnetic Mn^{II} metal centers, the material was surface functionalized with an amine-capped PEG-PCL copolymer that provided for covalent attachment of fluorescent probes to the polymer shell. For therapeutic function, the material integrates abdc as the organic linker. Azobenzene derivatives have been shown to be effective as anti-cancer agents,[53] and so the incorporation of abdc into the

structure of the NPs allows for simultaneous drug delivery upon material degradation. Material degradation was slow and controlled (15 wt% after 30 h). Therefore, the NPs are applicable for slow drug release and delivery, as well as demonstrating long imaging lifetimes.

5.3 Experimental

5.3.1 Materials

The 4-nitrobenzoic acid (98 %), sodium hydroxide (≥ 98 %), D-glucose (≥ 98 %), $MnCl_2$•$4H_2O$ (≥98 %), ε-caprolactone (99 %), polyethylene glycol (PEG; M_n = 1,000 g/mol), potassium hydroxide (98 %), diisopropylethyl amine (DIEA), fluorenylmethyloxycarbonyl (FMOC)-glycine (>98 %), piperidine (99 %), N-(3-dimethylaminopropyl)-N'-ethylcarbodiimide hydrochloride (EDC, >99 %), and N-hydroxysuccinimide (NHS, 98 %) were purchased from Sigma Aldrich and used without further purification. Glacial acetic acid (certified ACS) and dimethylformamide (DMF, Spectrophotometric grade ≥99.8 %) were used as received from Fischer Scientific. The 2-(6-chloro-1H-benzotriazole-1-yl)-1,1,3,3-tetramethylaminium hexafluorophosphate (HCTU) was purchased from Peptides International and the 5(6)-carboxytetramethylrhodamine was obtained from Novabiochem. Dulbecco's Modified Eagle's Medium (DMEM) and Hank's Balanced Salt Solution (HBSS) were purchased from Life Technologies.

5.3.2 Synthesis of 4,4´-azobenzenedicarboxylic acid (AZB)[54]

4-nitrobenzoic acid (13 g) and 250 mL of 5 M NaOH were heated to 50 °C in a 500 mL round bottom flask. A solution of 3.7 M D-glucose (150 mL) was added slowly to the flask before cooling to room temperature. The solution was aerated for 12 h and 5 M (200 mL) acetic acid was added to precipitate the abda. The pink solid was collected via vacuum filtration and dried in a 100 °C oven overnight. (9.6 g, ~91 %) ^{1}HNMR (500 MHz, D_2O, δ, ppm) trans: 7.94,

7.92 (d, 2H, J= 10 Hz), 7.82, 7.80 (d, 2H, J = 10 Hz), cis: 7.68, 7.66 (d, 2H, J=10 Hz), 6.91, 6.89 (d, 2H, J = 10 Hz),), Figure S5.1 (M^- = 269 *m/z*).

5.3.3 Synthesis of $[Mn(abdc)(H_2O)_{1.5}(DMF)_{0.17}]_n$ Nanoparticles (NPs)

Abda was dissolved in H_2O to give azobenzene dicarboxylate (abdc) by deprotonating with 15 % KOH drop wise and bath sonicating the solution for 10-15 min upon each addition of KOH until the desired concentration was reached, ensuring the pH remained neutral. 50mL of 0.1 M $MnCl_2 \cdot 4H_2O$ in DMF and 50 mL 0.05 M abdc in H_2O were heated to 90 °C then combined into a 125 mL Erlenmeyer flask by slowly adding the abdc solution to the solution containing Mn^{II}. The mixture was stirred while heating for 30 s before transfer to an ice bath. The particles were recovered via centrifugation at 10,000 rpm for 15 min and washed with ethanol (100 mL) after dispersion via sonication three times. The material was then dispersed in ~40 mL ethanol, transferred to a collection vessel, and dried under vacuum at 60 °C for 1 h, to yield NPs of $[Mn(abdc)(H_2O)_{1.5}(DMF)_{0.17}]_n$ (0.8 g; 95 % based on abdc). (Elemental analysis: 15.0 % Mn, 46.50 % C, 3.40 % H, and 7.94 % N; Calc: 15.2 % Mn, 48.05 % C, 3.36 % H, and 8.38 % N, Galbraith Laboratories).

5.3.4 Synthesis of NH_2-PEG-*b*-PCL-NH_2 Copolymer

Ring opening polymerization of ε-caprolactone (2.5 g) was initiated with potassium hydroxide (0.095 g). After stirring for 12 h at 130 °C, 1.69 g of polyethylene glycol (PEG; M_n = 1,000 g/mol) was added along with 1.40 g of HCTU and 0.66 g DIEA in DMF. The resulting mixture was stirred at 24 °C for an additional 12 h and precipitated in cold ethyl ether. The precipitate was re-dissolved in DMF and 1.25 g of Fmoc-glycine, 2.09 g HCTU, and 0.87 g DIEA were added to the mixture. After stirring at 24 °C for 12 h, the polymer mixture was precipitated in cold ethyl ether. The Fmoc group was removed by stirring for 1 h in a solution of

20 % piperidine in DMF. The diamine terminated copolymer was precipitated in cold ethyl ether and dried in a vacuum oven overnight.

5.3.5 Surface Modification of Nanoparticles with Copolymer

The same procedure for the uncoated material was followed, however, simultaneously upon transfer to an ice bath, a solution of 1.08 g NH_2-PEG-*b*-PCL-NH_2 copolymer in 5 mL DMF was added. The mixture was stirred at room temperature overnight and the coated material was collected via centrifugation at 10,000 rpm for 15 min. After removal of the supernatant, the particles were dispersed in 50 mL ethanol and centrifuged again at 10,000 rpm for 15 min. This washing process was repeated for a total of five washes, each with 50 mL ethanol, in order to remove un-tethered copolymer. After removal of the final supernatant, ~20 mL ethanol was added and the mixture was transferred to a collection vessel and dried via rotary evaporation.

5.3.6 Attachment of Fluorescent Dye

Fluorescent rhodamine dye was selectively attached to the primary amines available on the exterior of the polymer coated NP. Separate 1 mg/mL solutions of 5(6)-carboxytetramethylrhodamine, EDC, and NHS were prepared in water. The dried polymer coated NPs (3 mg) were combined with 534 µL of 5(6)-carboxytetramethylrhodamine, 3.594 mL of EDC, 431 µL of NHS, and 2 mL of pH 7.2 water. The mixture was stirred overnight and the NPs collected via centrifugation at 10,000 rpm for 5 min. After removal of the supernatant, the particles were dispersed in 1 mL water (pH=7.2) and centrifuged again; this washing process was repeated six times.

5.3.7 Fourier Transform Infrared Spectroscopy (FT-IR)

A Varian 670 FT-IR spectrometer with a diamond Specac Golden Gate attenuated total reflectance (ATR) attachment was used to collect infrared spectra. A background of air was

collected and subtracted from each sample spectra. For both background and sample collection, 64 scans with a resolution of 4 cm^{-1} were obtained from 4000-400 cm^{-1}

5.3.8 Powder X-ray Diffraction (PXRD)

For x-ray diffraction analysis, a 600 W Rigaku MiniFlex powder diffractometer operating with a Cu (K_α = 0.15418 nm) radiation source was used, with a 2θ sweeping range of 3-60° in continuous scanning mode. Data was collected in 0.1° increments at a scanning rate of 1°/min, and patterns were optimized with PDXL software.

5.3.9 Scanning Electron Microscopy (SEM)

A Leo (Zeiss) 1550 field-emission scanning electron microscope, equipped with an in-lens detector and operating at 5.0 kV, was used to collect SEM images. NPs were prepared for SEM imaging by first dispersing them in ethanol (0.1 mg/mL) via sonication. The resulting solution was then deposited via drop casting, with a short stem Pasteur pipette (1 drop), onto precut 5 mm x 5 mm glass slides. After oven drying, slides were mounted onto an SEM sample peg using double sided Cu tape and the sides of the slides were painted with carbon paint. A Cressington 208 High Resolution Sputter Coater with a Au/Pd target (80/20) was used to deposit a conductive layer on the surface of the slides in order to allow for imaging. Samples were coated for 60 seconds.

5.3.10 Thermogravimetric Analysis (TGA)

A Q-series TGA from TA instruments was used to analyze thermal stability of materials. 10 mg of sample in an aluminum pan were heated under nitrogen from 0 °C to 550°C with heating rate of 5 °C/min.

5.3.11 Fluorescence Spectroscopy

Fluorescence spectra were recorded using a Varian Carry Eclipse Fluorescence Spectrophotometer. The samples were prepared in 50 mM Na_2HPO4 buffer (pH 7.6). The path length was 1 cm with a cell volume of 100 uL. All measurements were excited with a 520 nm wavelength, and collected from 530 - 650 nm.

5.3.12 Relaxivity Measurements

The T_1 and T_2 relaxation times of the material were measured using a Bruker "the minispec" 60 MHz NMR instrument. Samples were prepared for NMR studies by dispersing the NPs in deionized water via sonication for 1 minute to make a 0.1 mg/mL stock solution. Standards of known concentration (0.05-0.5 mg/mL) were prepared from the stock and analyzed immediately in order to ensure that measurements were a result of the NPs and not the free Mn^{II} ion released by degradation of the material.

5.3.13 Degradation Studies

The degradation of the coated and uncoated materials was monitored using UV-Vis spectroscopy. Materials were submersed in 3 mL deionized H_2O and the absorption spectrum of the solution was taken at time intervals over a period of ~30 h. Spectral measurements were collected from 200-800 nm on a Cary 5000 UV-Vis-NIR spectrometer at a scan rate of 600 nm/min. A background of deionized water was collected over the same wavelength range and subtracted from sample spectra. After the final scan, the solutions were immediately filtered and the concentration of Mn^{II} was measured using Flame Atomic Absorption Spectroscopy (AAS). Standard solutions of $MnCl_2 \cdot 4H_2O$ ranging in concentration from 1-50 ppm were prepared and the atomic absorption of each solution was measured using a Perkin Elmer AAnalyst 200 Flame Atomic Absorption Spectrometer. A calibration curve of absorbance vs. concentration was

constructed. This curve was used to calculate the concentration of Mn^{II} in solution upon filtration of the NPs, and those values were compared to the concentration of abdc.

5.3.14 Dynamic Light Scattering (DLS)

The size distribution of the NPs was measured using a Malvern Zetasizer Nano-ZS, with at least five measurements taken for each sample. Uncoated NPs were suspended in ethanol and polymer coated NPs were suspended in 50 mM disodium phosphate buffer (pH=7.6). Samples were sonicated for 60 minutes and passed through a 0.45 µm filter prior to measurement.

5.3.15 *In vitro* Internalization Studies

HeLa cells were maintained in DMEM media supplemented with fetal bovine serum (10 %), penicillin (100 units/mL), and streptomycin (50 units/mL) at 37 °C in a CO_2 incubator (95 % relative humidity, 5 % CO_2). The cells were seeded at 8 x 10^3 per well in a 96-well plate and incubated for 24 h to reach 60 % confluency. The 5,6-carboxytetramethylrhodamine functionalized H_2N-PEG-*b*-PCL-NH_2 coated NPs (0.5 mg/mL) were incubated with the HeLa cells for 30 minutes. After incubation, the cells were washed three times with HBSS buffer and then imaged using an Olympus IX71 microscope fitted with an Olympus DP72 camera.

5.4 Results and Discussion

MRI is a powerful medical imaging technique used to identify and diagnose a variety of illnesses. Governed by the same principles as NMR spectroscopy, MRI exploits the sensitivity, abundance, and high density of protons *in-vivo*. The high density of protons in water and lipids found in tissues, however, offer poor spatial and/or structural contrast. Therefore, to enhance the overall quality of images and ease of MRI image interpretation, contrast agents are often employed, whose electromagnetic properties serve to improve image resolution and broaden the

scope of the technique.[9, 55-58] Manganese (specifically Mn^{II}) based nanomaterials are increasingly popular choices for investigation of MRI-active theranostic contrast agents due to significantly decreased toxicity in comparison to their Gd^{3+} based counterparts.[59] For this reason, Mn^{II} was chosen as the metal center for the design of the reported MRI-active CP.

Even with the added effect of contrast agents, resolution of MRI is lacking in comparison to fluorescence imaging, which can achieve resolution on the cellular to subcellular level. Additionally, fluorescence imaging is orders of magnitude more sensitive, resulting in a decrease in the amount of imaging agent required for quality spectra. However, fluorescence imaging relies on excited state relaxation of a chromophore upon light absorption. Therefore, the application of fluorescence imaging is limited due to the poor penetration depth of light into biological tissues.[60] In this regard, bimodal imaging agents that combine the functionality of both MR and fluorescence imaging can provide the advantages of both technologies in one vehicle. This becomes vital in the translation of bench-top drug discovery to clinical trials by eliminating the need for vehicle modification at the crucial transition from cellular to animal study. To impart fluorescence imaging ability to the reported bimodal imaging agent, rhodamine, a red-fluorescent dye (emission energy <700 nm), was covalently attached to the CP nanoparticles.

The last component of the theranostic described herein is the therapeutic agent. In CPs, the linkers can act as both the therapeutic and the structural scaffold of the material. Azobenzene dicarboxylate (abdc) was incorporated as such a dual-function linker in the reported CP. Azobenzene derivatives have been shown to exhibit cytotoxic action.[53] It is important to note that the simple abdc linker incorporated here is not expected to show significant anti-cancer activity. The incorporation of active abdc derivatives is an area of on-going investigation.

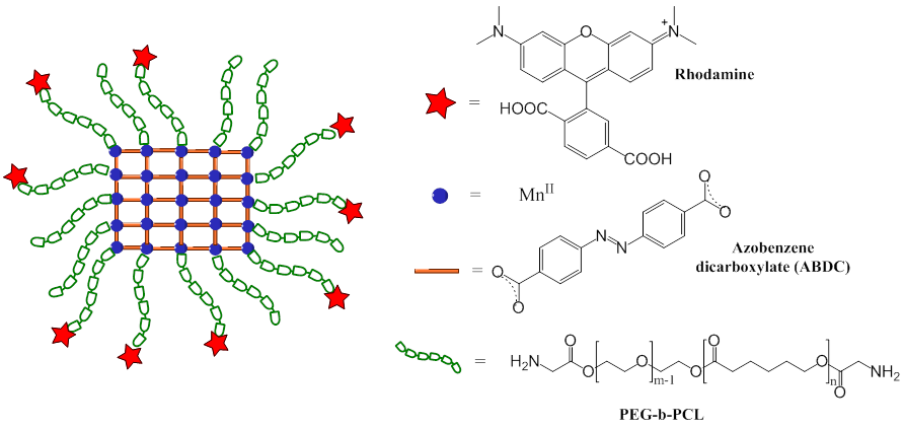

Figure 5.1 Schematic diagram of the bimodal imaging theranostic.

5.4.1 Nanoparticle Synthesis and Characterization

The design of theranostic systems for *in-vivo* applications begins with the formation of nanomaterials (~50-200 nm). Nanometer scale materials are required for efficient transport via the circulatory system, as the smallest capillaries are on the order of 200 nm. Additionally, to take advantage of the aforementioned EPR effect, the nanoparticles should be larger than 50 nm. Nanoscale CPs have previously been synthesized via solvothermal[61-63] and/or microemulsion[50, 52] techniques that employ long reaction times and multi-component surfactant systems. NPs of $[Mn(abdc)(H_2O)_{1.5}(DMF)_{0.17}]_n$ were synthesized via a fast and simple solvothermal precipitation method in which $MnCl_2 \cdot 4H_2O$ and azobenzene dicarboxylic acid (abda) starting materials were placed in separate solutions; DMF and H_2O, respectively. The solutions were each heated to 90 °C and then combined slowly before being cooled in an ice bath. After 18 h, the NPs were collected via centrifugation. Elemental analysis indicated a material consistent with a $[Mn(abdc)(H_2O)_{1.5}(DMF)_{0.17}]_n$ composition.

To further confirm the formation of a CP, PXRD, SEM, FT-IR, and TGA were utilized. PXRD of the NPs indicated a highly crystalline material (Figure 5.2) that was unidentified when compared to the International Center for Diffraction Database, suggesting a new material may have been synthesized. (PXRD pattern of starting abda is provided in Figure S5.2). Analysis of the peak width with the Scherrer equation (1),

$$\tau = \frac{K\lambda}{\beta \cos(\theta)} \quad (1)$$

where τ is a lower limit average of crystalline domain size, K is the shape factor (assumed to be 1), λ is the wavelength of the incident radiation, β is the peak width (expressed as Δ2θ) at the full width half max (FWHM) and θ is the Bragg angle, indicated a polycrystalline material with crystalline domains on the order of 30 nm. SEM of the particles showed that the average particle size is 200 nm (Figure 5.3). The average particle size was also confirmed via dynamic light scattering (Figure S5.3) that indicated the particles were poly-disperse with an average peak position at 231 ± 2 nm.

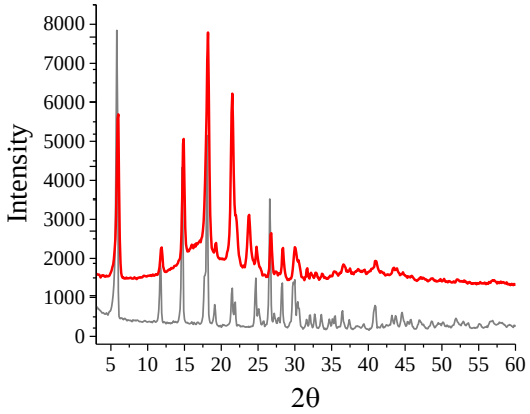

Figure 5.2 PXRD patterns of uncoated (gray) and coated (red) NPs. The baseline drifting in the pattern of the coated material suggests the presence of amorphous surface copolymer coating, while the retention of crystallinity is evidenced by the preservation of major peaks.

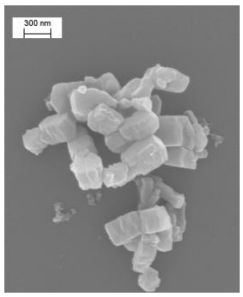

Figure 5.3. SEM image of $[Mn(abdc)(H_2O)_{1.5}(DMF)_{0.17}]_n$ NPs.

FT-IR spectra (Figure 5.4) of abda (light grey) and $[Mn(abdc)(H_2O)_{1.5}(DMF)_{0.17}]_n$ NPs (red) confirmed formation of a CP. The abda spectrum showed a peak at ~1740 cm^{-1} corresponding to the carbonyl stretch (C=O) in the abda starting material. In the NP spectrum, the disappearance of this peak and the appearance of a band at ~1500 cm^{-1} is consistent with a loss in carbon-oxygen double bond character upon metal binding to form the carboxylato (COO-) functionality. Thus, both carboxylate groups of abdc have complexed to Mn^{II} ions to form a CP.

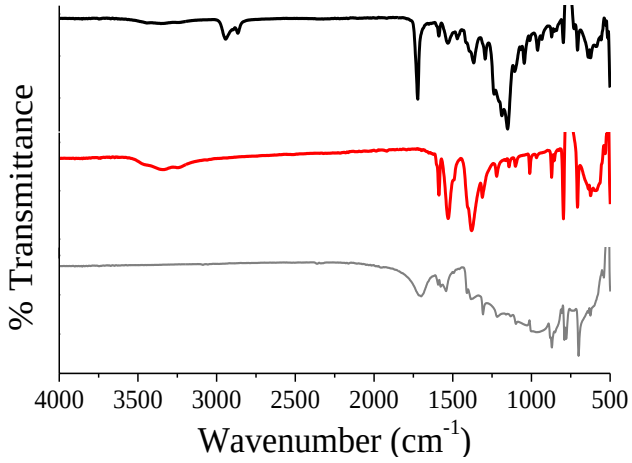

Figure 5.4. FT-IR of abda (bottom, light gray), uncoated (middle, red), and coated (top, black) NPs. The loss of the carbonyl (C=O) stretch (~1740 cm^{-1}) in the abda ligand and the appearance of carboxylato (COO-) peaks (~1500 cm^{-1}) in the spectrum of uncoated NPs indicate ligand coordination to the Mn^{II} ions. The appearance of the ether stretch (1240 cm^{-1}) and carbonyl stretch (1725 cm^{-1}) in the spectrum of the coated NPs (black) indicate polymer attachment.

Thermogravimetric analysis (TGA) was used to investigate the thermal stability and to confirm the composition of the NPs. From the curve of the NPs (red, Figure 5.5), two initial solvent losses are observed; the first takes off at ~150 °C and is attributed to water (7.6 % by weight) and the second loss takes off at ~200 °C and corresponds to a loss of DMF (3.4 %). Both solvent losses at 150 °C and 200 °C occur above the expected boiling points (100 °C and 151 °C) for H_2O and DMF, respectively. Therefore, the solvents are most likely physically bound to the Mn^{II} in the CP and are not the result of residual solvent in the pore space of the framework. The overall material was thermally stable up to ~500 °C, at which temperature the abdc starts to decompose as evidenced by the TGA curve of abdc (Figure S5.4).

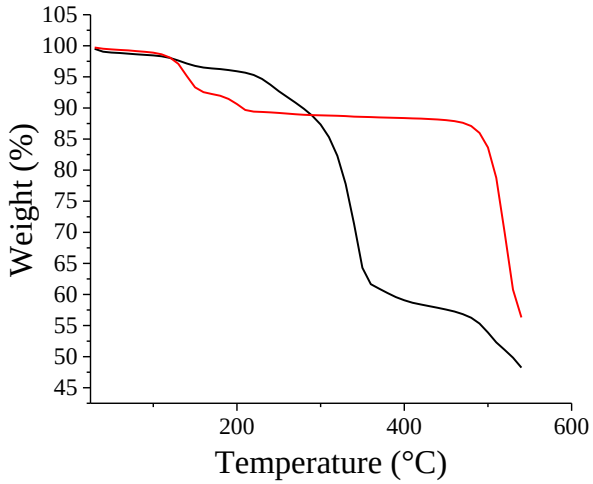

Figure 5.5 TGA curves of uncoated (red) and coated (black) NPs. The weight% losses in the TGA curve of dried NPs at ~150 °C and ~200 °C indicate the presence of bound water (~7.6 %) and DMF (~3.4 %), respectively. The same losses are observed in the curve of the coated NPs, yet, are less pronounced due to the presence of copolymer coating (~37 %).

Functionalization of NPs with stabilizers is necessary to avoid *in vivo* elimination by the immune system and to prevent nanoparticulate aggregation.[14, 32] A diamine terminated poly(ethylene glycol)-*b*-poly(caprolactone) (NH_2-PEG-*b*-PCL-NH_2) block copolymer was used to modify the surface of the $[Mn(abdc)(H_2O)_{1.5}(DMF)_{0.17}]_n$ NPs. PEG and PCL are FDA-

approved for use in the human body.[64] When combined with uncoated NPs, the primary amines of the block copolymer coordinate to surface exposed manganese ions. The hydrophobic PCL acts as a buffer region, keeping water away from the water-soluble NP and decreases their degradation in aqueous solutions. The hydrophilic PEG corona increases biocompatibility and dispersion of the NP.[65] PEG increases the longevity of NPs in physiological conditions by blocking the absorption of phagocyte signaling proteins and, thus, masking the NPs from the host immune system.[66-67] In addition, the primary amines located on the copolymer termini are protonated at physiological pH, decreasing aggregation of NPs due to charge-charge repulsion.[68]

The co-polymer synthesis was accomplished as follows (Scheme S1). The PCL block was synthesized by ring-opening polymerization of ε-caprolactone initiated by KOH in a 13:1 ratio, resulting in a molecular weight of 1,500 g/mol. In the presence of HCTU coupling reagent, an ester bond between the carboxylic acid terminus of PCL and the alkyl alcohol of the PEG is formed, resulting in PEG-b-PCL. To add amine functionality, the carboxyl group on Fmoc-glycine-OH was coupled to the hydroxyl termini of the PEG-*b*-PCL using HCTU. Removal of the Fmoc protecting group with piperidine results in primary amine termini.[69] The molecular mass of the block copolymer (2,400 g/mol) was confirmed with ^{1}HNMR (Figure S5.5).

Polymer coated NPs were prepared analogously to the uncoated material however, upon transferring the combined solutions to an ice bath, a mixture of 1.08 g NH_2-PEG-*b*-PCL-NH_2 copolymer in 5 mL DMF was added to the reaction and the mix was allowed to stir overnight. The coated-NPs were recovered and washed with ethanol via centrifugation to remove un-tethered copolymer before drying via rotary evaporation. From the FT-IR spectrum of the polymer coated NPs (Figure 5.4, black) a sharp peak was observed at 1725 cm^{-1}, corresponding to the carbonyl functionality in the PCL portion of the copolymer (Figure S5.6). Ether stretching

(1240 cm^{-1}) from the PEG portion was evident.[70] Also, the weak bands below 3000 cm^{-1} were consistent with the N-H stretch of the amine caps. The baseline drift in the PXRD pattern of the coated material (Figure 5.2, black) indicated amorphous surface functionalization of the material while the retention of NP crystallinity is evident. The water and DMF solvent loss characteristic of the uncoated NPs are also present in the TGA curve of the coated NPs (Figure 5.5, black), however, the large loss due to the polymer coating (37 %) that takes off around ~220 °C obscured these losses.

5.4.2 Dual-Mode Theranostic Capability

In order for CPs to be considered practical dual-mode theranostic devices, materials must initially meet several criteria: 1) they must demonstrate sufficient aqueous stability in order for the theranostic to reach its intended active site; 2) they must readily be taken up by cells; and 3) they should provide comparable or better fluorescence imaging and MR contrast than commercially available contrast agents.

As mentioned, theranostic CPs must be stable enough in aqueous media to ensure therapeutic function at the target site. Otherwise, the biological environment will quickly degrade the material, which will result in the premature release of drugs. Premature release, termed the "burst effect", causes the need for higher drug dose administration to ensure the delivery of the proper amount of drug cargos to the active site. For most drug delivery vehicles, the mechanism of delivery is degradation. Therefore, there is a delicate balance between premature release and on target release, controlled by the strength of coordination bonds within the polymer. Additionally, long term material decomposition is necessary in order to ensure metabolism and elimination from the body.

Typically, CPs made using carboxylato groups as the chelating functionality are inherently unstable in aqueous media due to protonation and hydrolysis of the coordination bonds.[32] For example, MRI-active Mn-based benzene tricarboxylate (BTC) MOFs demonstrate nearly 80 % degradation over a 30 hour time period.[50] We have found that the $[Mn(abdc)(H_2O)_{1.5}(DMF)_{0.17}]_n$ NPs reported here degrade by 20 % over 30 hours. A contributing factor to the decrease in degradation rate is that the abdc used in the backbone structure is a stronger base than BTC, discussed later in further detail.

UV-Vis spectroscopy was used to explore the aqueous degradation and ligand release from the coated and uncoated $[Mn(abdc)(H_2O)_{1.5}(DMF)_{0.17}]_n$ NPs. Degradation and release of abda from the material was studied over a period of ~30 h and was monitored by submersing the solids in DI water and observing the appearance of absorption peaks due to the free abdc ligand in solution over time. As expected, the absorbance of the solution increased over the 30 h period and was used to calculate the % release of abda from the materials (Figure 5.6A). The % release vs. time plot of the uncoated $[Mn(abdc)(H_2O)_{1.5}(DMF)_{0.17}]_n$ NPs (Figure 5.6B, closed black squares) displays biphasic behavior and slows significantly at 20 % ligand release over the 30 h period. Two processes are believed to be responsible for the observed behavior. Initially, the fast release from the material corresponds to weakly bound surface abdc that is easily hydrolyzed. Once the surface abdc linkers have been removed, the decreased rate of abda release results from the liberation of internally bound abdc that must undergo two hydrolysis events before release. The concentration of free Mn^{II} was measured after ~30 h using AAS and was, within reasonable error, equivalent to the abda concentration determined via UV-Vis, consistent with a 1:1 Mn^{II}:abdc ratio.

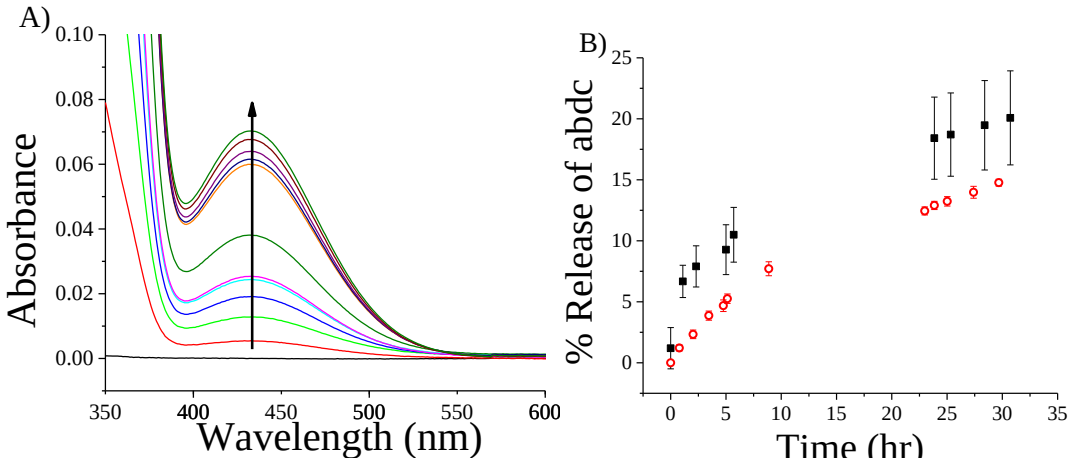

Figure 5.6. A) UV-Vis spectra monitored over a 30 h time period of the supernatant upon submersing the NPs in deionized water. The absorbance due to free abda increases over the observed time frame. B) Calculated % release of abda from coated (open red circles) and uncoated (closed black squares) NPs vs. time. The % release of uncoated NPs slows around 20 % after 30 h and is further decreased to 15 % for the coated NPs.

The exceptionally slow release profiles of abdc from the $[Mn(abdc)(H_2O)_{1.5}(DMF)_{0.17}]_n$ NPs is attributed to the strength of the carboxylate-Mn bond. It is well known that as the basicity of a ligand increases, so does the strength of the formed M-L bond. In the case of CPs, common linkers BDC and BTC are moderate donors with pKas of 3.51 and 3.12 for the first deprotonation event, respectively. While the measurement of the aqueous azobenzene dicarboxylate pKa was precluded by insolubility, estimates from similar known compounds (methyl red) put a lower limit on the pKa of 5.1.[71] Therefore, azobenzene dicarboxylate is a stronger base in comparison to BDC and BTC, which is the root cause of the increased stability.

It should be noted that the slowest drug release from CPs comes from Junior et. al[72] with a reported 66 % release of doxorubicin (an anticancer drug) from a zeolitic-imidazolate framework (ZIF-8) after 30 days. In this example, however, the pore spacing was about half that required for molecular docking within the material, and so doxorubicin was only bound to the surface of the ZIF-8. Therefore, the observed slow release was due to the strength of the bonds

formed between doxorubicin and free metal sites on the MOF surface. As a result, the drug loading was small (0.049 g doxorubicin/g ZIF-8) and did not take advantage of MOF structure. In our case, the therapeutic is incorporated as the linker, leading to drug loading of 0.74 g abdc/g $[Mn(abdc)(H_2O)_{1.5}(DMF)_{0.17}]_n$. Extrapolation of the release curve indicates the $[Mn(abdc)(H_2O)_{1.5}(DMF)_{0.17}]_n$ NPs would release 66 % of abdc in 9 days.

Surface functionalization has been previously shown to stabilize NPs in aqueous environments. For example, the Mn-BTC MOFs reported by Lin *et al.* demonstrated an increase in stability to give 60 % degradation over 30 h upon coating with a silica shell (80 % uncoated).[50] With regard to the coated $[Mn(abdc)(H_2O)_{1.5}(DMF)_{0.17}]_n$ NPs, the abdc release curve (open red circles, Figure 5.6) shows a similar overall trend to that of the uncoated material. The lack of initial fast release in the coated materials is most likely due to the replacement of weakly-bound, surface abdc by the polymer during surface functionalization. With this in mind, the copolymer coating decreased the overall release of abdc from the material, resulting in 15 % degradation over 30 h in comparison to 20 % for the uncoated material.

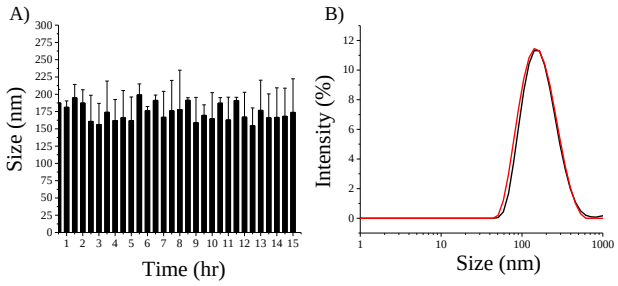

Figure 5.7. Polymer coated NPs in Na_2HPO_4 buffer monitored by DLS over 15 hours. A) Size of NP over a 15 hour period stays constant and B) the intensity of the measurements at 1 (black) and 15 (red) h are the same.

While the effect of the polymer coating on degradation stability was minor, surface functionalization was successful in maintaining dispersion and preventing aggregation in 50 mM

Na_2HPO_4 buffer (pH 7.6). The initial DLS size distribution curve for functionalized NPs indicates that the particles were well dispersed with the average size of 174 ± 12 nm. In comparison, the uncoated NPs in phosphate buffer displayed an average size of 378 ± 60 nm in the initial DLS measurement, indicating aggregation occurred rapidly in this environment. Furthermore, for the coated NPs, the average size, shape of the size distribution curve, and percent signal intensity did not change over a 15 h time period (Figure 5.7). Taken together, these observations indicate that the coated NPs did not aggregate or precipitate over the time period investigated.

In addition to facilitating dispersion, primary amines at the surface of the NPs are a convenient handle for further functionalization with targeting moieties or imaging agents. As a proof-of-concept experiment, a 5(6)-carboxytetramethylrhodamine dye was covalently attached to the NPs through amide bond formation using EDC coupling in water. After five washes, the suspension of NPs was fluorescent (Figure 5.8A, black). In contrast, NPs incubated with the fluorophore without the EDC coupling reagent were not fluorescent (Figure 5.8A, red); confirmation that the NP surface was covalently modified and the observed fluorescence was not a result of non-specific binding of the fluorophore. After functionalization of the NPs with rhodamine, the fluorescent signal was utilized to explore the cellular uptake of the NPs. HeLa Cells incubated for 30 minutes with 75 micrograms of rhodamine-tagged NPs display fluorescence signifying rapid and efficient cross-membrane transport of the NPs (Figure 5.8C).

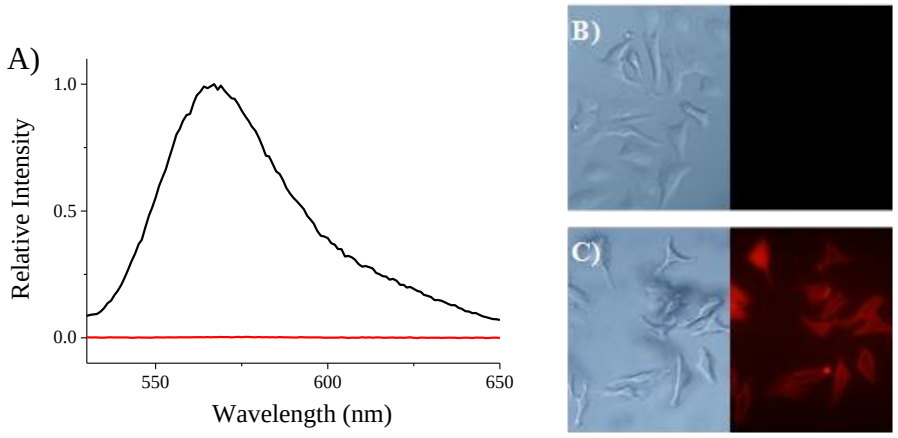

Figure 5.8. A) Fluorescence spectra (excitation λ = 520 nm) of NP incubated with dye (red), and dye covalently attached to NP (black). Right: Confocal fluorescence microscopy images of HeLa cells after thirty minute incubation B) without any NPs and C) with 75μg of rhodamine-labeled NPs.

With demonstrated optical imaging in hand, the focus shifted to quantifying the effectiveness of $[Mn(abdc)(H_2O)_{1.5}(DMF)_{0.17}]_n$ for MR contrast. MR contrast effectiveness is measured by probing the increase or decrease in proton relaxation times of water molecules surrounding or encapsulated inside the CP. Generally, contrast agents are categorized into "positive" and "negative" enhancement agents. Positive enhancement agents are those that serve to increase the brightness of images by shortening the proton *longitudinal* relaxation time (T_1). Materials, such as the $[Mn(abdc)(H_2O)_{1.5}(DMF)_{0.17}]_n$ NPs reported here, incorporating paramagnetic ions like Mn^{II}, represent these types of contrast agents, also termed T_1-weighted agents. Alternatively, negative enhancement agents are those that serve to darken images by shortening the T_2 relaxation time while maintaining T_1. These types of contrast agents include iron oxide NPs. Darkened images provided by negative contrast agents can be clinically confused with bleeding and calcification, as such, positive, T_1-weighted contrast agents are preferred.[73]

The MR contrast ability of the NPs was characterized by measuring the T_1 and T_2 relaxation times as a function of $[Mn(abdc)(H_2O)_{1.5}(DMF)_{0.17}]_n$ concentration for the uncoated and coated NPs. The relaxivity of a material (r_n) is the slope of the linear regression obtained from plotting $1/T_n = R_n$ as a function of ion concentration. The relaxivity (both r_1 and r_2) of uncoated material (Figure 5.9A) is much smaller (r_1 = 2.78 $mM^{-1}s^{-1}$ and r_2 = 39.36 $mM^{-1}s^{-1}$) than for the $MnCl_2$ control (r_1 = 4.83 $mM^{-1}s^{-1}$ and r_2 = 64.2 $mM^{-1}s^{-1}$, Figure S5.7), which is expected due to Mn^{II} complexation. Upon binding, the abdc ligands shield the Mn^{II} from local water molecules and, thus, decrease the affect the ion has on surrounding water relaxation. Typical relaxivity ratio (r_2/r_1) values of marketed Gd^{3+} T_1-weighted contrast agents are below 2, the target value when designing theranostic devices for MR contrast. While the $[Mn(abdc)(H_2O)_{1.5}(DMF)_{0.17}]_n$ NPs are not currently competitive with marketed Gd^{3+} materials, they exhibit similar relaxivity ratios (14.16) when compared with known Mn-based CPs.[50] This ratio is further reduced to 13.03 upon functionalization with the polymer coating (Figure 5.9B). This decrease in the relaxivity ratio upon polymer functionalization is attributed to an increase in the hydrophilicity of the coated NPs, thereby increasing the amount of surrounding water molecules and the relaxation effect of the Mn^{II}.[43] Therefore, it may be possible to further decrease the relaxivity ratio and increase MR contrast through synthetic manipulation of the polymer coating.

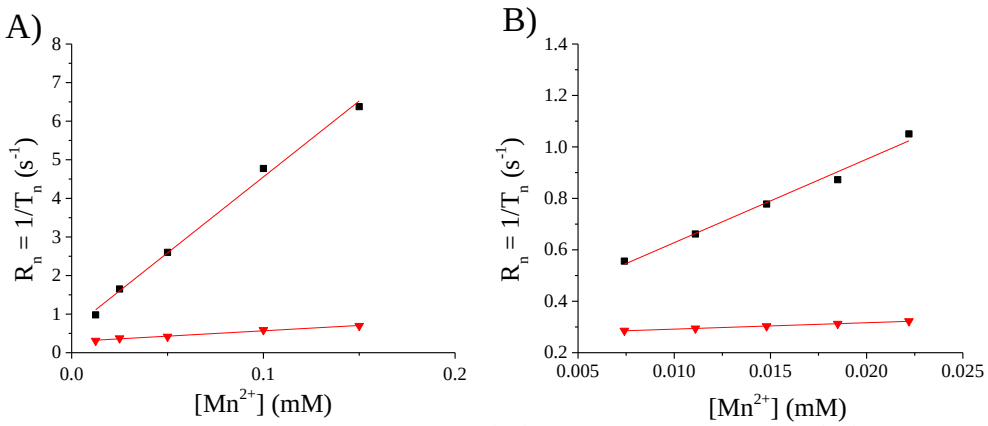

Figure 5.9. A) MRI relaxivity (r_1 = 2.78 $mM^{-1}s^{-1}$ and r_2 = 39.36 $mM^{-1}s^{-1}$) of uncoated NPs measured at 1.5 T. B) MRI relaxivity (r_1 = 2.49 $mM^{-1}s^{-1}$ and r_2 = 32.45 $mM^{-1}s^{-1}$) of coated NPs also measured at 1.5 T (black squares indicate measured T_2 and red triangles represent measured T_1).

5.5 Conclusions

In conclusion, we have prepared and demonstrated the bimodal imaging capability of a new manganese-containing coordination polymer theranostic. The nanoscale $[Mn(abdc)(H_2O)_{1.5}(DMF)_{0.17}]_n$ CPs were synthesized via a fast and simple solvothermal method. Surface functionalization with an amine-capped PEG-PCL polymer resulted in biocompatible, well-dispersed NPs that exhibited slow, controlled ligand release in aqueous environments. Additionally, the polymer coating provides a scaffold for the covalent attachment of molecular chromophores for fluorescence imaging. The incorporated Mn^{II} metal nodes impart moderate MR contrast ability with relaxivity ratios (r_2/r_1 = 13.03) competitive with previously published Mn-based MRI-active CPs. The demonstrated MR and fluorescence imaging functionalities provide the basis for the future development of bimodal thernanostics from CP constructs. With the synthetic diversity of CPs, libraries of nanothernostics with various imaging and targeting ability are within reach, bringing science one step closer to the goal of personalized medicines.

5.6 Acknowledgements

The authors would like to thank Virginia Tech and the Institute for Critical Technology and Applied Science (ICTAS) housed on the campus of Virginia Tech for funding and access to equipment. The authors are also grateful to the VT Chemistry Department for support and assistance with instrumentation.

5.7 References

1. Strebhardt, K.; Ullrich, A., Paul Ehrlich's Magic Bullet Concept: 100 Years of Progress. *Nature Reviews Cancer* **2008,** *8* (6), 473-480.

2. Allen, T. M.; Cullis, P. R., Drug Delivery Systems: Entering the Mainstream. *Science* **2004,** *303*, 1818-1822.

3. Dobson, J., Magnetic Nanoparticles for Drug Delivery. *Drug Development Research* **2006,** *67*, 55-60.

4. Gaumet, M.; Vargas, A.; Gurny, R.; Delie, F., Nanoparticles for Drug Delivery: The Need for Precision in Reporting Particle Size Parameters. *European Journal of Pharmaceutics and Biopharmaceutics* **2008,** *69*, 1-9.

5. Maeda, H.; Wu, J.; Sawa, T.; Matsumura, Y.; Hori, K., Tumor Vascular Permeability and the Epr Effect in Macromolecular Therapeutics: A Review. *Journal of Controlled Release* **2000,** *65* (1–2), 271-284.

6. Bulte, J. W. M.; Kraitchman, D. L., Iron Oxide Mr Contrast Agents for Molecular and Cellular Imaging. *NMR in Biomedicine* **2004,** *17* (7), 484-499.

7. Jiang, S.; Eltoukhy, A. A.; Love, K. T.; Langer, R.; Anderson, D. G., Lipidoid-Coated Iron Oxide Nanoparticles for Efficient DNA and Sirna Delivery. *Nanoletters* **2013,** *13* (3), 1059-1064.

8. Kim, B. H.; Lee, N.; Kim, H.; An, K.; Park, Y. I.; Choi, Y.; Shin, K.; Lee, Y.; Kwon, S. G.; Na, H. B.; Park, J.-G.; Ahn, T.-Y.; Kim, Y.-W.; Moon, W. K.; Choi, S. H.; Hyeon, T., Large-Scale Synthesis of Uniform and Extremely Small-Sized Iron Oxide Nanoparticles for High-Resolution T1 Magnetic Resonance Imaging Contrast Agents. *Journal of the American Chemical Society* **2011,** *133* (32), 12624-12631.

9. Small, W. C.; Nelson, R. C.; Bernardino, M. E., Dual Contrast Enhancement of Both T1- and T2-Weighted Sequences Using Ultrasmall Superparamagnetic Iron Oxide. *Magnetic Resonance Imaging* **1993,** *11* (5), 645-654.

10. Baek, M. J.; Park, J. Y.; Xu, W.; Kattel, K.; Kim, H. G.; Lee, E. J.; Patel, A. K.; Lee, J. J.; Chang, Y.; Kim, T. J.; Bae, J. E.; Chae, K. S.; Lee, G. H., Water-Soluble Mno Nanocolloid for a Molecular T1 Mr Imaging: A Facile One-Pot Synthesis, in Vivo T1 Mr Images, and Account for Relaxivities. *ACS Applied Materials & Interfaces* **2010,** *2* (10), 2949-2955.

11. Kim, T.; Momin, E.; Choi, J.; Yuan, K.; Zaidi, H.; Kim, J.; Park, M.; Lee, N.; McMahon, M. T.; Quinones-Hinojosa, A.; Bulte, J. W. M.; Hyeon, T.; Gilad, A. A., Mesoporous Silica-Coated Hollow Manganese Oxide Nanoparticles as Positive T1 Contrast Agents for Labeling and Mri Tracking of Adipose-Derived Mesenchymal Stem Cells. *Journal of the American Chemical Society* **2011,** *133* (9), 2955-2961.

12. Park, M.; Lee, N.; Choi, S. H.; An, K.; Yu, S.-H.; Kim, J. H.; Kwon, S.-H.; Kim, D.; Kim, H.; Baek, S.-I.; Ahn, T.-Y.; Park, O. K.; Son, J. S.; Sung, Y.-E.; Kim, Y.-W.; Wang, Z.;

Pinna, N.; Hyeon, T., Large-Scale Synthesis of Ultrathin Manganese Oxide Nanoplates and Their Applications to T1 Mri Contrast Agents. *Chemistry of Materials* **2011,** *23* (14), 3318-3324.

13. Kim, C. S.; Tonga, G. Y.; Solfiell, D.; Rotello, V. M., Inorganic Nanosystems for Therapeutic Delivery: Status and Prospects. *Advanced Drug Delivery Reviews* **2013,** *65* (1), 93-99.
14. Gref, R.; Minamitake, Y.; Peracchia, M. T.; Trebetskoy, V.; Torchilin, V.; Langer, R., Biodegradable Long-Circulating Polymeric Nanospheres. *Science* **1994,** *263*, 1600+.
15. Liong, M.; Lu, J.; Kovochich, M.; Xia, T.; Ruehm, S. G.; Nel, A. E.; Tamanoi, F.; Zink, J. I., Multifunctional Inorganic Nanoparticles for Imaging, Targeting, and Drug Delivery. *ACS Nano* **2008,** *2* (5), 889-896.
16. Gautier, J.; Allard-Vannier, E.; Munnier, E.; Soucé, M.; Chourpa, I., Recent Advances in Theranostic Nanocarriers of Doxorubicin Based on Iron Oxide and Gold Nanoparticles. *Journal of Controlled Release 169* (1–2), 48-61.
17. Janib, S. M.; Moses, A. S.; MacKay, J. A., Imaging and Drug Delivery Using Theranostic Nanoparticles. *Advanced Drug Delivery Reviews* **2010,** *62* (11), 1052-1063.
18. Calderon, M.; Quadir, M. A.; Sharma, S. K.; Haag, R., Dendritic Polyglycerols for Biomedical Applications. *Advanced Materials* **2010,** *22*, 190-218.
19. Soppimath, K. S.; Aminabhavi, T. M.; Kulkarni, A. R.; Rudzinski, W. E., Biodegradable Polymeric Nanoparticles as Drug Delivery Devices. *Journal of Controlled Release* **2001,** *70*, 1-20.

20. Vivero-Escoto, J. L.; Huxford-Phillips, R. C.; Lin, W., Silica-Based Nanoprobes for Biomedical Imaging and Theranostic Applications. *Chemical Society Reviews* **2012,** *41* (7), 2673-2685.

21. Kumar R, K. A., Nagesha DK, Sridhar S. , In Vitro Evaluation of Theranostic Polymeric Micelles for Imaging and Drug Delivery in Cancer. *Theranostics* **2012,** *2* (7), 714-722.

22. Kataoka, K.; Harada, A.; Nagasaki, Y., Block Copolymer Micelles for Drug Delivery: Design, Characterization and Biological Significance. *Advanced Drug Delivery Reviews* **2001,** *47*, 113-131.

23. Kedar, U.; Phutane, P.; Shidhaye, S.; Kadam, V., Advances in Polymeric Micelles for Drug Delivery and Tumor Targeting. *Nanomedicine* **2010,** *6*, 714-729.

24. Rapoport, N.; Pitt, W. G.; Sun, H.; Nelson, J. L., Drug Delivery in Polymeric Micelles: From in Vitro to in Vivo. *Journal of Controlled Release* **2003,** *91*, 85-95.

25. Li, S.; Goins, B.; Zhang, L.; Bao, A., Novel Multifunctional Theranostic Liposome Drug Delivery System: Construction, Characterization, and Multimodality Mr, near-Infrared Fluorescent, and Nuclear Imaging. *Bioconjugate Chemistry* **2012,** *23* (6), 1322-1332.

26. Santra, S.; Kaittanis, C.; Grimm, J.; Perez, J. M., Drug/Dye-Loaded, Multifunctional Iron Oxide Nanoparticles for Combined Targeted Cancer Therapy and Dual Optical/Magnetic Resonance Imaging. *Small* **2009,** *5* (16), 1862-1868.

27. Lucignani, G., Nanoparticles for Concurrent Multimodality Imaging and Therapy: The Dawn of New Theragnostic Synergies. *European Journal of Nuclear Medicine & Molecular Imaging* **2009,** *36* (5), 869-874.

28. Melancon, M. P.; Zhou, M.; Li, C., Cancer Theranostics with near-Infrared Light-Activatable Multimodal Nanoparticles. *Accounts of Chemical Research* **2011,** *44* (10), 947-956.

29. Bao, G.; Mitragotri, S.; Tong, S., Multifunctional Nanoparticles for Drug Delivery and Molecular Imaging. *Annual Review of Biomedical Engineering* **2013,** *15* (1), 253-282.

30. Kim, J. S.; Rieter, W. J.; Taylor, K. M. L.; An, H.; Lin, W.; Lin, W., Self-Assembled Hybrid Nanoparticles for Cancer-Specific Multimodal Imaging. *Journal of the American Chemical Society* **2007,** *129* (29), 8962-8963.

31. Das, M.; Mishra, D.; Dhak, P.; Gupta, S.; Maiti, T. K.; Basak, A.; Pramanik, P., Biofunctionalized, Phosphonate-Grafted, Ultrasmall Iron Oxide Nanoparticles for Combined Targeted Cancer Therapy and Multimodal Imaging. *Small* **2009,** *5* (24), 2883-2893.

32. Xu, H.; Cheng, L.; Wang, C.; Ma, X.; Li, Y.; Liu, Z., Polymer Encapsulated Upconversion Nanoparticle/Iron Oxide Nanocomposites for Multimodal Imaging and Magnetic Targeted Drug Delivery. *Biomaterials* **2011,** *32* (35), 9364-9373.

33. Caldorera-Moore, M. E.; Liechty, W. B.; Peppas, N. A., Responsive Theranostic Systems: Integration of Diagnostic Imaging Agents and Responsive Controlled Release Drug Delivery Carriers. *Accounts of Chemical Research* **2011,** *44* (10), 1061-1070.

34. Hüber, M. M.; Staubli, A. B.; Kustedjo, K.; Gray, M. H. B.; Shih, J.; Fraser, S. E.; Jacobs, R. E.; Meade, T. J., Fluorescently Detectable Magnetic Resonance Imaging Agents. *Bioconjugate Chemistry* **1998,** *9* (2), 242-249.

35. Mulder, W. J. M.; Strijkers, G. J.; Habets, J. W.; Bleeker, E. J. W.; van der Schaft, D. W. J.; Storm, G.; Koning, G. A.; Griffioen, A. W.; Nicolay, K., Molecular Imaging and Fluorescence Microscopy for Identification of Activated Tumor Endothelium Using a Bimodal Lipidic Nanoparticle. *FASEB Journal* **2005,** *19* (14), 2008-2010.

36. Das, G. K.; Heng, B. C.; Ng, S.-C.; White, T.; Loo, J. S. C.; D'Silva, L.; Padmanabhan, P.; Bhakoo, K. K.; Selvan, S. T.; Tan, T. T. Y., Gadolinium Oxide Ultranarrow Nanorods as Multimodal Contrast Agents for Optical and Magnetic Resonance Imaging. *Langmuir* **2010,** *26* (11), 8959-8965.

37. Yang, H.; Santra, S.; Walter, G. A.; Holloway, P. H., Gdiii-Functionalized Fluorescent Quantum Dots as Multimodal Imaging Probes. *Advanced Materials* **2006,** *18* (21), 2890-2894.

38. Choi, J. H.; Nguyen, F. T.; Barone, P. W.; Heller, D. A.; Moll, A. E.; Patel, D.; Boppart, S. A.; Strano, M. S., Multimodal Biomedical Imaging with Asymmetric Single-Walled Carbon Nanotube/Iron Oxide Nanoparticle Complexes. *Nanoletters* **2007,** *7* (4), 861-867.

39. Mulder, W. J. M.; Koole, R.; Brandwijk, R. J.; Storm, G.; Chin, P. T. K.; Strijkers, G. J.; de Mello Donegá, C.; Nicolay, K.; Griffioen, A. W., Quantum Dots with a Paramagnetic Coating as a Bimodal Molecular Imaging Probe. *Nanoletters* **2005,** *6* (1), 1-6.

40. Louie, A., Multimodality Imaging Probes: Design and Challenges. *Chemical Reviews* **2010,** *110* (5), 3146-3195.

41. Lee, J. E.; Lee, N.; Kim, T.; Kim, J.; Hyeon, T., Multifunctional Mesoporous Silica Nanocomposite Nanoparticles for Theranostic Applications. *Accounts of Chemical Research* **2011,** *44*, 893-902.

42. Hao, R.; Xing, R.; Xu, Z.; Hou, Y.; Gao, S.; Sun, S., Synthesis, Functionalization, and Biomedical Applications of Multifunctional Magnetic Nanoparticles. *Advanced Materials* **2010,** *22*, 2729-2742.

43. Della Rocca, J.; Liu, D.; Lin, W., Nanoscale Metal–Organic Frameworks for Biomedical Imaging and Drug Delivery. *Accounts of Chemical Research* **2011,** *44* (10), 957-968.

44. Horcajada, P.; Chalati, T.; Serre, C.; Gillet, B.; Sebrie, C.; Baati, T.; Eubank, J. F.; Heurtaux, D.; Clayette, P.; Kreuz, C.; Chang, J.-S.; Hwang, Y. K.; Marsaud, V.; Bories, P.-N.; Cynober, L.; Gil, S.; Férey, G.; Couvreur, P.; Gref, R., Porous Metal–Organic-Framework Nanoscale Carriers as a Potential Platform for Drug Delivery and Imaging. *Nature Materials* **2010,** *9* (2), 172-178.

45. Horcajada, P.; Gref, R.; Baati, T.; Allan, P. K.; Maurin, G.; Couvreur, P.; Férey, G.; Morris, R. E.; Serre, C., Metal–Organic Frameworks in Biomedicine. *Chemical Reviews* **2011,** *112* (2), 1232-1268.

46. McKinlay, A. C.; Morris, R. E.; Horcajada, P.; Férey, G.; Gref, R.; Couvreur, P.; Serre, C., Biomofs: Metal–Organic Frameworks for Biological and Medical Applications. *Angewandte Chemie International Edition* **2010,** *49* (36), 6260-6266.

47. Huxford, R. C.; Della Rocca, J.; Lin, W., Metal–Organic Frameworks as Potential Drug Carriers. *Current Opinion in Chemical Biology* **2010,** *14* (2), 262-268.

48. Horcajada, P.; Serre, C.; Vallet-Regí, M.; Sebban, M.; Taulelle, F.; Férey, G., Metal–Organic Frameworks as Efficient Materials for Drug Delivery. *Angewandte Chemie International Edition* **2006,** *45* (36), 5974-5978.

49. Della Rocca, J.; Lin, W., Nanoscale Metal–Organic Frameworks: Magnetic Resonance Imaging Contrast Agents and Beyond. *European Journal of Inorganic Chemistry* **2010,** *2010* (24), 3725-3734.

50. Taylor, K. M. L.; Rieter, W. J.; Lin, W., Manganese-Based Nanoscale Metal−Organic Frameworks for Magnetic Resonance Imaging. *Journal of the American Chemical Society* **2008,** *130* (44), 14358-14359.

51. Rieter, W. J.; Taylor, K. M. L.; An, H.; Lin, W.; Lin, W., Nanoscale Metal−Organic Frameworks as Potential Multimodal Contrast Enhancing Agents. *Journal of the American Chemical Society* **2006,** *128* (28), 9024-9025.

52. Taylor, K. M. L.; Jin, A.; Lin, W., Surfactant-Assisted Synthesis of Nanoscale Gadolinium Metal–Organic Frameworks for Potential Multimodal Imaging. *Angewandte Chemie International Edition* **2008,** *47* (40), 7722-7725.

53. Dimmock, J. R.; Erciyas, E.; Kumar, P.; Hetherington, M.; Quail, J. W.; Pugazhenthi, U.; Arpin, S. A.; Hayes, S. J.; Allen, T. M.; Halleran, S.; Clercq, E. D.; Baizarini, J.; Stables, J. P., Mannich Bases of Phenolic Azobenzenes Possessing Cytotoxic Activity. *European Journal of Medicinal Chemistry* **1997,** *32* (7–8), 583-594.

54. Mary, L. J. F.; Kannan, P., Synthesis, Characterization and Thermal Behaviour of Poly(Pyromellitimide-Ester)S and (Imide-Urethane)S Containing Azobenzene Units. *European Polymer Journal* **1998,** *35* (1), 17-26.

55. Na, H. B.; Lee, J. H.; An, K.; Park, Y. I.; Park, M.; Lee, I. S.; Nam, D.-H.; Kim, S. T.; Kim, S.-H.; Kim, S.-W.; Lim, K.-H.; Kim, K.-S.; Kim, S.-O.; Hyeon, T., Development of a T1 Contrast Agent for Magnetic Resonance Imaging Using Mno Nanoparticles. *Angewandte Chemie International Edition* **2007,** *46* (28), 5397-5401.

56. Port, M.; Idee, J.-M.; Medina, C.; Robic, C.; Sabatou, M.; Corot, C., Efficiency, Thermodynamic and Kinetic Stability of Marketed Gadolinium Chelates and Their Possible Clinical Consequences: A Critical Review. *BioMetals* **2008,** *21* (4), 469-490.

57. Rowe, M. D.; Chang, C.-C.; Thamm, D. H.; Kraft, S. L.; Harmon, J. F.; Vogt, A. P.; Sumerlin, B. S.; Boyes, S. G., Tuning the Magnetic Resonance Imaging Properties of

Positive Contrast Agent Nanoparticles by Surface Modification with Raft Polymers. *Langmuir* **2009,** *25* (16), 9487-9499.

58. Val M. Runge; Ai, T. D., Hao; Xuemei Hu, The Developmental History of the Gadolinium Chelates as Intravenous Contrast Media for Magnetic Resonance. *Investigative Radiology* **2011,** *46* (12), 807-816.

59. Kueny-Stotz, M.; Garofalo, A.; Felder-Flesch, D., Manganese-Enhanced Mri Contrast Agents: From Small Chelates to Nanosized Hybrids. *European Journal of Inorganic Chemistry* **2012,** *2012* (12), 1987-2005.

60. Stolik, S.; Delgado, J. A.; Pérez, A.; Anasagasti, L., Measurement of the Penetration Depths of Red and near Infrared Light in Human "Ex Vivo" Tissues. *Journal of Photochemistry and Photobiology B: Biology* **2000,** *57* (2–3), 90-93.

61. He, J.; Yu, J.; Zhang, Y.; Pan, Q.; Xu, R., Synthesis, Structure, and Luminescent Property of a Heterometallic Metal−Organic Framework Constructed from Rod-Shaped Secondary Building Blocks. *Inorganic Chemistry* **2005,** *44* (25), 9279-9282.

62. McDonald, T. M.; Lee, W. R.; Mason, J. A.; Wiers, B. M.; Hong, C. S.; Long, J. R., Capture of Carbon Dioxide from Air and Flue Gas in the Alkylamine-Appended Metal–Organic Framework Mmen-Mg2(Dobpdc). *Journal of the American Chemical Society* **2012,** *134* (16), 7056-7065.

63. Senkovska, I.; Kaskel, S., Solvent-Induced Pore-Size Adjustment in the Metal-Organic Framework [Mg3(Ndc)3(Dmf)4] (Ndc = Naphthalenedicarboxylate). *European Journal of Inorganic Chemistry* **2006,** *2006* (22), 4564-4569.

64. Qi, W.; Ghoroghchian, P. P.; Li, G.; Hammer, D. A.; Therien, M. J., Aqueous Self-Assembly of Poly(Ethylene Oxide)-Block-Poly(?-Caprolactone) (Peo-B-Pcl) Copolymers:

Disparate Diblock Copolymer Compositions Give Rise to Nano- and Meso-Scale Bilayered Vesicles. *Nanoscale* **2013,** *5* (22), 10908-10915.

65. Chan, R. T. H.; Marcal, H.; Russell, R. A.; Holden, P. J.; Foster, L. J. R., Application of Polyethylene Glycol to Promote Cellular Biocompatibility of Polyhydroxybutyrate Films. *International Journal of Polymer Science* **2011**.

66. Kohler, N.; Fryxell, G. E.; Zhang, M., A Bifunctional Poly(Ethylene Glycol) Silane Immobilized on Metallic Oxide-Based Nanoparticles for Conjugation with Cell Targeting Agents. *Journal of the American Chemical Society* **2004,** *126* (23), 7206-7211.

67. Owens Iii, D. E.; Peppas, N. A., Opsonization, Biodistribution, and Pharmacokinetics of Polymeric Nanoparticles. *International Journal of Pharmaceutics* **2006,** *307* (1), 93-102.

68. Guerrero-García, G. I.; González Mozuelos, P.; Olvera de la Cruz, M., Large Counterions Boost the Solubility and Renormalized Charge of Suspended Nanoparticles. *ACS Nano* **2013**.

69. Yang, X.; Lin, H.; Lu, W.; Wang, D., Compatibility Study of Merrifield Linker in Fmoc Strategy Peptide Synthesis. *Protein and Peptide Letters* **2013,** *20* (2), 140-5.

70. Kang, S. W.; Li, Y.; Park, J. H.; Lee, D. S., Ph-Triggered Unimer/Vesicle-Transformable and Biodegradable Polymersomes Based on Peg-B-Pcl–Grafted Poly(B-Amino Ester) for Anti-Cancer Drug Delivery. *Polymer* **2013,** *54* (1), 102-110.

71. Morcellet-Sauvage, J.; Morcellet, M.; Loucheux, C., Polymethacrylic Acid Derivatives, 4. Solubilization of Azobenzene, a Water Insoluble Nonpolar Compound. *Macromolecular Chemistry and Physics* **1982,** *183* (4), 839-848.

72. Vasconcelos, I. B.; Silva, T. G. d.; Militao, G. C. G.; Soares, T. A.; Rodrigues, N. M.; Rodrigues, M. O.; Costa, N. B. d.; Freire, R. O.; Junior, S. A., Cytotoxicity and Slow

Release of the Anti-Cancer Drug Doxorubicin from Zif-8. *RSC Advances* **2012,** *2* (25), 9437-9442.

73. Terreno, E.; Castelli, D. D.; Viale, A.; Aime, S., Challenges for Molecular Magnetic Resonance Imaging. *Chemical Reviews* **2010,** *110* (5), 3019-3042.

5.8 Supporting Information

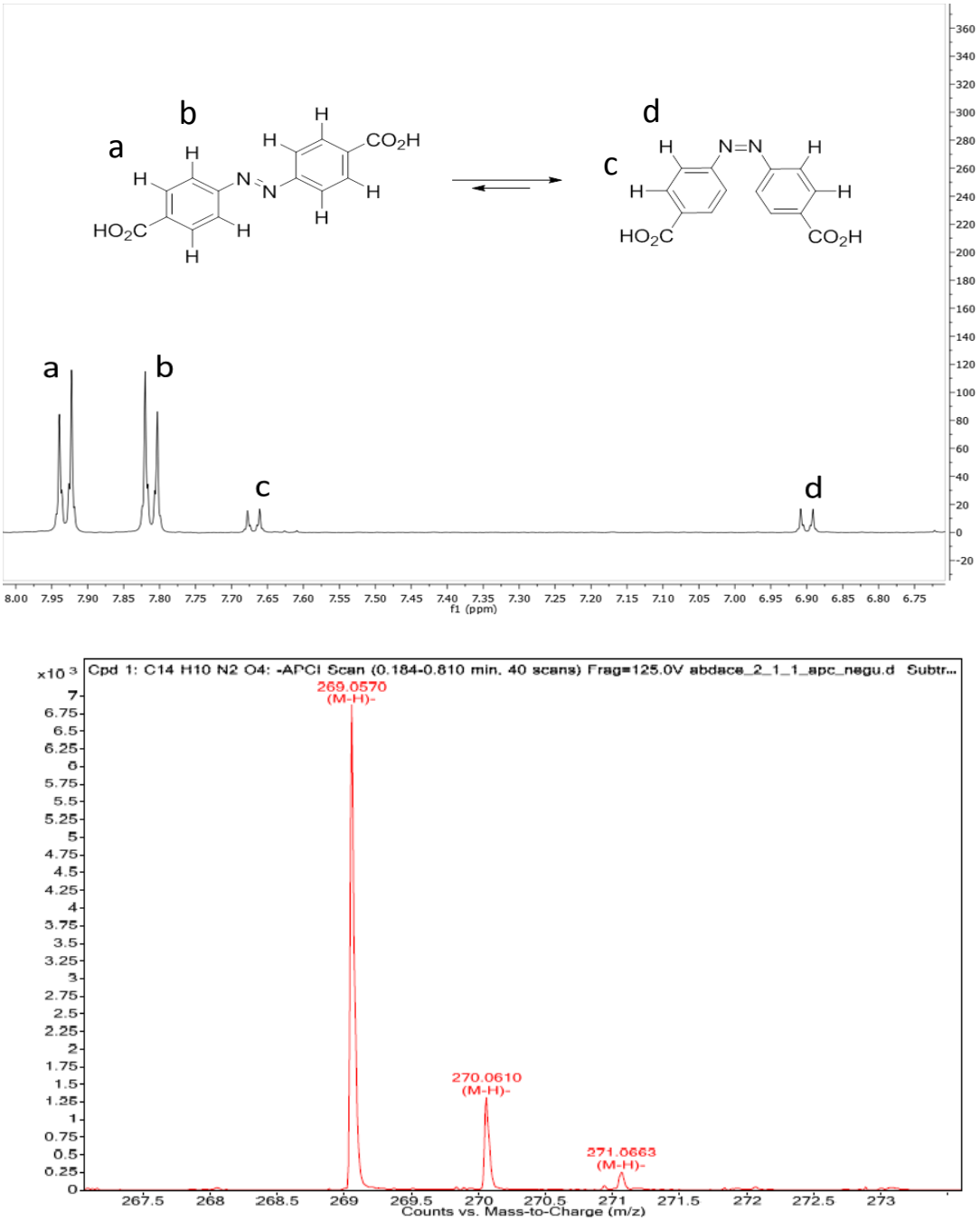

Figure S5.1. ^{1}H NMR of abdc in D_2O (Top). Mass Spectrometry of abdc (Bottom).

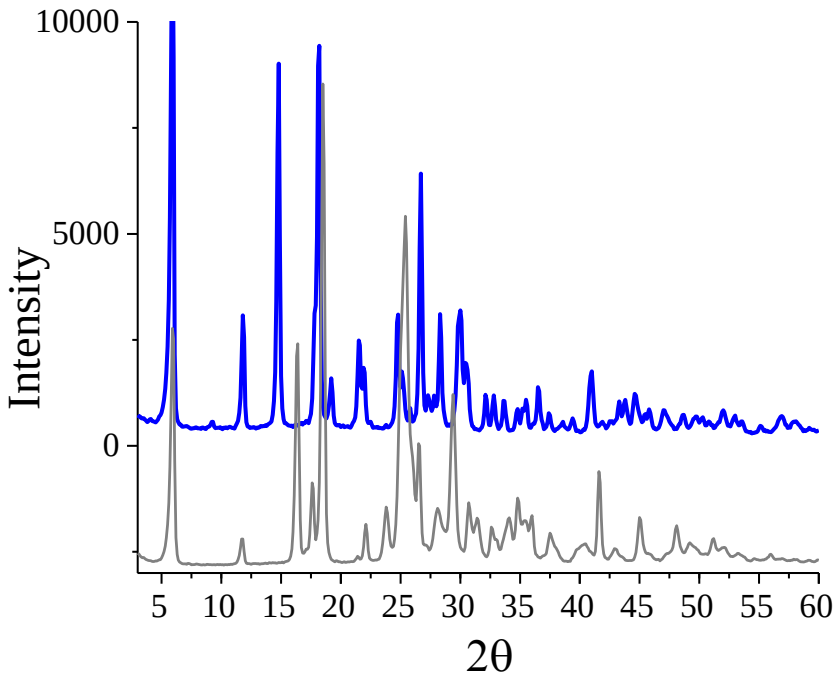

Figure S5.2. PXRD patterns of abda (grey) and Mn(abdc)$(H_2O)_{1.5}(DMF)_{0.17}$ NPs (blue). There is an absence of peaks and appearance of new peaks in the pattern of the NPs, indicating that a new material is formed.

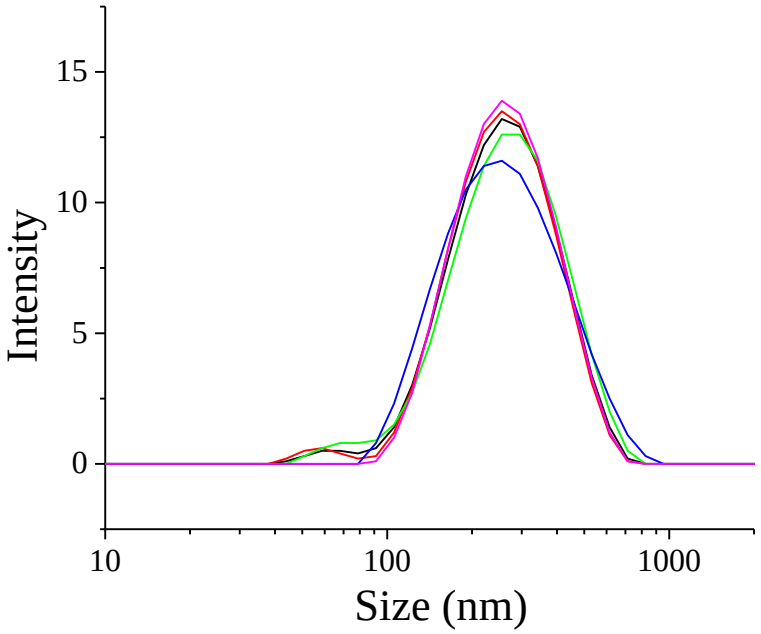

Figure S5.3. DLS analysis of $[Mn(abda)(H_2O)_{1.5}(DMF)_{0.17}]_n$ NPs. Each trace was collected on the same sample and is the average of 10 measurements. The average peak position was at 231 ± 2 nm.

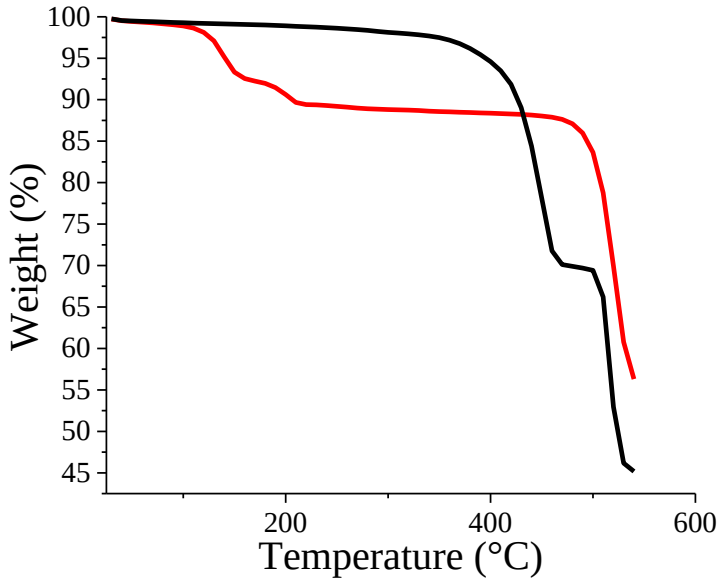

Figure S5.4. TGA curve of abda (black) and the NPs (red). The abda is stable up to ~400 °C.

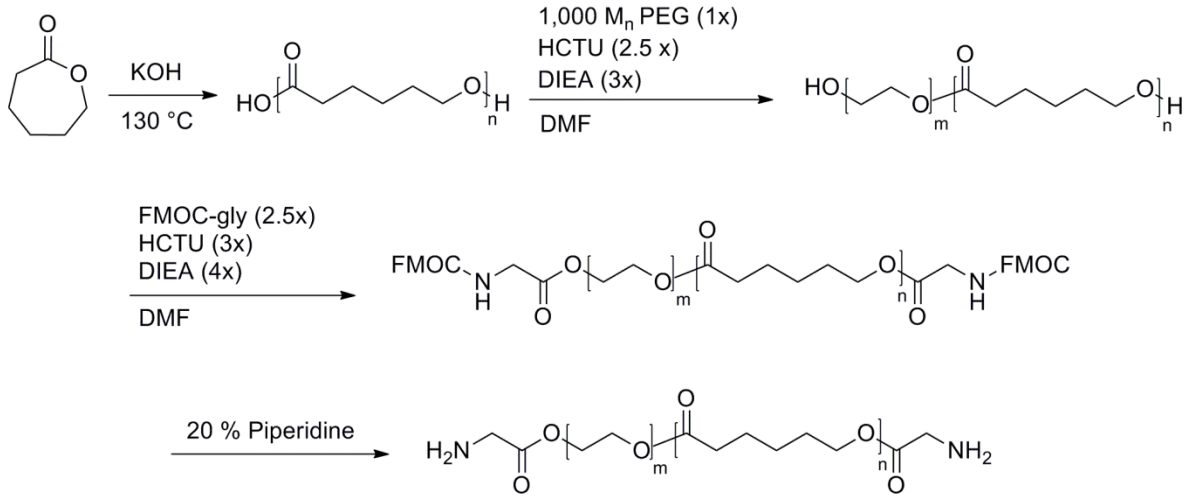

Scheme S5.1. Synthesis of NH_2-PEG-*b*-PCL-NH_2.

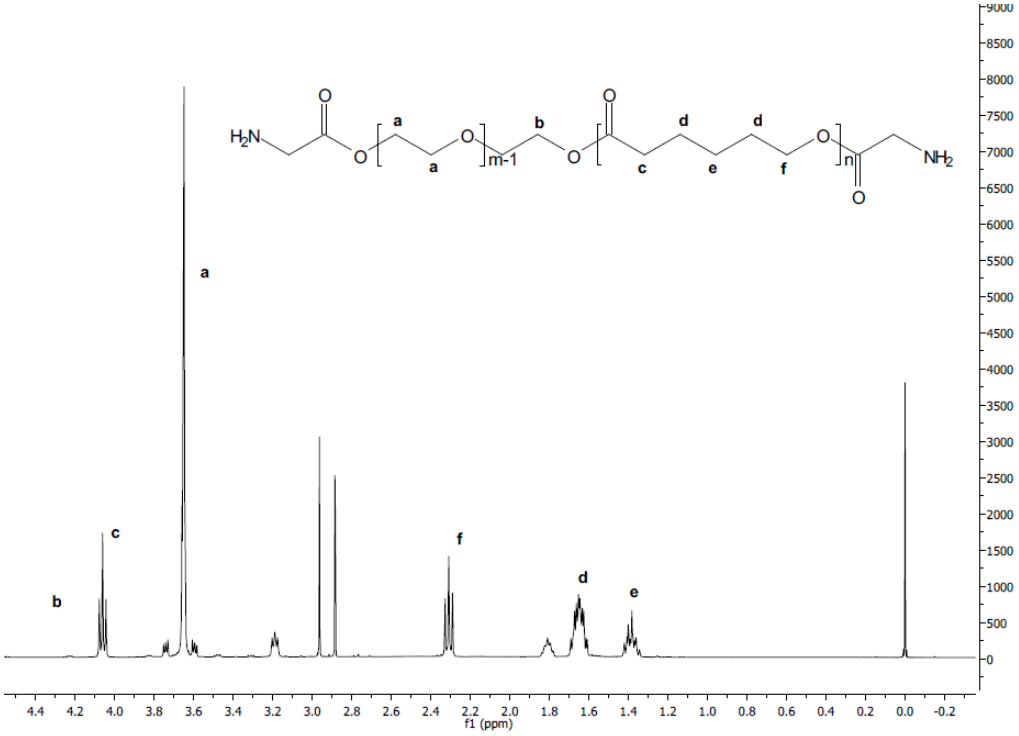

Figure S5.5. ^{1}H NMR of NH_2-PEG-*b*-PCL-NH_2 in $CDCl_3$.

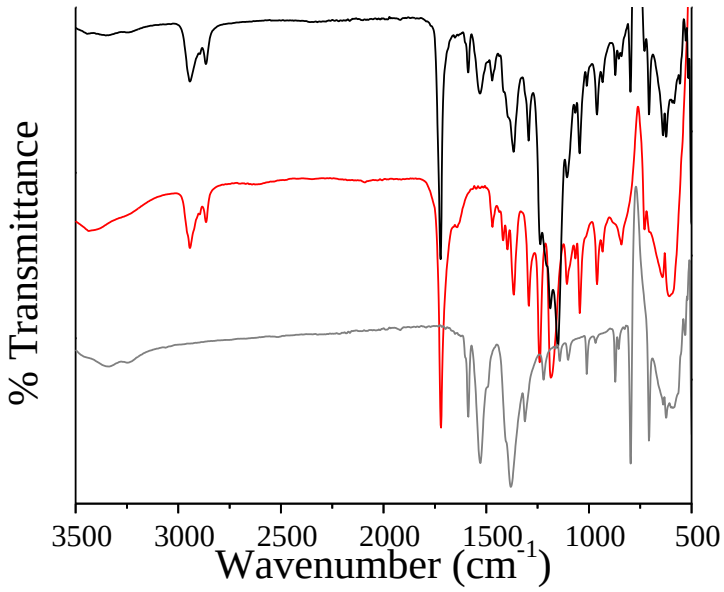

Figure S5.6. FT-IR of uncoated NPs (grey), the double ended amine H_2N-PEG-*b*-PCL-NH_2 copolymer (red), and of coated NPs (black). From the FT-IR of the coated materials, the sharp peak at ~1750 cm^{-1}corresponds to the C=O stretching of the carbonyl group in the PCL portion of the copolymer. Also evident are peaks slightly above 1500 cm^{-1} that correspond to the carboxylato functionality in the coordination polymer.

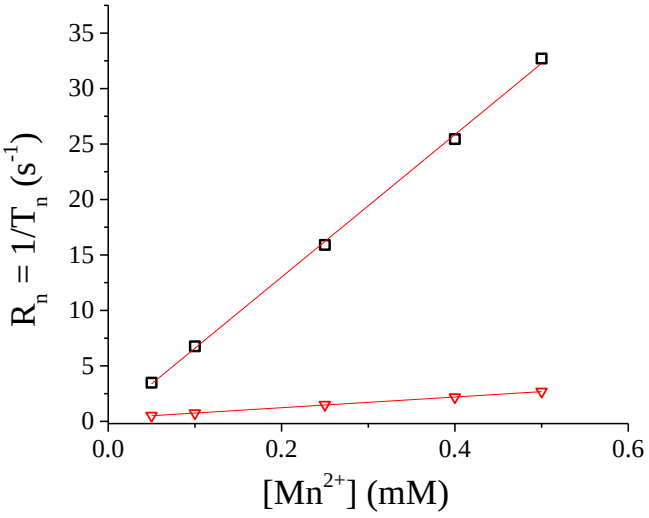

Figure S5.7. MRI relaxivity (r_1 = 4.83 $mM^{-1}s^{-1}$ and r_2 = 64.2 $mM^{-1}s^{-1}$) of a Mn^{2+} control (made using $MnCl_2 \bullet 4H_2O$) measured at 1.5 T.

6. Conclusions and Outlook

6.1 Summary of Work Completed

The first example of a MOF nano-cage that releases a cargo "on command" due to MOF degradation when irradiated with light has been developed. Optimization of the synthesis of the MOF resulted in ~100 nm nanoparticles with a surface area of ~2500 m^2/g. The MOF is isostructural with UiO-AZB (UiO = University of Oslo) and consists of $Zr_6O_4(OH)_4$ metal clusters bridged by 4,4´-azobenzenedicarboxylate (AZB) linkers. Due to the isomerization of AZB from the trans- to the cis- form upon irradiation with light, the structural integrity of the nanoparticles is compromised when illuminated. This degradation of the framework facilitates the release of the model drug Nile Red (0.04 ± 0.01 %/h in the dark vs. 0.36 ± 0.02 %/h when irradiated). Initial cell uptake studies confirmed that the nanoparticles are taken into the cytoplasm by HeLa cells as evidenced by Z stacking of confocal microscopy images.

The UiO-AZB platform developed was then tested *in vitro* to probe the efficacy for selectively killing cancer cells under irradiation while providing little to no toxicity in the dark. The cancer drug 5-fluorouracil was loaded into the nanoparticles at ~15 wt% and they were subsequently coated with an aminated polyethylene glycol ($PEGNH_2$) stabilizing polymer. The degradation of the final drug-MOF system, termed $PEGNH_2$@5-FU-UiOAZB, was found to be light dependent, where little to no degradation occurred in the dark, while 0.72 ± 0.03 %/h was released upon irradiation with a 340 nm LED array. When incubated with MCF-7 human breast cancer cells, low toxicity was observed for the $PEGNH_2$@5-FU-UiOAZB nanoparticles when the cells were kept in the dark. However, ~80 % of cells died when incubated with 3000 μg/mL $PEGNH_2$@5-FU-UiOAZB under irradiation. These cell studies support that the drug is not

releasing from the MOF system until irradiation and therefore, the mechanism for delivery would be photo-enhanced degradation to release cargos controllably.

Finally, we have also developed a Mn^{II} coordination polymer (CP), $[Mn(abdc)(H_2O)_{1.5}(DMF)_{0.17}]_n$, where abdc is another acronym for 4,4´-azobenzenedicarboxylate, that is versatile for several diagnostic imaging modalities. The incorporation of Mn^{II} into the framework allows for improving relaxivity ratios (a useful benchmark to consider when comparing to clinically available contrast agents at ~2) to 14.16 in comparison to current literature ratios for CPs. Also, by functionalizing the surface with a polymer coating, this ratio dropped to 13.03. Furthermore, the particles were tagged with a fluorescent 5(6)-carboxytetramethylrhodamine dye and incubated with HeLa cells. Cell uptake was confirmed via fluorescence microscopy and so, we were able to show that materials like these may be useful for the transition from the benchtop (*in vitro*) to animal studies (*in vivo*) due to the incorporation of highly sensitive fluorescence tags and Mn^{II} metal ions for MRI contrast. These studies have laid the foundation for the development of more advanced materials that combine controlled drug delivery with diagnostic imaging to afford theranostic nanomedicines.

6.2 Outlook and Future Work

We have provided a platform for immense potential of MOFs to act as photo-degradable nanocarriers able to secure payloads until triggered via a photo-stimulus. The diversity of these types of systems is extensive (not just for drug delivery applications) due to many azobenzene derivatives and multiple metal options that offer additional functionality. For example, the possible doping of Mn^{II} into the UiO-AZB core structure could offer the advantage of MRI contrast. We have also shown the ability to coat the nanoparticles with a stabilizing polymer and an optical dye (Nile Red) which opens up avenues of changing the fluorophore or polymer for

different applications. Finally and perhaps most broadly, is the ability to easily alter the linker synthesis to create different functionalized linkers. For example, the synthesis is tolerable to a variety of electron donating or withdrawing groups, and the addition of these groups to the core phenyl rings, would change the photo-physical properties of the AZB derivative. Also, modifying the carboxylate chelating group to stronger or weaker Lewis bases could change the stability of the final MOF products. While the possibilities are extensive, for drug delivery applications, the path from discovery to actual implementation in a clinical setting is always difficult, even for small molecule drugs. Therefore, research efforts are needed across a range of disciplines.